

IoT-enabled Graphene-based Microfluidic Biosensors for Multiple Biomolecule Detection

THESIS

Submitted in partial fulfilment
of the requirements for the degree of
DOCTOR OF PHILOSOPHY

by

Mrunali Dnyaneshwar Wagh

ID. No. 2019PHXF0428H

Under the Supervision of

Prof. Subhendu Sahoo

Co-supervision of

Prof. Sanket Goel and Prof. Michael Dickey



BITS Pilani
Pilani | Dubai | Goa | Hyderabad

Birla Institute of Technology and Science, Pilani

Hyderabad Campus

2023

BIRLA INSTITUTE OF TECHNOLOGY AND SCIENCE, PILANI

CERTIFICATE

This is to certify that the thesis entitled “**IoT-enabled Graphene-based Microfluidic Biosensors for Multiple Biomolecule Detection**” and submitted by **MRUNALI WAGH**, ID. No. **2019PHXF0428H** for the award of Ph.D. of the institute embodies original work done by his under my supervision.



Signature of the Supervisor:

Name in capital letters: PROF. SUBHENDU SAHOO

Designation: Professor, Department of Electrical & Electronics Engineering, BITS-Pilani, Hyderabad Campus

Date: 9 May 2023



Signature of the Co-Supervisor:

Name in capital letters: PROF. SANKET GOEL

Designation: Professor, Department of Electrical & Electronics Engineering, BITS-Pilani, Hyderabad Campus

Date: 9 May 2023



Signature of the Co-supervisor:

Name in capital letters: PROF. MICHAEL DICKEY

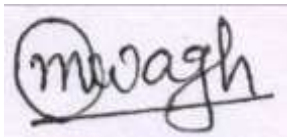
Designation: Professor, Dept. of Chemical & Biomolecular Engineering, North Carolina State University Raleigh, NC

Date: 9 May 2023

DECLARATION

I hereby declare that the work described in this thesis, entitled “IoT driven Microfluidic Biosensor for the biomedical application” is being submitted by me in partial fulfilment for the award of doctor of philosophy (Ph.D.) in the department of Electrical and Electronics Engineering Department (EEE) Department of Birla Institute of Technology & Science-Pilani, is the result of investigations carried out by me under the guidance of Prof. Subhendu Sahoo, Prof. Sanket Goel (Supervisor), Professor, Electrical and Electronics Engineering Department , BITS Pilani Hyderabad Campus and Prof. Michael Dickey Professor, Dept. of Chemical & Biomolecular Engineering North Carolina State University Raleigh, NC.

This work is original and has not been submitted for award of any Degree/Diploma of this or any other university.

A handwritten signature in black ink on a light purple background. The signature is written in a cursive style and reads "mrunali wagh". The first letter 'm' is enclosed in a circle.

Mrunali Wagh

ID. No: 2019PHXF0428H

ACKNOWLEDGMENT

The pursuit of knowledge and curiosity has played a vital role in my doctoral program, serving as the catalyst for my continuous learning. Through moments of courage, I have made significant strides both personally and professionally, while also recognizing that a lack of courage has prompted me to re-evaluate my choices. From a technical perspective, my guiding principle has been further solidified, given that the endeavors I pursued throughout my doctoral program have been essential in shaping my growth as both a researcher and an individual. Technically, my deep appreciation goes to the invaluable contributions and mentorship of individuals, without whom my doctoral program wouldn't have been possible.

I am deeply grateful to my esteemed supervisors, **Dr. Sanket Goel** and **Dr. Subhendu Sahoo**, for their unwavering mentorship and trust in me throughout my journey from a graduate student to an early researcher. With Prof. Sanket Goel contagious zeal and relentless commitment to excellence have served as a profound source of inspiration, impelling me to consistently surpass my limits and relentlessly strive for continuous improvement. The invaluable skill of scientific articulation and writing that I have acquired from Prof. Goel has been a defining factor in all my research outcomes. I will always be thankful to Dr. Subhendu Sahoo for entrusting me with an ambitious interdisciplinary research project during my 3 years of journey, which sparked my passion for research and engineering.

The insightful discussions I have had with **Prof. Michael Dickey** have been instrumental in correcting my approach on numerous occasions and he taught me the importance of simplicity in solving complex issues, a valuable lesson that I will carry with me in all my future research endeavours.

Besides my supervisors, I sincerely like to thank the rest of my Doctoral Advisory Committee (DAC) members **Dr. Prasant Kumar Pattnaik** and **Dr. BVVSN Prabhakar Rao** for their productive suggestions throughout during my research. I am also pleased to say thank you to my MEMS group mentors, **Dr. Satish K Dubey**, **Dr. Prasant Kumar Pattnaik**, and not for their important question and motivation, but also for the informative comments that inspired me to extend my study from a range of perspectives. Apart from my supervisors, I am deeply thankful to my senior colleagues, especially Dr. Puneeth SB, for their invaluable guidance in my research endeavors. I also extend my sincere appreciation to Dr. Prakash Rewatkar, Dr. Srikant Sangam, Dr Renuka H and Dr. Mary Salve for their kind support during the initial stages of my PhD journey. My gratitude also goes to Dr. Amreen Ma'am for her valuable suggestions and encouragement. Furthermore, I express my thanks to Dr. Sohan Dudala, Mr. Manish Bhaiyya, Mr. Abhishesh , and Mr. Sai for keeping me inspired in every critical aspect of my research. I would probably not have enough pages to name all of you, but again thanks a lot for helping.

I would like to acknowledge the assistance provided by technician Mr. Sreekanth T in MEMS, Microfluidics and Nanoelectronics Lab and our technical staff of EEE Department and Central Analytical laboratory, without which my work could not be carried out smoothly.

I express my deep gratitude to my esteemed parents, **Mr. Dnyaneshwar Wagh** and **Mrs. Lata Wagh**, who have unwaveringly provided me with their patient support and blessings throughout the entirety of my doctoral program. The tireless efforts and sacrifices made by my mother in caring for my health and education have laid a solid foundation for my future accomplishments. Furthermore, I am indebted to my father for imparting in me the invaluable values of work ethics through his exemplary role modelling. Witnessing his dedication, sincerity, and integrity in his work has instilled in me the qualities of being a better peer and a leader. Without my parents' unwavering guidance, I would not have reached the current juncture in my life, and for that, I am profoundly grateful. I extend my heartfelt thanks to my dear younger brother, **Mr. Himanshu Wagh**, for his unwavering support in all my life choices and showering me with constructive criticism on numerous occasions.

ABSTRACT

Point-of-care (POC) testing has become a critical aspect of the healthcare and food industries. This is because it enables precise and accurate diagnosis of diseases and food conditions. By providing rapid and reliable results at the point of testing, POC testing has revolutionized healthcare delivery and food safety management. Its ability to diagnose diseases and conditions quickly and accurately has made it an indispensable tool in emergency and critical care settings. In the food industry, POC testing is used to ensure the safety and quality of food products by detecting contaminants, allergens, and other impurities. In this context, microfluidic sensory devices have emerged as promising tools for POC applications, due to their ability to detect biological analytes with high sensitivity and specificity in a fast and cost-effective manner.

Such microfluidic devices can be implemented in POC applications through the development of portable and user-friendly devices that can be used by non-expert personnel. These devices can be designed to be handheld or compact, and wireless connectivity to allow for easy data transfer and analysis. Additionally, they can be integrated with microfluidic cartridges/micro trips that contain all required modifications, which can improvise the selectivity and sensitivity to make it occur in the clinical usable range. The sensors can also be designed to be compatible with a variety of sample types, including blood, urine, saliva, and food characterization samples including the milk and different human taste gestures. Overall, the implementation of microfluidic sensors in POC applications has the potential to revolutionize healthcare by providing rapid, precise and accurate diagnosis and monitoring of diseases and conditions in a cost effective area.

Another aspect of this thesis is relying on a single biomarker analysis which can be inadequate for an appropriate diagnosis and treatment monitoring. As a result, it is imperative to concurrently screen multiple analytes, including various disease biomarkers and drugs, with affordable, quick, and reliable quantification. Thus, in recent years, it has become essential to perform simultaneous and multiplexed analysis of various biochemical analytes from a single bodily fluid sample for early diagnosis leading to point-of-care testing (POCT) high electrical conductivity is a prerequisite for electrodes to effectively detect the target analyte with enhanced sensitivity and specificity. Additionally, the electrodes should be cost-effective and facile to fabricate for practical and scalable sensor applications.

Laser-induced graphene (LIG) electrodes have become a popular choice for microfluidic device fabrication due to their unique properties and advantages over traditional electrode materials. LIG is a graphene-like material that is produced by exposing a polymer film to a laser beam, resulting in a highly conductive and porous graphene structure. LIG electrodes are great choice for microfluidic device fabrication due to their benefits such as low cost, high conductivity, high surface area, biocompatibility, ease of integration to the microfluidic level.

As one of the primary work, this thesis describes the realization of a microfluidic device with LIG electrodes, which involves multiple stages including standard microfabrication techniques, laser irradiation, optimization of laser parameters, electrode integration, and functionalization of the sensor surface. The device is designed to selectively capture target analytes with a low detection limit. All these fabrication aspects were accomplished by simple and user-friendly methods like soft-lithography, 3D printing and laser engraving. The developed sensor exhibits high sensitivity, selectivity, and stability, with a detection limit of 10 nM for dopamine and 17 mg/dL for triglyceride which lies in the clinical acceptable range. The proof-of-concept assay platforms can analyse numerous analytes from human serum concurrently and has the ability to detect within the micro-molar range with a broad linear range. The microfluidic design allows for precise control of the sample volume, reducing the required sample volume to microliters. The sensor has potential applications in point-of-care diagnostics, environmental monitoring, and biomedical research. Overall, the microfluidic LIG sensor presented in this study demonstrated high sensitivity, selectivity, and stability for the detection of small biomolecules. And microfluidic design allowed for efficient mass transport and reduced analysis time, making it a promising candidate for precise and accurate biomolecule detection in various applications, such as medical diagnostics and environmental monitoring. The LIG sensor also had several advantages over conventional sensors, including its low cost, ease of fabrication, and versatility. Future studies could focus on further optimizing the performance of the LIG sensor and exploring its potential for other applications.

TABLE OF CONTENTS

CERTIFICATE.....	2
DECLARATION	3
Acknowledgment	4
Abstract.....	6
Table of Contents.....	8
List of Tables	11
List of Figure.....	12
List of Abbreviations	15
Chapter 1: Introduction.....	17
1.1. Antecedents of Microfluidic electrochemical biosensor technology:	17
Electrochemical Biosensor:	18
1.1.1. Microfluidics:.....	18
1.1.2. Point of care devices (PoC):.....	19
1.2. Electroanalytical techniques for the microfluidic biosensor study:	22
1.2.1. Cyclic Voltammetry (CV).....	22
1.2.2. Pulse Technique:.....	23
1.2.2.2. Square–Wave Voltammetry (SWV)	24
1.2.2.3. Electrochemical Impedance Spectroscopy (EIS):	24
1.3. Existing Gaps in the Research:	26
1.4. Objective of the PhD Thesis Work	27
1.5. Organization of Ph.D. Thesis:.....	27
Chapter 2:.....	28
laser ablated microfluidic devices: automated electro microfluidic viscometer for biochemical sensing applications	28
2.1. Introduction.....	28
2.2. Materials, Equipment, and Reagents used	28
2.3. Design of LIG-EMV	29
2.4. Design and Fabrication of LIG based Device:.....	30
2.5. Experimental setup and Operation of LIG-EMV Prototype	32
2.6. Result and Discussion	33
2.6.1. Influence of Flow Rate on Reynold Number	34
2.7. Errors in Measurement of Fluids Viscosity at Different Flow Rate:	37

2.8.	Pressure Gradient Vs Viscosity of Fluids	38
2.9.	Conclusion:	40
Chapter 3:.....		41
Laser Ablated Microfluidic Devices Interdigital Electrodes for Taste Sensing Application in Food Industry		41
3.1.	Design Principle and Materials and equipment:	41
3.2.	Microfluidic LIG-IDE Sensor Design and Fabrication.....	43
3.3.	Experimental Setup:.....	46
3.4.	Result and Discussion:	47
3.5.	Real Sample Analysis:	55
3.6.	Conclusion	57
Chapter 4:.....		58
Stereolithographic microfluidic devices with enhanced Laser-Induced Graphene Bio electrode for Electroanalytical Detection		58
4.1.	Introduction:.....	58
4.2.	Materials and Methods:.....	60
4.3.	Solution and sample preparation:.....	60
4.4.	Synthesis of layer by layer assembly of the bio electrodes:.....	61
4.5.	Fabrication and integration of the bioelectrodes in the microfluidic chambers:	62
4.6.	Material Characterization:.....	63
4.7.	Result and Discussion:	65
4.7.1.	Electro catalytic behaviour of the Biosensor	65
4.7.2.	Effect of varying concentration.....	67
4.7.3.	Simultaneous determination of L-Cysteine, Xanthin, Ascorbic Acid, and Uric Acid at L-Ti ₃ C ₂ -G towards Dopamine detection:.....	68
4.7.4.	Reproducibility, Anti-interference (Selectivity), and Stability properties of biosensor	69
4.7.5.	Real Sample Analysis in Blood Serum and Synthetic Urine	70
4.8.	Conclusion	72
Chapter 5:.....		73
IoT-enabled Electrochemical Sensor Microstrip		73
5.1.	Introduction:.....	73
5.2.	Materials and Method	75
5.3.	Synthesis and fabrication model of the triglyceride biosensor:	75

5.4.	Material Characterization.....	77
5.4.1.	Scanning Electron Microscopy: Impact of H ₂ AuCl ₄ concentration on PDA coating. 77	
5.4.2.	Fourier transforms infrared spectroscopy	78
5.4.3.	UV-Vis Spectroscopy	79
5.5.	Result and Discussion:	80
5.5.1.	Data acquisition and monitoring on smartphone:	80
5.5.2.	Electrochemical response studies and response of LIP/PDA@Au/LIG microstrips and Hanes plot for effect of enzyme activity:.....	81
5.5.3.	Anti-interference and Reproducibility of lipase/PDA@Au/LIG microstrip.....	83
5.5.4.	Determination of triglycerides in human serum sample	84
5.6.	Conclusion	84
Chapter 6: Conclusion and Future Scope.....		85
6.1.	Major Outcomes:.....	86
6.2.	Limitations and Future Scope	86
Reference		88
List of Publications and Patent :		99
List of Patent :		99
Biographies		100
Biography of the Candidate - Ms. Mrunali Wagh		100
Biography of the Supervisor - Dr. Subhendu Sahoo.....		100
Biography of the Co-Supervisor - Dr. Sanket Goel.....		100
Biography of the Co-Supervisor - Michael Dickey		101

LIST OF TABLES

Table 1. 1 Summary of reported research in the Microfluidic biosensor.....	25
Table 1. 2: Calculation of Reynold number for sample fluids and flow rate	35
Table 1. 3: Average time (in a sec) taken by sample fluids for different flow rate in the microchannel	36
Table 2. 1 Dimensions of the Microfluidic LIG-IDE fabricated using CO ₂ Laser Engraver.....	44
Table 2. 2: Summary of research work reported using Interdigitated electrode sensing.	52
Table 4. 1: Comparative assessment of analytical performances of electro-chemical biosensors obtained for dopamine determination based on 2D nanomaterials.....	66
Table 4. 2: Cathodic/anodic peak current and cathodic/anodic peak potential for the electrodes for dopamine.....	67
Table 4. 3: Summary of limit of detection of bioelectrodes towards dopamine	68
Table 4. 4: Real sample sensing of dopamine in blood serum (n = 3) and synthetic urine.....	71
Table 5. 1 Response of triglyceride assay and recovery analysis of blood serum samples	84

LIST OF FIGURE

Figure 1. 1: Schematics of Microfluidic Electrochemical Biosensors	17
Figure 1. 2: Classification of polymer based microfluidic devices depending on the fabrication technology.....	21
Figure 2. 1 Illustration of the design parameters of the microfluidic device. All dimensions are in mm	30
Figure 2. 2 Schematic representation of the proposed and conventional viscometers. (a) Electro Microfluidic viscometer (b) Conventional Ostwald Viscometer	30
Figure 2. 3: Fabrication steps of the EMV device (a) Polyimide sheet was adhered on microscopic glass slide (b) Engraving of LIG electrodes using CO ₂ laser (c) Laser cut straight microchannel on a double-sided tape (d) Enclosing microchannel with PDMS slab.....	31
Figure 2. 5 Complete assembly of the experimental setup.	34
Figure 2. 6 Average time measured for different fluids at a different flow rate	37
Figure 2.7 Measurement of Error percentage in LIG –EMV and Ostwald viscometer	38
Figure 2. 8 Viscosity (cP) Vs Pressure Gradient ($\Delta P/L$) for different fluids	39
Figure 3.1. Schematic of the operating principle of the LIG-IDE Sensor: (a) Operating Principle of the parallel-plate capacitor (b) Rippling Direction of Resultant Electric Field lines that occur within electrode gap.	42
Figure 3. 2: Design of microchannel and Interdigitated electrodes along with dimensions in mm.....	43
Figure 3. 3 Schematics of Fabrication steps pf LIG-IDE sensor(a)PI sheet of 25.4 microns adhered on glass slide(b)Fabrication of Microfluidic Channel(c) Laser engraving of graphene electrodes (d) Enclosing Microchannel with the acrylic sheet (e) Capture Image of the Fabricated LIG-IDE device.	44
Figure 3. 4 SEM images of the fabricated rectangular horizontal microchannel to represent untreated surface on Polyimide sheet. (a) Upper view of the microchannel. (b) Magnified view of laser engraved microchannel.....	45
Figure 3. 5 Scanning electron microscopic images of the fabricated LIG-IDE sensor to characterize graphene on a polyimide sheet. (a) The upper view of electrode fingers with the dimensions is in μm . (b) Top view of laser-induced graphene.	45
Figure 3. 6 Complete Assembly of Experimental Setup.....	46
Figure 3. 7 EIS responses of the LIG-IDE sensor towards citric acid expressed in terms of	48
Figure 3. 8 EIS responses of the LIG-IDE sensor towards sucrose expressed in terms of (a) reactance and (b) resistance for the frequency range.	48
Figure 3. 9. EIS responses of the LIG-IDE sensor towards NaCl expressed in terms of (a) reactance and (b) resistance for the frequency range.....	49

Figure 3. 10 EIS responses of the LIG-IDE sensor towards GMP expressed in terms of (a) reactance and (b) resistance for the frequency range.	49
Figure 3. 11. EIS responses of the LIG-IDE sensor towards L-Tryptophan expressed in term of (a) reactance and (b) resistance for the frequency range.	50
Figure 3. 12 : Analysis of the LIG-IDE sensor responses to several chemicals/samples at different concentrations. Error bar represents the standard deviations for three experiments.	50
Figure 3. 13: EIS responses of the LIG-IDE sensor towards two different chemicals expressed in terms of C for time.	51
Figure 3. 14: EIS responses of the LIG-IDE sensor towards different chemicals expressed in terms of C for time.	53
Figure 3. 15: Sensor response in impedance change toward different analytes at 100 ppm and 50 ppm with NaCl (1000 ppm) as reference analyte. Error bar represents the standard deviations for three independent experiments.	54
Figure 3. 16: Sensor response to different concentration (ppm) in terms of % change in impedance as a reference to NaCl	55
Figure 3. 17: Plot shows the real sample analysis.	55
Figure 3. 18 Impedance spectra in the sensing area for 100 ppm NaCl with fitting curves and inset illustrates equivalent model to present the electric behaviour of sensing area at 100 ppm NaCl.	56
Figure 4. 1 Schematic representation for LBL Synthesis Process for L-Ti ₃ C ₂ -G Bio-Electrode.	61
Figure 4. 2: Schematic illustrates the synthesis of Bioelectrode and fabrication flow of Biosensor (a) Polyamide Sheet (b) Laser engraved Electrodes (c) Ag/AgCl coated Reference Electrode (d) L-Ti ₃ C ₂ -G Working Electrode. (e) Ti ₃ C ₂ Powder (f) Sonication (g) LBL Drop Casting (h) L-Ti ₃ C ₂ Bio-electrode catalytic activity (i) 3-Electrodes on polyamides, (j) 3D printed Microfluidic cap, and (k) Complete prototype of the fabricated biosensor.	62
Figure 4. 3 Scanning Electron Morphology of (a) Ti ₃ C ₂ -G (b) L-Ti ₃ C ₂ -G: Immobilization of laccase on Ti ₃ C ₂ -G (c) L-Ti ₃ C ₂ -G bioelectrode.	64
Figure 4. 4: Spectra of energy dispersive spectroscopy mapping of (a) L-Ti ₃ C ₂ -G (b) Ti ₃ C ₂ -G, (c) XRD patterns of Ti ₃ C ₂ T _x and Ti ₃ AlC ₂	64
Figure 4. 5 Cyclic voltammetry of (a) Optimal L-Ti ₃ C ₂ -G and control electrodes with 1 mM dopamine in pH 7 PBS at 20 mV. Sec-1 for n=2. (b) Scan Rate effects of L-Ti ₃ C ₂ -G in 1mM dopamine concentration from 20-150 mV.sec-1 with inset showing correlating trendline calibration graphs of I _{pa} versus V ^{1/2} oxidation peak currents.	66
Figure 4. 6 Square wave voltammogram of (a) L-Ti ₃ C ₂ -G in PBS with different concentrations of dopamine (1 nM -10 μM) (b) L-Ti ₃ C ₂ -G in PBS with different concentration of dopamine (1 nM -10 μM) (b) L-G in PBS with different concentrations of dopamine (1 μM -10 mM)	67
Figure 4. 7 SWV (I delta Vs E step) for Simultaneous detection analysis of common interferent.	68
Figure 4. 8 (a) Reproducibility of L-Ti ₃ C ₂ -G biosensors for dopamine detection with fixed concentrations of 1mM were used in 0.1 M PBS (b) Anti-interference property of the biosensor (*Do=Dopamine, UA=uricAcid, LC=L-cysteine, Xn=Xanthein, AA=Ascorbic Acid)	69

Figure 4. 9 Stability analysis using SWV plots of L-Ti ₃ C ₂ -G for continuous scanning of 5 cycles.	70
Figure 4. 10 SWV Graph for (a) Blood serum with and without spikes, and (b) Synthetic urine with and without spikes.	70
Figure 5. 1: Mechanism and fabrication stages (a) of bare LIG surface (b) LIP/PDA@Au/LIG electrode synthesis process (c) magnified view of synthesized PDA@Au/LIG (d) layer by layer assembly of final LIP/PDA@Au/LIG electrode (e) Accumulated solution image of PDA@Au as a function of Au concentration (f) Schematic for the lipase immobilization process.	76
Figure 5. 2: Scanning electron microscopy illustrating the synthesis process of the PDA/Aun where n=16 mM, 8 mM, 6 μM (d) magnified view of the lipase immobilization over PDA/Au 6 μM the surface	77
Figure 5. 3 Fourier transforms infrared spectroscopy (FTIR) spectra of PDA/Aun n=16 mM, 8 mM, 6 μM.....	78
Figure 5. 4 UV-Vis absorption spectra of the PDA@Aun n=16 mM, 8 mM, 6 μM as a function of the increasing concentration of the Au.	79
Figure 5. 5: (a) LIP/PDA@Au/LIG microstrip inserted to the electrochemical analyzer with selected cyclic voltammetry mode (b) Smartphone is tapped on the application to receive data (c) Electrochemical analyzer receive power from smartphone; (d) sample drop on the detection zone (e) Receive signal display as concentration on smartphone application.	80
Figure 5. 6 Cyclic voltammetry of (a) LIG, PDA@Au/LIG, and LIP/PDA@Au/LIG microstrip in PBS (50 mM, pH 7.0) at the scan rate of 20 mV/s (b) Scan rate analysis of PDA@Au/LIG with a scan rate of 20 mV/s to 280 mV/s.....	81
Figure 5. 7: Cyclic voltammetry of (a) LIG, PDA@Au/LIG, and LIP/PDA@Au/LIG microstrip in 200 mg/dL triglyceride at the scan rate of 20 mV/s (b) Concentration analysis varies from 20 mg/dl to 100 mg/dl with the scan rate of 20 mV/s (c) Calibration plot for concentration of 20 mg/dl to 100 mg/dl. (d) Study of Hanes plot for the concentration of substrate [S] and [S]/current in mA.	82
Figure 5. 8: (a) Anti-interference plot for the triglyceride with interferent of UA, UR, Gl, and all composition in TG (b) Reproducibility analysis for the four devices.....	83
Figure 6. 1: Summary of the outcomes of this thesis is illustrated in the accompanying flowchart.....	85

LIST OF ABBREVIATIONS

3D Printing: Three-Dimensional Printing

CE: Counter Electrode

WE: Working Electrode

RE: Reference Electrode

SLA: Stereolithographic

CV: Cyclic Voltammetry

DPV: Differential Pulse Voltammetry

SWV: Square-Wave Voltammetry

EC: Electrochemistry

LIP: Lipase

LAC: Laccase

PDA: Polydopamine

AA: Ascorbic Acid

UA: Uric Acid

Lc: L-Cystein

Xn: Xanthein

Au: Gold

NP: Nanoparticle

EIS: Electrochemical Impedance Spectroscopy

IDE: Interdigitated Electrodes

LED: Light Emitting Diode LIG: Laser Induced Graphene

PBS: Phosphate Buffer Solution

PDMS: Polydimethylsiloxane

PI: Polyimide

PoC: Point of Care

PoS: Point of Source

RE: Reference Electrode

Re: Reynold's Number

SEM: Scanning Electron Microscope

UV: Ultraviolet

WE: Working Electrode

XPS: X-Ray Photoelectron Spectroscopy

XRD: X-Ray Diffraction

CHAPTER 1: INTRODUCTION

1.1. Antecedents of Microfluidic electrochemical biosensor technology:

In the current era, the fields of electrochemistry, biosensors, and microfluidics are increasingly intertwined, challenging the notion of their distinctness. The Venn diagram in Figure 1. 1 illustrates how these intersections can be further categorized into four application areas: electrochemistry and biosensors, electrochemistry and microfluidics, microfluidic biosensors, and microfluidic electrochemical biosensors. In this context, our focus is on dynamic interplay between electrochemistry, biosensors, and microfluidics, particularly in the emergence of novel application areas such as "point-of-care" diagnostics, where traditionally laboratory-based measurements are conducted in field settings.

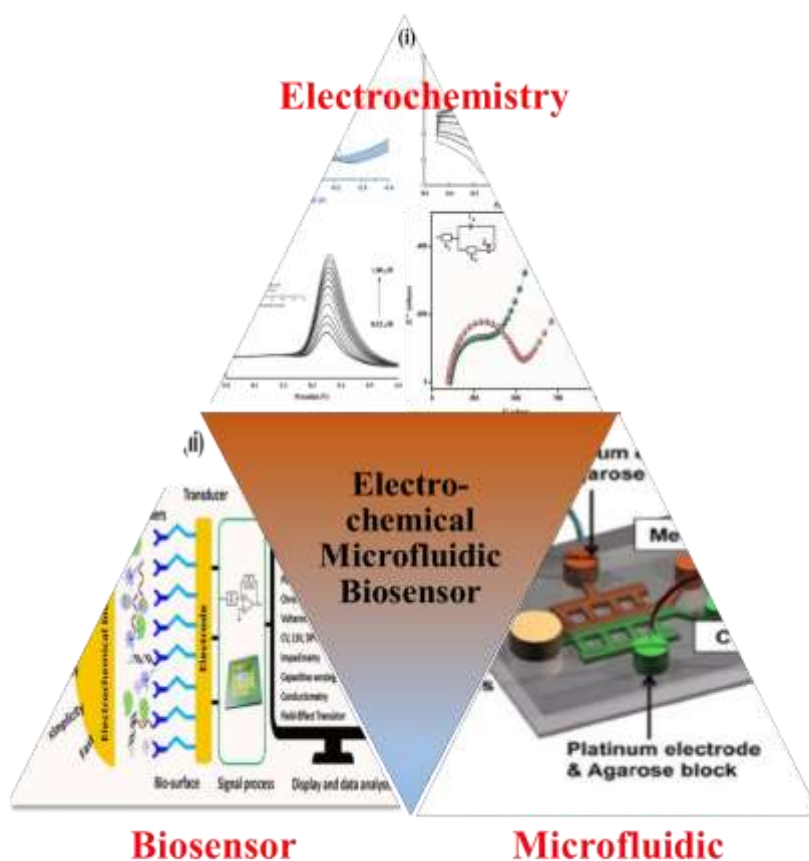


Figure 1. 1: Schematics of Microfluidic Electrochemical Biosensors

Electrochemical Biosensor:

An electrochemical biosensor uses electrical signals, such as voltage, current, or impedance, to detect biological entities[1], [2]. The biosensor contains a biological entity, such as an enzyme, protein, virus, or antibody, which reacts with the target molecule and generates an electrical signal. The electrode is a critical component of the electrochemical biosensor, as it controls the flow of electrons and bioagents. The first electrochemical biosensor was created by Clark to monitor glucose levels in human blood serum. Since then, electrochemical biosensors have been developed to detect various biological entities, making them highly versatile and useful tools in biomedical research, clinical diagnostics, environmental monitoring, and food analysis. This introduction section will discuss various electrochemical biosensors that have been developed to detect different biological entities. The technology behind electrochemical biosensors has undergone significant advancements in recent years, leading to improved accuracy, sensitivity, and selectivity of these devices.

Enzymatic sensing of biomolecules is a commonly used technique in biosensing and diagnostic applications. In enzymatic sensing, an enzyme is used to catalyze the reaction of a target biomolecule, such as glucose, lactate, or cholesterol. The enzyme converts the target molecule into a product that can be electrochemically detected. The product or the enzyme itself can be immobilized on an electrode surface to form a biosensor. During the CV scan, the potential is cycled between two values, causing the oxidation or reduction of the electroactive species on the electrode surface. The resulting current is measured and plotted against the potential. When the enzyme catalyzes the reaction of the target biomolecule, the product is generated on the electrode surface, leading to a change in the electrochemical response. This change can be detected and quantified, providing information about the concentration of the target biomolecule. The sensitivity of enzymatic sensing can be enhanced by optimizing the immobilization of the enzyme or the product on the electrode surface and by optimizing the experimental conditions, such as pH, temperature, and scan rate. The selectivity of enzymatic sensing can be improved by using enzymes with high specificity for the target biomolecule and by incorporating selectivity-enhancing elements, such as enzyme immobilization matrix, into the biosensor. Overall, cyclic voltammetry is a versatile and powerful technique for the enzymatic sensing of biomolecules and has wide applications in biomedical research, clinical diagnostics, and environmental monitoring.

1.1.1. Microfluidics:

As discussed in the previous sections, working with the biological entity required contamination free environment, low sample requirement and sensitivity. Microfluidics is a field of science and technology that deals with the behavior, manipulation, and control of fluids at the micrometer scale. It involves the study and application of fluid mechanics, electromechanical systems, and fabrication techniques to

create miniaturized devices and systems that can handle small volumes of liquids or gases. The Reynolds number (Re) is a key parameter that governs the flow behaviour in microfluidic systems. In microscale channels, the Reynolds number is typically low, and the flow is dominated by viscous forces. This results in laminar flow, where fluid streams flow in parallel layers with minimal mixing. Laminar flow is commonly used in microfluidic applications for precise fluid handling, such as in chemical reactions, cell analysis, and droplet generation. Re is an important dimensionless parameter in microfluidics that characterizes the relative importance of inertial forces to viscous forces in fluid flow. It is defined as the ratio of inertial forces to viscous forces and is given by the formula:

$$Re = \rho v d / \mu$$

where:

ρ is the density of the fluid

v is the velocity of the fluid

d is a characteristic length scale (e.g., diameter or height of a microchannel)

μ is the dynamic viscosity of the fluid

Microfluidic devices are typically fabricated using microfabrication techniques such as soft lithography, micro-milling, and micro-electromechanical systems (MEMS) fabrication. These techniques enable the creation of microchannel, microstructures, and micro features with high precision, which are essential for microfluidic devices.

1.1.2. Point of care devices (PoC):

Point of care devices (PoC) is a boon to the medical healthcare system, solving basic needs and easy affordability, allowing quicker disease diagnostics and monitoring of patients. In recent progress, miniaturized versions of the mainframe technologies are found on larger benchtops [3]. PoC devices are more straightforward and smaller than their predecessors [4]. Other beneficial features of PoC devices include the highest rate of sensitivity at the most negligible maintenance costs and target-specific selectivity at reduced sample consumption [5]. However, demanding PoC devices are an immediate requirement for hassle-free fabrication methodologies. It also poses a significant challenge in identifying fabrication methods and integrating required sensing techniques for practical PoC developments. A biosensor integrated with a microfluidic chip for POCT diagnosis meets the requirement for rapid detection and has become a hot topic of research. The combination of microfluidic technology and advanced bio-sensing technology has led to the invention of many outstanding miniaturized analytical platforms that can achieve precise control of micro/nano liquids and integrate various types of biological arrays on a miniaturized platform.

Such microfluidic integrated biosensor device has many advantages, such as low reagent consumption, shorter reaction time, automated sample preparation, high-throughput analysis, minimal hazardous material handling, parallel detection, high detection accuracy, and flexible design and miniaturization, portability, low cost, and one-time use [6]–[8]. The fabrication of electrochemical biosensors with integrated microfluidics requires careful consideration of several technical aspects. Material selection is critical, as the materials must be biocompatible, chemically stable, and should not interfere with the electrochemical measurements. Additionally, the choice of electrode material and design can significantly impact the performance of the biosensor. The fabrication process must also ensure precise alignment and sealing of the microfluidic channels to the electrode, which can be challenging due to the small dimensions of the channels. The integration of microfluidics can introduce noise into the electrochemical signal, and efforts must be made to minimize this noise through careful design of the microfluidic channels and the use of appropriate flow rates. Signal amplification and detection methods must also be carefully selected and optimized to achieve high sensitivity and accuracy. Finally, the miniaturization of the biosensor is an important consideration, as smaller devices can improve portability and reduce costs. However, miniaturization can also introduce challenges such as reduced sensitivity and increased complexity in fabrication. By carefully considering these technical aspects, researchers can develop innovative and effective electrochemical biosensors with integrated microfluidics for a range of applications.

Different fabrication techniques used in the production of microfluidic devices. Two traditional fabrication techniques for microfluidic chips are photolithography and etching, which are used on silicon and glass chips. The process of soft-lithography is time-consuming, requires multiple fabrication steps, and is difficult to transport due to the involvement of fragile substrates [9]. Further, state-of-the-art identified various widely leveraged substrate materials to fabricate PoC devices, including polymer plastics, zero conductive polymers (polyimide (PI), polyethylene terephthalate (PET), SiO₂ glass (silica), paper, and polymethylmethacrylate (PMMA) [10]–[12]. Compared to conventional silicon, the affordability and wide availability of nonconductive polymers at a significantly lower cost of production attract researchers to adapt for device fabrications [13], [14].

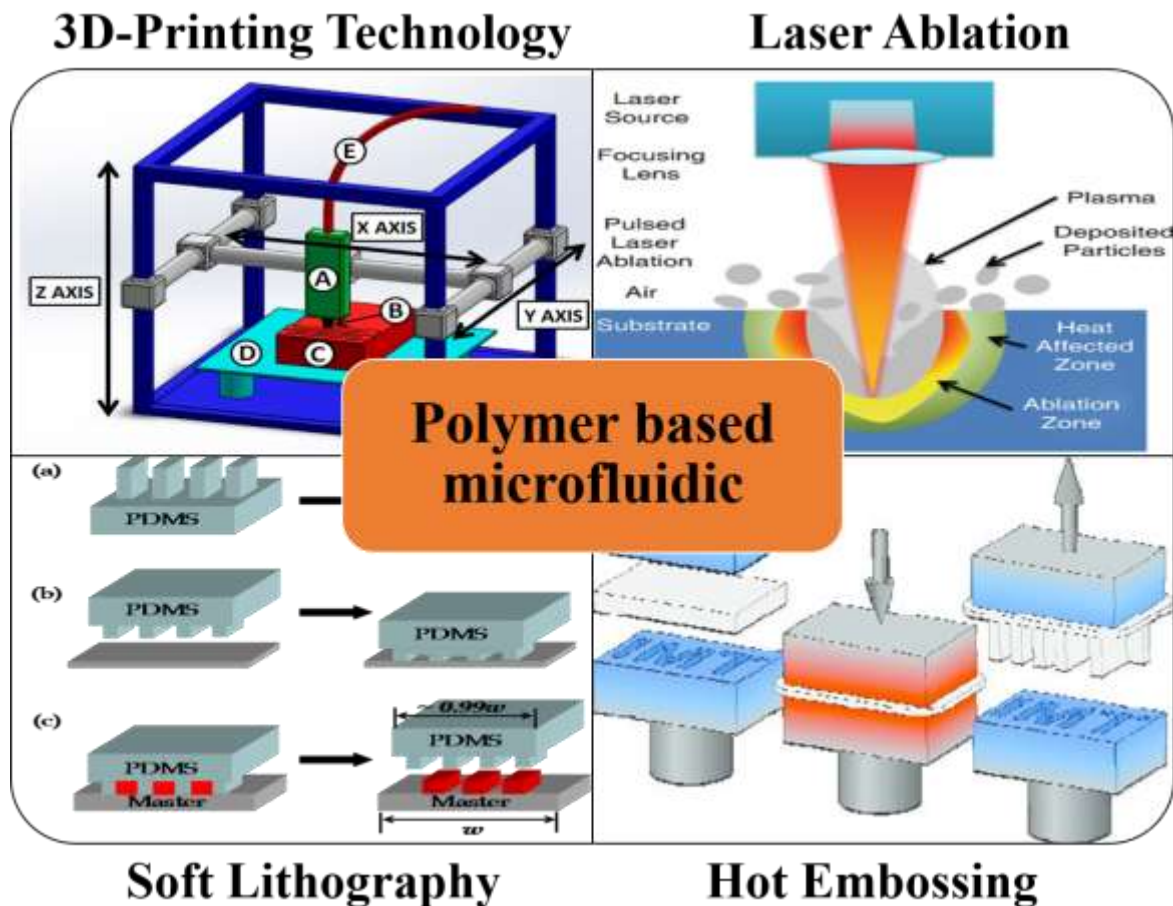


Figure 1. 2: Classification of polymer based microfluidic devices depending on the fabrication technology

An efficient microfluidic device ensures prior substrate selection, adequate device dimensions, and feasibility of integration into detection units. However, with the emergence of polymer-based microfluidic chips, various other fabrication technologies such as injection molding, molding, hot pressing, soft lithography, laser ablation, photolithography galvanofomung abformung (LIGA), 3D printing, and others are being increasingly used to fabricate microfluidic chips requirements [15]–[17]. This growing trend towards using these alternative fabrication techniques to conventional technique, which are suited to the production of polymer-based microfluidic chips. The widely adaptable most recent fabrication methods include laser-assisted fabrications [18], additive fabrication (3D printing) [19], and resin-based encapsulations (laminations) [20] as shown in Figure 1. 3 also summarized in Table 1. 1. This thesis focuses on the technical development of a microfluidic biosensor utilizing graphene as the sensing material, which is enabled by Internet of Things (IoT) technology. This thesis discusses the fabrication and optimization of the biosensor, as well as its performance in detecting various biomolecules. Additionally, the integration of IoT technology and its impact on biosensor performance, sensitivity, and selectivity will be explored. The potential of an IoT-enabled graphene-based microfluidic biosensor to revolutionize the field of biosensors by providing real-time monitoring

and remote data analysis capabilities is highlighted. The findings of this thesis will provide valuable insights into optimizing the performance of graphene-based biosensors and integrating IoT technology in biosensor applications.

1.2. Electroanalytical techniques for the microfluidic biosensor study:

1.2.1. Cyclic Voltammetry (CV)

Cyclic Voltammetry is a widely used electrochemical technique that measures the current generated by an electrochemical cell as a function of an applied potential. It works by applying a potential to the working electrode while the current is measured between the working electrode and a reference electrode. In a typical enzymatic sensing experiment using cyclic voltammetry, a three-electrode electrochemical cell is used, consisting of a working electrode, a reference electrode, and a counter electrode. The working electrode is usually modified with the enzyme or the product of the enzymatic reaction. The reference electrode is used to measure the potential of the working electrode, while the counter electrode provides the current necessary to maintain a constant potential.

The potential is then scanned linearly in the opposite direction, and the current is again measured. Subsequently, the potential is scanned back to its original value, and the process is repeated. During the potential scan, electrochemical reactions occur at the working electrode. If the electrode is a reactive species, such as a metal, an oxidation or reduction reaction will occur. The current generated by the reaction is directly proportional to the rate of the reaction, and the potential at which the reaction occurs is related to the free energy of the reaction. By measuring the current as a function of the applied potential, cyclic voltammetry can be used to determine the kinetics and thermodynamics of the electrochemical reaction. CV can also be used to study the electrochemical behaviour of complex systems, such as electrochemical cells with multiple redox couples or systems with chemical reactions that compete with the electrochemical reactions. By varying the scan rate and other experimental parameters, it is possible to obtain detailed information about the electrochemical behaviour of a system. Overall, cyclic voltammetry is a powerful tool for studying electrochemical systems and has applications in many fields, including electrochemistry, materials science, and biochemistry.

$$E = E^0 + \frac{RT}{nF} \ln \frac{C_o}{C_R} \quad (1)$$

The Nernst equation (eqn (1)) describes how the electric potential, denoted as E, and the concentrations of species undergoing oxidation or reduction (C_o , C_R) change in response to an applied electric potential between the working electrode (WE) and reference electrode (RE). This relationship is applicable to most electrochemical applications where the analyte participates in a redox reaction due to the electric potential. In voltammetry, similar to amperometry, a potential difference (E) is applied between the working electrode (WE) and counter electrode (CE), and the resulting current (I) is measured. However, unlike amperometry, in voltammetry, the potential (E) is varied over time. For instance, in cyclic

voltammetry, E is swept in a linear cycle at a specific scan rate (v). When E becomes more positive, the analyte undergoes oxidation, and when E becomes more negative, the analyte undergoes reduction, each resulting in a peak current (i_p) associated with the oxidation and reduction steps.

The correlation between i_p and v is specified by the Randles–Sevcik equation (2):

$$i_p = (2.69 * 10^5)ACD^{1/2}n^{3/2}v^{1/2} \quad (2)$$

here A = electrode area, C = concentration of analyte in bulk solution, D = diffusion coefficient of the analyte, and n = number of electrons involved in the reaction. The magnitude of i_p used to determine analyte concentration, and the potential which the analyte is oxidized/reduced utilized for qualitative identification.

1.2.2. Pulse Technique:

1.2.2.1. Differential Pulse Voltammetry

Pulse Technique Differential Pulse Voltammetry (PT-DPV) is a widely used electrochemical technique for detecting and quantifying electroactive species in a solution. This technique is based on the application of a series of voltage pulses to a working electrode immersed in the solution of interest. During the measurement, a potential pulse is applied to the working electrode and a current response is recorded as a function of time. The pulse is typically of short duration (few milliseconds to microseconds) and small amplitude (a few millivolts), and is followed by a short period of rest, during which no potential is applied. The pulse causes the electroactive species in the solution to undergo oxidation or reduction reactions at surface of the working electrode, causing in a change in the current passing through the electrode. The magnitude of this change in current is proportional to the concentration of the electroactive species in the solution.

The PT-DPV technique is known for its ability to resolve overlapping voltammetric peaks and to provide superior sensitivity and selectivity for the detection of electroactive species in a solution. This is achieved by applying a series of closely spaced potential pulses of different amplitudes, each followed by a short rest period. The differential current response is then obtained by subtracting the current obtained during the rest period from the current obtained during the pulse period. This differential signal is used to obtain a highly resolved voltammetric curve, which can be used to identify and quantify electroactive species in the solution. In summary, PT-DPV is a highly sensitive and selective electroanalytical technique that is widely used for the detection and quantification of electroactive species in a solution. Its ability to resolve overlapping peaks and to provide highly resolved voltammetric curves makes it a valuable tool in a wide range of applications, including environmental monitoring, pharmaceutical analysis, and biochemical research.

1.2.2.2. Square–Wave Voltammetry (SWV)

Square-wave voltammetry (SWV) is a technique used in electrochemical analysis to study the behaviour of electroactive species in solution. It is a type of cyclic voltammetry that involves applying a square-wave potential waveform to an electrode in a solution containing the electroactive species of interest. An electrochemical cell is set up, containing an electrode (usually a working electrode made of a conductive material such as platinum or gold), a reference electrode (often a saturated calomel electrode, SCE), and a counter electrode (usually a platinum wire). The working electrode is immersed in the solution containing the electroactive species, and a potential difference is applied between the working electrode and the reference electrode.

The potential is scanned at a high rate (typically several hundred volts per second) over a range of values, such that the potential waveform resembles a square wave. The potential is then held at a fixed value for a short period (typically a few milliseconds) before being reversed and scanned back to the original potential. The resulting current is measured at each potential value and plotted as a function of the applied potential. The resulting plot is a series of peaks and valleys that correspond to the redox reactions of the electroactive species in solution. The peak current is proportional to the concentration of the electroactive species, making SWV a useful technique for quantitative analysis. Overall, SWV provides a highly sensitive and selective method for the detection and quantification of electroactive species in solution. It is widely used in various fields such as analytical chemistry, biochemistry, and materials science.

1.2.2.3. Electrochemical Impedance Spectroscopy (EIS):

Enzymatic sensing involves the use of enzymes as the recognition element to selectively detect and quantify a target analyte. Enzymatic sensors typically consist of an electrode surface that is functionalized with an enzyme and a transducer that converts the biochemical reaction between the enzyme and analyte into an electrical signal. EIS can be used to study the properties of the enzyme-modified electrode surface, including the charge transfer resistance, double-layer capacitance, and any adsorption or desorption processes occurring at the surface. The impedance spectrum obtained from the EIS measurements can provide information about the enzymatic reaction kinetics, as well as the stability and performance of the enzymatic sensing interface.

The basic principle of EIS for enzymatic sensing involves applying a small AC voltage to the enzyme-modified electrode surface and measuring the resulting current response at different frequencies. The impedance spectrum obtained from the EIS measurements can be analyzed using mathematical models and simulation tools to extract information about the electrochemical behaviour of the enzyme-modified electrode surface and the enzymatic reaction kinetics. By monitoring changes in the impedance spectrum over time, EIS can provide information about the presence and concentration of the target analyte, as well as the sensitivity and selectivity of the enzymatic sensor. EIS can also be used to

optimize the performance of enzymatic sensors by studying the effect of different experimental conditions, such as the concentration of the enzyme, the pH and temperature of the solution, and the presence of interfering species. In summary, EIS is a valuable tool for the characterization and optimization of enzymatic sensors, as it can provide information about the electrochemical behaviour of the enzyme-modified electrode surface and the enzymatic reaction kinetics, which is critical for the development of high-performance enzymatic sensors for a wide range of applications.

Table 1. 2 Summary of reported research in the Microfluidic biosensor

Sr.no	Fabrication Technique	Percentage Error	Sample volume requirement	Cost of device	Application	Reference
1	Screen-Printing on Paper	±7%	20 µl	US\$ 8	Bio sensing	[21]
2	Micro pillar using Al mold	2.6–18.5%	80–400 µl	NA	Biomedical application	[22]
3	3-D Printed Paper Micro strips	±8%	20 µl	NA	Biomedical application	[23]
4	Wax printing technique on paper	8%	10 µL	NA	Milk Adulteration	[24]
5	3D printing	15 %	1–10 µl	NA	Biomedical application	[25]
6	Soft lithography techniques	10%-30%	1.5 mL	NA	Industrial application	[26]

1.3.Existing Gaps in the Research:

- **Sensitivity and Detection Limits:** While microfluidic biosensors offer high sensitivity in many cases, there is still room for improvement, especially for the detection of low-concentration analytes. Enhancing the sensitivity and lowering the detection limits of microfluidic biosensors remains a challenge, as it requires overcoming issues such as non-specific binding, signal amplification, and background noise.
- **Standardization and Reproducibility:** There is a lack of standardization and reproducibility in microfluidic biosensor research, making it difficult to compare results from different studies. Standardization of fabrication techniques, assay protocols, and data analysis methods would enable more reliable and consistent results, and facilitate the translation of microfluidic biosensors from research to practical applications.
- **Integration and Automation:** Integrating various components such as sample preparation, analyte capture, and signal transduction into a single microfluidic biosensor platform is a challenge. Achieving seamless integration and automation of these components would simplify the workflow and enable efficient and reliable operation of microfluidic biosensors in real-world settings.
- **Long-term Stability and Durability:** Ensuring the long-term stability and durability of microfluidic biosensors is critical for their practical use. Issues such as biofouling, device degradation, and shelf-life need to be addressed to ensure the reliable and robust operation of microfluidic biosensors over extended periods of time.
- **User-Friendly Interfaces:** The user-friendliness of microfluidic biosensors is an important factor for their widespread adoption. Designing intuitive and user-friendly interfaces, such as simple sample loading, easy-to-interpret results, and minimal user intervention, would enhance the usability and accessibility of microfluidic biosensors for end-users.

1.4.Objective of the PhD Thesis Work

This study intended to develop a cost-efficient, miniaturized / microfluidics electro-analytical biosensor devices. The overall objectives of this work are as mentioned below:

- Fabrication and characterization of microfluidic / miniaturized electro-analytical platform for biosensing application
- Enhancement the performance with different electrode materials.
- Automation and optimization of microfluidic electro-analytical biosensor using real samples.
- Development of an integrated and automated microfluidic prototype with electrode and use it for electro-analytical biosensing applications.

1.5.Organization of Ph.D. Thesis:

This Ph.D. thesis, based on the objective mentioned above, are arranged as chapters in an organized manner. In chapter 2, a meticulous report of materials and methods used for fabrication of microfluidic / miniaturized laser induced graphene portable platforms. And aims to explore the development and optimization of an IoT-enabled graphene-based microfluidic biosensor for the detection of various biomolecules. Chapter 3 and 4 introduces the fabrication process of the taste and biosensor, including the preparation and surface modification of graphene, microfluidic chip fabrication, and immobilization of biomolecules on the graphene surface. The optimization of the biosensor performance, such as its sensitivity, selectivity, and dynamic range, are also be investigated. Chapter 5 furthermore, the integration of IoT technology into the biosensor will be explored, which includes the design and development of an IoT platform for real-time data acquisition, analysis, and remote monitoring. The impact of IoT technology on the performance of biosensors, such as its response time, accuracy, and reliability, has been evaluated. Finally, Chapter 6 draws the summary of this work and future opportunity for further improvement of POCT devices.

CHAPTER 2:

LASER ABLATED MICROFLUIDIC DEVICES: AUTOMATED ELECTRO MICROFLUIDIC VISCOMETER FOR BIOCHEMICAL SENSING APPLICATIONS

2.1. Introduction

The development of a desired microfluidic device with suitable constituents, like microchannel and electrodes, is crucial for realizing the true potential of microfluidic sensors. However, the conventional screen-printing techniques, though provides easy and aligned micro patterning technique, carries disadvantages such as expensive process, requirement of multiple steps and skilled personnel. In order to overcome these limitations, the current chapter discusses the utilization of CO₂ laser engraving technique, for fabricating features in micron dimensions of channel as well as the electrodes. Major advantages of this technique are the elimination of mask, cost-effectiveness and design scalability. Electrode patterns with different dimensions and geometries can be fabricated using this technique, which are greatly influenced by several laser parameters such as the intensity of the laser, speed of the stage (substrate), and focus level of the laser.

In fluid rheological studies, viscosity measurement is one of the most significant phenomena leveraged in a variety of studies. Viscometers are broadly employed in a wide range of sensing and monitoring applications, such as biochemical diagnostics and numerous adulteration detections. Therefore, it is pertinent to develop a miniaturized, automated, and cost-effective device that can measure the fluid viscosity from small samples. In this context, this chapter discusses fluid viscosity measurements by a low-cost automated electro-microfluidic viscometer (EMV) fabricated on a hydrophilic laser-induced graphene (LIG) platform with integrated electronics to monitor viscosity from a small sample of fluid of 1.5 μL . The principle of operation of the fabricated device is based on the modified Hagen–Poiseuille equation, which imitates the Ostwald viscometer. Under laminar flow, the proposed standalone and portable device automatically evaluates the travel time of fluid with high accuracy. This travel time was used to obtain viscosity accurately of various fluids, such as water, milk, and acetic acid, with a minimum error of up to $\pm 1.08\%$. Overall, the device provides a pathway for a convenient, robust, and plug-and-play platform for different applications, including various adulteration monitoring and bio sensing.

2.2. Materials, Equipment, and Reagents used

A PI sheet of thickness 25.4 μm was procured from Dali Electronics, India, and a 30-W CO₂ Laser Engraver (VLS 3.60 from Universal Laser Systems, AZ, USA) was used to form the LIG zones. The conductivity and the sheet resistance of the fabricated LIG-based electrodes were measured using the four-probe measurement (Ossila) technique. Furthermore, the height of the fabricated microfluidic channel was measured to be 35 μm by utilizing a Surface Profilometer (SJ-210 from Minutolo, Japan).

Benchtop Ostwald viscometer (Length of 290 mm, Capillary diameter of 0.4 mm, and time of water flow is 200–300 s) was procured from Sigma Aldrich, India. Glacial Acetic acid (99%–100%) and PDMS, Sylgard184 silicone elastomer kit, were procured from Sigma Aldrich. Pressure Sensors MPR 210 Series was purchased from Honeywell.

2.3. Design of LIG-EMV

The flow dynamics in a rectangular microchannel was designed based on the Hagen – Poiseuille Law which is given as[27]

$$\mu = \frac{H^2 \Delta P}{12 v_a L} \quad (1)$$

where μ denotes the viscosity of the fluid, ΔP is the pressure difference at the ends, v_a was the average velocity of the sample fluid in the channel, H is the height of the rectangular microchannel, L denotes the length of the microchannel. Using the Hagen-Poiseuille equation, it was proven that the viscosity is directly related to the time taken by the fluid to cover a fixed distance [28]. So, for a reference fluid and sample fluid, equation (1) can be written as

$$\frac{\mu_a}{\mu_b} = \frac{\Delta t_a}{\Delta t_b} \quad (2)$$

where μ_a is the viscosity of reference fluid and μ_b is the viscosity of sample fluid and Δt_a and Δt_b are the time taken by reference fluid and sample fluid respectively to travel between two consecutive electrodes separated with a known distance. Based on equation (2), a microfluidic device was designed, with the dimension of the microchannel as 1.5 mm × 0.035 mm × 26 mm as indicated in Figure 2. 1. This microfluidic device emulated a conventional Ostwald viscometer to measure viscosity. The schematic of the device and the traditional Ostwald viscometer are shown in Figure 2. 2 (a) and (b), respectively.

In this device, the average time (Δt) taken by the fluid to travel between the equidistance electrodes (A, B, C, and D) can be measured as

$$\Delta t = \frac{\Delta t_1 + \Delta t_2 + \Delta t_3}{3} \quad (3)$$

where, Δt_1 , Δt_2 , Δt_3 are the time taken to travel the fluid from A to B, B to C, and C to D, respectively. Here, the distances AB, BC, and CD are equal. As discussed above, a sample fluid will be made to flow and the average time taken to travel between two adjacent electrodes will be obtained. This average time can be used to find the viscosity using Equation (2).

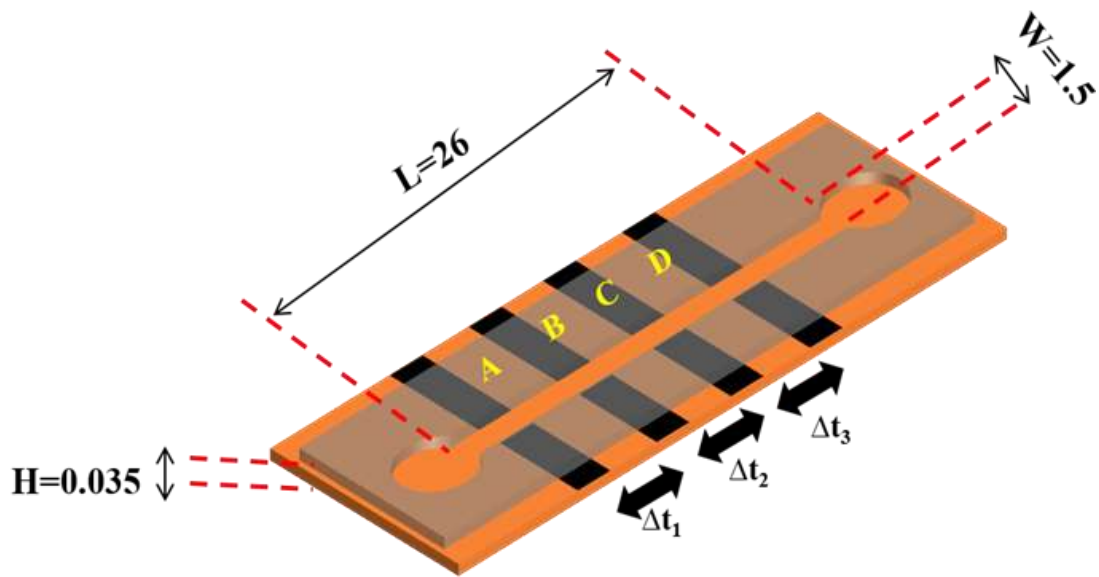


Figure 2. 1 Illustration of the design parameters of the microfluidic device. All dimensions are in mm

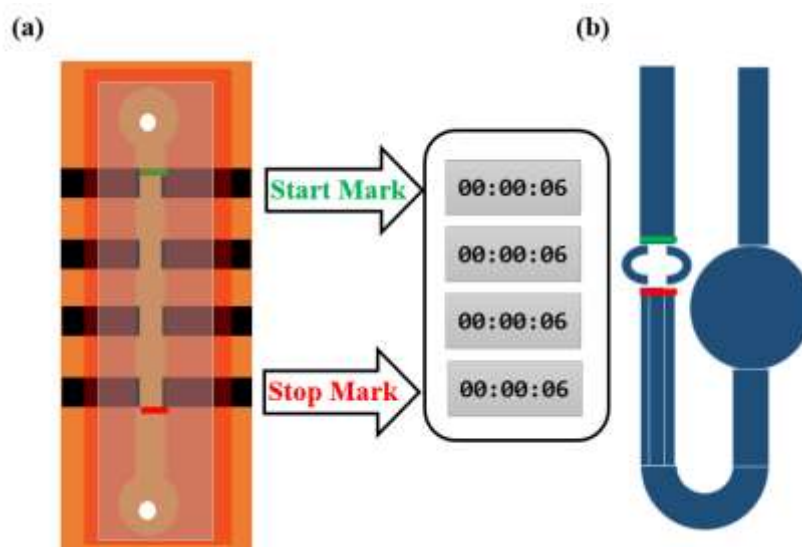


Figure 2. 2 Schematic representation of the proposed and conventional viscometers. (a) Electro Microfluidic viscometer (b) Conventional Ostwald Viscometer

2.4. Design and Fabrication of LIG based Device:

The LIG-EMV was fabricated using a CO₂ laser. First, the design of LIG electrodes was created using Corel Draw software and saved in .dxf format, which was fed to the CO₂ laser. Figure 2. 3 illustrates the step-by-step fabrication flow of LIG –EMV. The optimized laser parameters, such as 6.5 W power and 4.5 cm/s speed, were chosen as per our previously published research work[29]. Before the laser exposure, the polyimide sheet was ultrasonically washed in a solution of absolute isopropyl alcohol

(IPA) and dried at 50°C before being adhered to the microscopic glass slide to provide good strength, as shown in Figure 2. 3 (a).

Subsequently, the PI sheet was placed inside the CO₂ laser engraver for electrode fabrication. With optimized speed and power, LIG electrodes were formed as shown in Figure 2. 3 (b). Using the optimized speed and power of the laser machine, graphitized zones were formed at the positions where the intersecting electrodes were required.

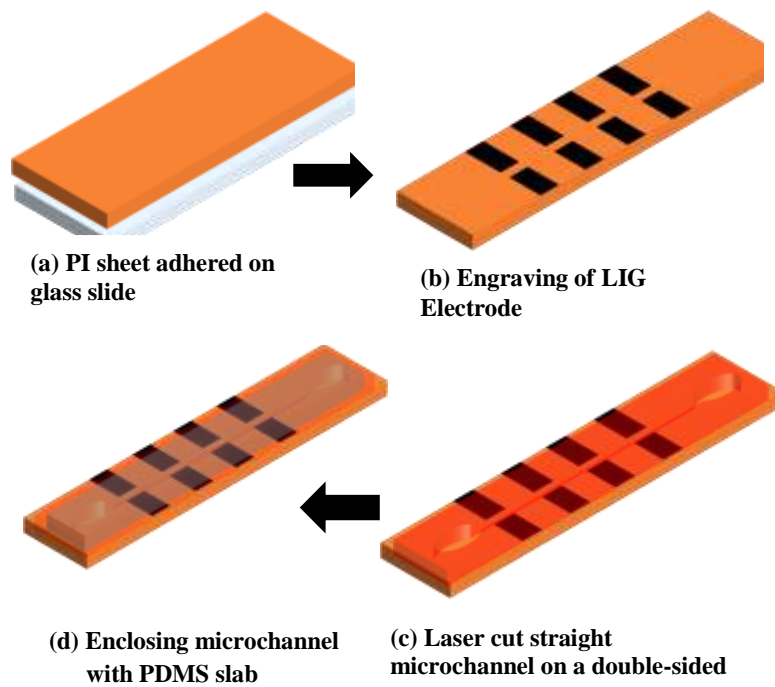


Figure 2. 3: Fabrication steps of the EMV device (a) Polyimide sheet was adhered on microscopic glass slide (b) Engraving of LIG electrodes using CO₂ laser (c) Laser cut straight microchannel on a double-sided tape (d) Enclosing microchannel with PDMS slab

The microfluidic device with rectangular microchannel and electrodes were fabricated on the same layer of the PI sheet by deploying the optimal height of laser-induced graphene electrodes. The height obtained for the fabricated microchannel was approximately 35 μm . The microfluidic device was capped soft-lithographically by bonding the PDMS layer with a double-sided thin adhesive tape. The microchannel was freed from the leakage after bonding with the PDMS and double-sided thin adhesive tape[30]. The bonding process of the PDMS slab and LIG electrodes is shown in Figure 2. 3 (c) and (d). For achieving a leakage-proof connection between microchannel and tubing, pipette tips were used. Prior to commencing the experiment, the peristaltic pump was used to introduce standard distilled water into the horizontal rectangular microchannel. Since the microchannel consisted of the untreated surface with a straight geometry, non-interrupting flow in between the microchannel was observed. The pump revolution per minute (RPM) and therefore, the flow rate was improved steadily in the range of 70 –

210 $\mu\text{l}/\text{min}$. Before employing a new flow rate, the system was made to run for about 2 min to get a stable flow rate value.

2.5. Experimental setup and Operation of LIG-EMV Prototype

A schematic diagram of the complete LIG-EMV device setup for viscosity measurement is shown in Figure 2. 4. As can be seen, one side of the conductive electrode has been coupled to the positive terminal of the power supply, and subsequently, uniformly spaced conductive electrodes were associated to a microcontroller the Arduino Nano board. An analog input port of Arduino Nano was used to sense the voltage impulse obtained from the viscometer.

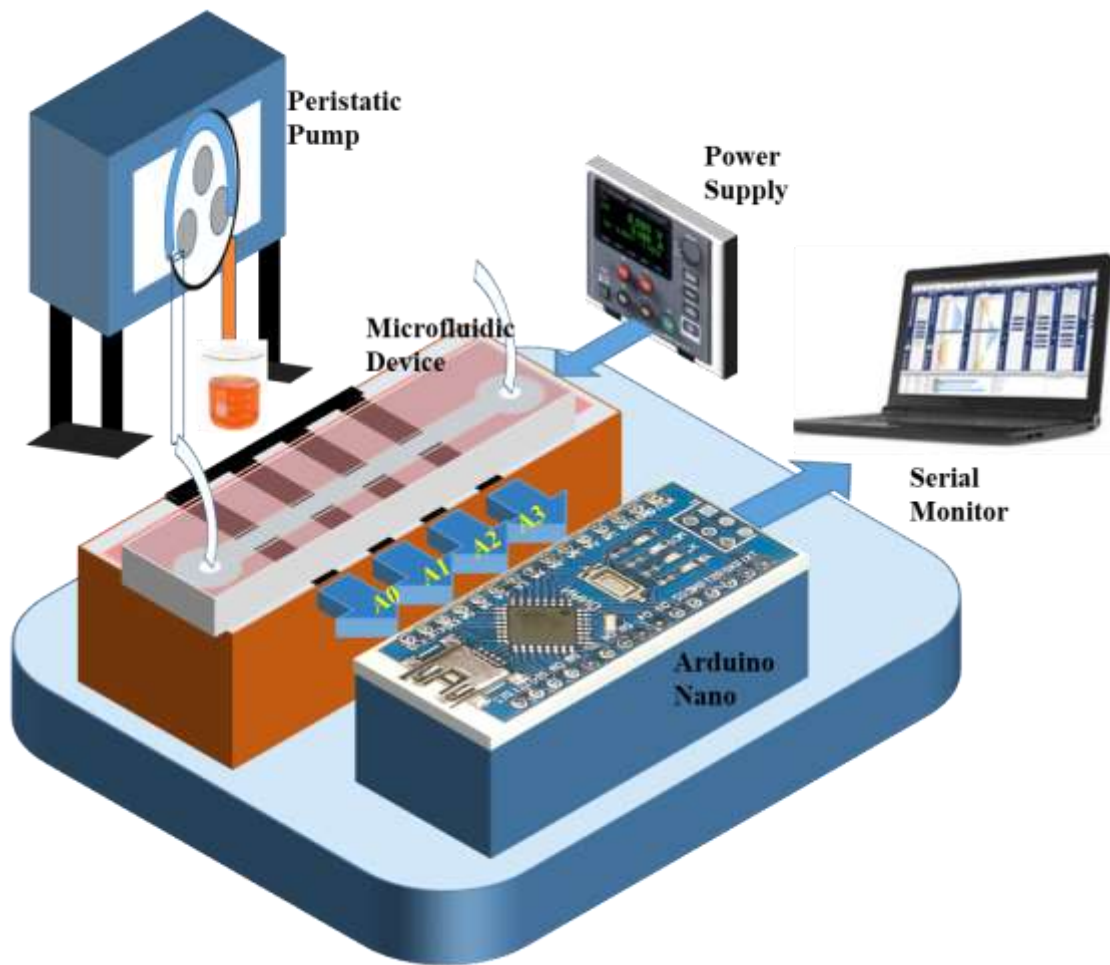


Figure 2. 4: Block Diagram of Complete EMV device prototype

The microchannel was developed to ensure one-dimensional flow with minimal entrance effects. A peristaltic pump was utilized to drive the Newtonian fluid into the rectangular microchannel using the Tygon tubing (with inner and outer diameters of 1.2 mm and 2.4 mm, respectively) at a constant pressure. The microchannel remained empty in the absence of fluid, and an open circuit existed between two adjacent electrodes. As fluid flows through the microchannel, a conductive path was established between two electrodes. This results in positive potential appearing at the input of the analog input port

of Arduino Nano. As the fluid touched the first electrode pair, the higher potential was sensed at the A0 port, and the timestamp was registered by the Arduino Nano and taken as t_0 . As the fluid progressed further, the higher potentials were sensed at A0, A1, A2, A3, and accordingly the timestamps were registered as t_0 , t_1 , t_2 , and t_3 , respectively. From these timestamps, the time difference between t_0 and t_1 was obtained and noted as Δt_1 . Similarly, the time difference between t_1 and t_2 , t_2 and t_3 were also obtained and noted as Δt_2 , Δt_3 , respectively. As shown in Equation (3), the average of these three-time differences Δt_1 , Δt_2 , and Δt_3 were measured and used as the average time Δt for the viscosity calculation.

On the LIG-EMV, four equidistance electrodes were printed with the three-time gap measurement. As a proof of principle, various conductive Newtonian fluids were chosen for creating the electrical contact between the four LIG fabricated electrodes. The Arduino Nano was programmed to sense the time instant of change in voltage and note the timing stamp accordingly. Water was used as a reference fluid to measure the relative viscosity, and the time required by water to cover a fixed length in the microchannel was estimated from five trials and stored in the Arduino. Then, the Newtonian test fluids were subjected to the microchannel for similar time measurements, and then viscosity was calculated using Equation (2) with water as the reference fluid.

The LIG-EMV with inset connection to Arduino and battery is depicted in Figure 2. 3. Here, on one side, all four electrodes are connected to the positive terminal of a battery using a common wire. On the other side, four electrodes were connected to the four separate analog input terminals of the Arduino Nano board. The electronic circuit across any pair of the electrode could complete only in the presence of the Newtonian fluid. Based on this, a voltage response was displayed on the Arduino serial display. This was programmed to calculate the three-time differences based on obtained voltage impulse at four electrodes.

The developed device was subjected to the viscosity measurement of various Newtonian fluids, like skimmed milk, toned milk, acetic acid and water sample, and then compared with an Ostwald viscometer. After considering the viscosity of water as a reference, the viscosity values of the test fluids were determined by the proposed method using Equation (2). The viscosity values of these four samples were measured and compared with the change of three parameters including flow rate and different RPM values.

2.6. Result and Discussion

The motivation behind this investigation was to develop an automated system for high-throughput dynamic viscosity measurement using fabricated LIG-EMV devices with integrated electrodes, peristaltic pumps, and Arduino Nano as shown in Figure 2. 5. Microchannel was fabricated using the CO₂ laser engraving technique with optimization of speed and power by embedding four electrodes on

it. The viscosity values of various Newtonian fluids were obtained from the fabricated LIG-EMV device.

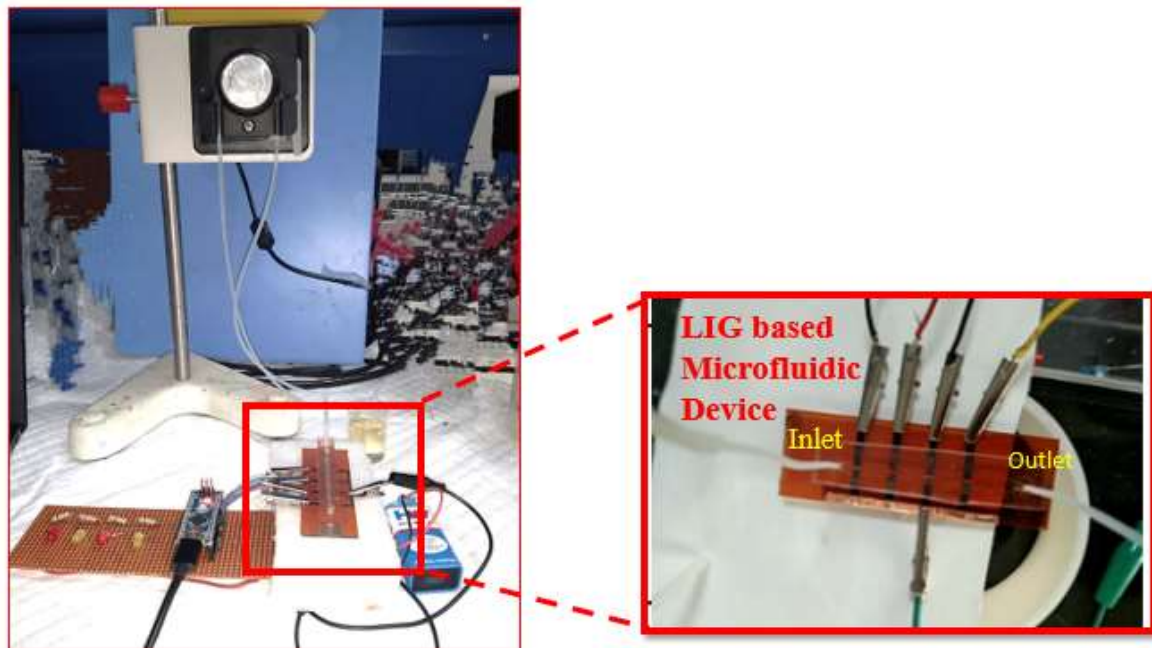


Figure 2. 4 Complete assembly of the experimental setup.

Ostwald benchtop viscometer was used to cross verify the error percentage of the results obtained from the LIG-EMV device. This was carried out while assuming that other parameters, like shear rate, shear stress, and temperature, were maintained constant throughout the experiments.

2.6.1. Influence of Flow Rate on Reynold Number

In the rheological property measurement technique, the optimization of flow rate is a relevant parameter as the variation of flow rate directly affects the Reynold number of the fluid leading to the creation of turbulence in the microchannel. The laminar flow, depending on the fluid velocity or flow rate, is a mandatory condition for operating the microfluidic viscometer. Theoretically, the Reynolds number was determined for the reference fluid to ensure the laminar flow based on the flow rate in the fabricated LIG-based microfluidic device. Hence, the flow rate was varied from 70 $\mu\text{l}/\text{min}$ to 210 $\mu\text{l}/\text{min}$ to explore the optimum flow rate to obtain a constant pressure gradient and check the existence of laminar flow throughout the microchannel. Since the laminar flow from the beginning of the microchannel was sufficient to start the measurement of the time difference, this was also considered during the assembly process.

The Reynolds number can be calculated by,

$$\text{Re} = \frac{\rho v_a D_H}{\mu} \quad (4)$$

where ρ is the density of the fluid, v_a is the average velocity of the sample fluid, D_H is the hydraulic diameter of the microchannel, μ is the dynamic viscosity of the sample fluid [31]. In this case, D_H was measured to be 0.0684 mm which was calculated using the relation

$$D_H = \frac{2HW}{H+W} = \frac{2H}{1+\frac{H}{W}} \quad (5)$$

Fluid distribution was measured at different pump flow rates leads to the maximum velocity (v_m) which measures the average velocity of the fluid.

$$v = \frac{v_m}{v_a}$$

Table 2. 1 Calculation of Reynold number for sample fluids and flow rate

Sample/Flow Rate	70 $\mu\text{l}/\text{min}$ water equivalent to (1 RPM)	170 $\mu\text{l}/\text{min}$ water equivalent to (3RPM)	210 $\mu\text{l}/\text{min}$ water equivalent to (5 RPM)
Water	5.92	14.38	17.77
Acetic Acid	4.1	9.98	12.32
Toned Milk	5.34	12.98	16.03
Skimmed Milk	4.05	9.83	12.15

$$v = -0.5 \left(\frac{H}{w}\right)^2 + 1.15 \left(\frac{H}{w}\right) + 1.5 \quad (6)$$

v is the ratio of maximum velocity v_m to average velocity v_a as a function of the aspect ratio $\frac{H}{w}$ for incompressible fluids. As the aspect ratio $\frac{H}{w}$ decreases to 0.023, Equation (6) shows that v of 1.526 ~ 1.5 corresponds to 2D full laminar flow with velocity distribution in parabolic nature which proves Poiseuille flow. To calculate the Reynold number, viscosity values were measured from the Ostwald viscometer as the proposed device worked on the same principle to measure the viscosity, and capillary-based measurements were done for kinematic viscosity measurement which was then converted to the dynamic viscosity.

Table 2. 2 Average time (in a sec) taken by sample fluids for different flow rate in the microchannel

Sample	At pump speed 70 μl/min	At pump speed 170 μl/min	At pump speed 210 μl/min
Water	5.49	3.06	1.59
Acetic Acid	6.62	4.47	1.75
Toned Milk	5.88	3.53	1.61
Skimmed Milk	6.15	4.28	1.69

Table 2. 3 Viscosity computation for the different viscosity sample.

Sample	Time (Sec)	Viscosity by Benchtop Viscometer (cP) (μ1)	Viscosity Using LIG- EMV (μ2)	Error (%) = (μ2-μ1)×100/μ1
Water	3.06	0.89	0.89	Reference
Acetic Acid	4.47	1.35	1.30	-3.69
Toned Milk	3.53	1.015	1.026	1.08
Skimmed Milk	4.28	1.35	1.24	-8.14

For the development of proper laminar flow with $Re \ll 2300$, the minimum entrance length of the microchannel L_e was given by the[32].

$$\frac{L_e}{H} = [-0.129 \left(\frac{H}{W}\right)^2 + 0.157 \left(\frac{H}{W}\right) + 0.016 \left(\frac{H}{W}\right)] Re \quad (7)$$

By simplifying in terms of D_H maximum entrance length was modified as

$$L_e = (D_H(0.6/(1 + 0.035Re) + 0.056Re))L \quad (8)$$

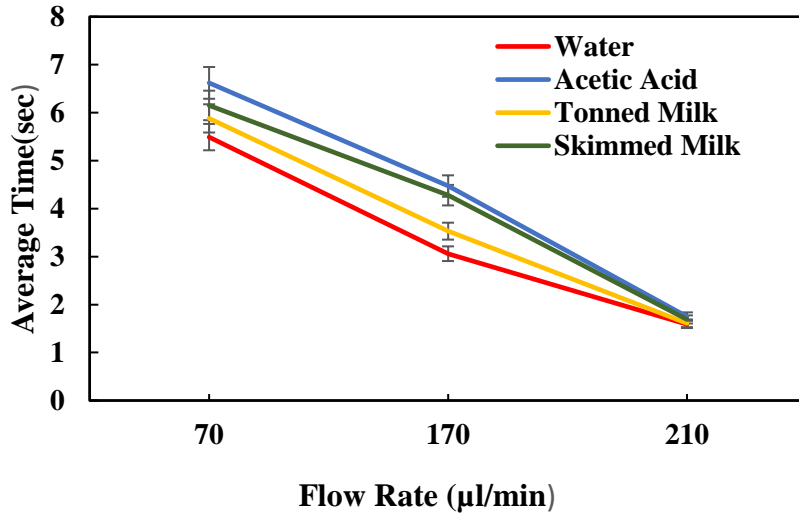


Figure 2. 5 Average time measured for different fluids at a different flow rate

Here, L_e is a function of Re and $\left(\frac{H}{w}\right)$ for rectangular microchannel according to Equation (8). In this work, the maximum entrance length (corresponding to the highest flow rate attained in the device ~ 210 $\mu\text{l}/\text{min}$ for water) was measured to be $L_e = 0.059L$, justifying that smaller requirement (less than 6%) of microchannel length (26 mm) proves the laminar flow has been fully developed in the microchannel. Thus, it was concluded from Table 2. 4 that in the microchannel, the laminar flow was sufficiently developed as the Reynolds numbers remain less than 2300 for different fluids. Table 2. 5 summarizes the average time conforming to three different velocities spanning all five trials, while Figure 2. 7 shows the evaluation of the average time intervals for five samples related to three velocities. These experiments manifest the efficient working of the electronic subsystem and efficient response of the viscometer (~ 1.6 sec).

2.7. Errors in Measurement of Fluids Viscosity at Different Flow Rate:

The errors and operating limits of LIG-EMV about viscosity and flow rate that can be predicted with the present analysis are discussed in this section. Table 2. 6 summarizes the average time for reference fluid calculated using automation of Arduino Nano board with flow rates 210 $\mu\text{l}/\text{min}$, 170 $\mu\text{l}/\text{min}$, 70 $\mu\text{l}/\text{min}$ which was further used for viscosity calculation. The average time values at various flows were linearly fitted to generate a calibration curve relating the viscosity values to the Hagen Poiseuille was depicted in Figure 2.7. Also, fitted equations and parameters are displayed inset. Here, x indicates flow rate, y indicates average time and R was the regression coefficient. During viscosity measurement, water viscosity, measured using a benchtop viscometer, was taken as a reference. To obtain the viscosity of acetic acid, the average time for a moderate flow rate of 170 $\mu\text{l}/\text{min}$ was taken from Table 2. 7. This time was 4.47 sec for acetic acid and 3.06 sec for water.

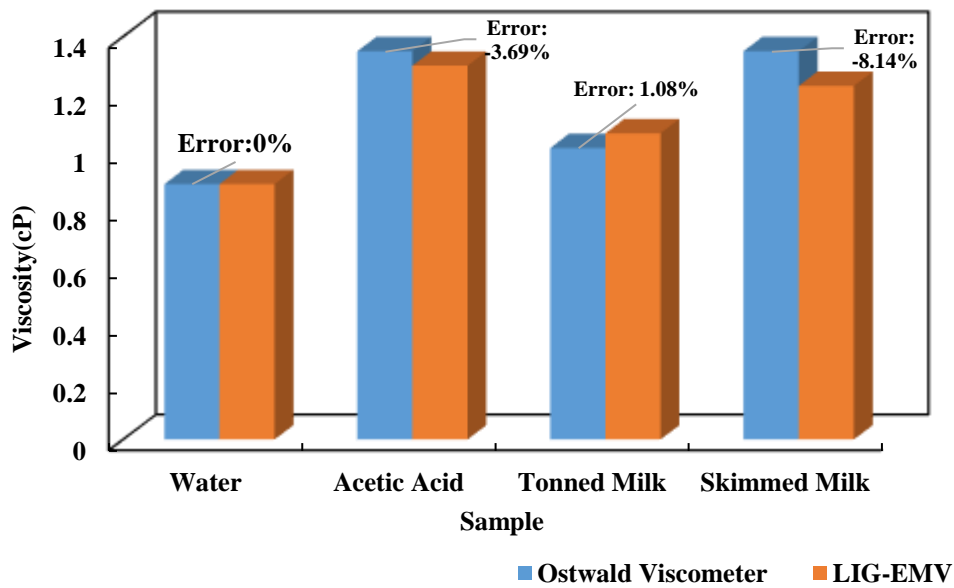


Figure 2.6 Measurement of Error percentage in LIG –EMV and Ostwald viscometer

Water viscosity was obtained as 0.89 cP using benchtop viscometer and was used as a reference to calculate the viscosity of sample (acetic acid) using Equation (2) and found to be 1.30 cP. This viscosity was noted as viscosity obtained from the EMV device. The acetic acid viscosity was also measured directly using the benchtop viscometer and found to be 1.35 cP. So, the error between viscosity obtained using our EMV device and benchtop viscometer was found to be 3.69%. A similar approach was followed for toned milk and skimmed milk, and was noted in Table 2. 8. From the last column, it was found that the errors were in the range of $\pm 1.08\%$ to $\pm 8.14\%$. These validation results demonstrate that the proposed device can be used for the viscosity measurement of the Newtonian fluids. In this study, the measured error in the viscosity was typical $\sim 3\%$ for the water-like fluids at a different flow rate. When higher viscous fluids were used, the error was larger nearly 8% at different flow rates because a shorter distance will be covered by the fluid. LIG –EMV showed a measurement performance with an error to Ostwald viscometer which was plotted graphically in Figure 2.7.

The microchannel expands to a larger dimension when high pressure is applied to one end and the governing flow–pressure relation for the microchannel was the Hagen–Poiseuille rule, but with a larger channel width[32]. These errors would be reduced by optimizing the surface area occupied by the fluid in the microchannel by optimizing the width of the microchannel.

2.8. Pressure Gradient Vs Viscosity of Fluids

Microchannel with minimum height has a major concern of pressure drop throughout the channel length. At the highest flow rate, the pressure drop values are higher for microchannels due to lower hydraulic diameters[33]. The primary detecting method for the fluid viscosity of LIG-EMV is the time interval to cross two neighboring electrodes which depend on the fluid flow rate. Higher viscous fluids

have lower flow rates inside the microfluidic channel than less viscous fluid like water, whereby it needs a larger pressure gradient along the length ($\Delta P/L$) to drag the fluid in the microchannel. comprising of static and dynamic pressure given by[34],

$$P_{\text{total}} = P_{\text{static}} + P_{\text{dynamic}} \quad (9)$$

where, $P_{\text{static}} = \rho g H$ and $P_{\text{dynamic}} = \frac{\rho Q^2}{2A^2}$

where ρ represents the density of the fluid, g is the acceleration of gravity, H is the height of the microchannel, A is the cross-sectional area of the microchannel, and Q is the flow rate. As static pressure increases with microchannel depth, each microfluidic device will have a varying tendency to perform with viscosity and pressure ranges. As a result, an appropriate microchannel depth was needed to provide a standardized pressure range. Herein, the static pressure (P_{static}) has only a marginal effect on the overall pressure due to the minuscule depth ($35 \mu\text{m}$). On the other hand, the dynamic pressure (P_{dynamic}) is proportional to the square of the flow rate (Q). As a result, the dynamic pressure is a more important factor affecting viscosity for maintaining a constant flow rate. The operating mechanism of the LIG-EMV relies on the monitoring of flow rate variations due to alteration in the fluid viscosity. Particularly, Equation (1) shows that the fluid viscosity (μ) is inversely proportional to the fluid flow rate (Q) or fluid velocity (v_a) in the microchannel. Figure 2. 8 depicts how viscosity varied with the pressure gradient in which a flow rate of $170 \mu\text{l/min}$ was chosen for further pressure gradient and time analysis using a pressure sensor. At $170 \mu\text{l/min}$, constant pressure of 0.02 Nm^{-3} was maintained throughout the microchannel for water (reference) because Newtonian fluids are unaffected by the variation of the parameter like shear rate, shear stress, temperature[30].

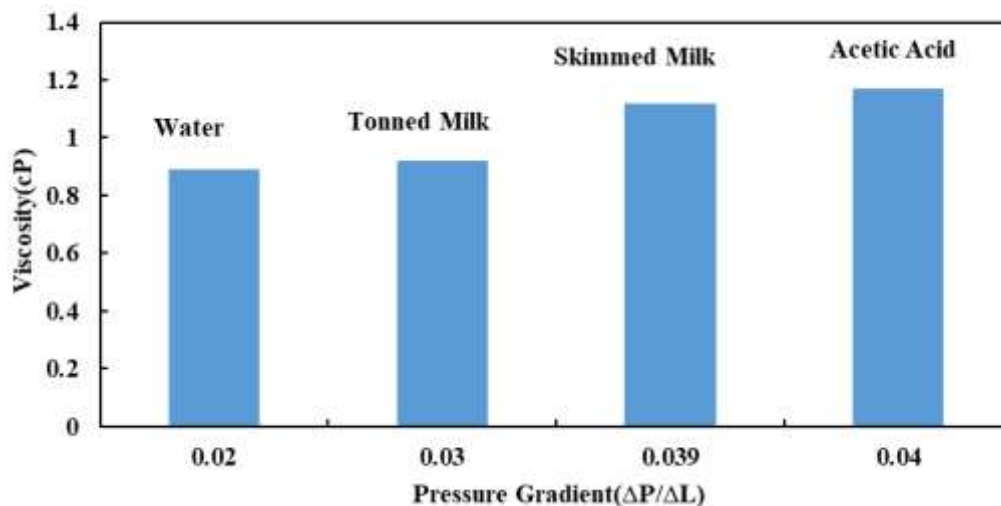


Figure 2. 7 Viscosity (cP) Vs Pressure Gradient ($\Delta P/L$) for different fluids

Here, the measured pressure gradient and viscosity are linearly related. It was also detected that for the estimation of viscosity, the pressure gradient was constant throughout the microchannel for 2 min which

was in the range of only 0.015-0.04 Nm^{-3} at a moderate flow rate as shown in Figure 2.8. Higher viscous fluids, such as acetic acid and skimmed milk demonstrate a significantly higher pressure gradient (nearly 0.04 Nm^{-3}) which was needed to observe smooth flow throughout the microchannel. As Newtonian fluids are unaffected by the variation of parameters, a constant pressure gradient was maintained throughout the microchannel for a given reference fluid. Also, the pressure gradient at the flow front in the microchannel was constant due to its lower flow resistance. However, the short inlet microchannel of diameter 1.2 mm was used to generate a higher flow rate due to its lower flow resistance and faster response of the fabricated viscometer[35]. Pressure reduces along the microchannel as the hydraulic diameter decreases, allowing the highly viscous fluids to drag. This proves that lesser fluid resistance was present throughout the microchannel which manifests that the LIG-EMV device mimics the fundamental nature of the Ostwald viscometer.

2.9. Conclusion:

In this work, a simple approach is developed to estimate viscosity using a flexible electro-microfluidic device by harnessing its hydrophilic property. An electro-microfluidic viscometer (EMV), with laser-induced graphene (LIG) electrodes on polyamide substrate, was fabricated and a microcontroller was programmed to measure the viscosity in an automated manner with a minimal response time of 1.6 sec. The LIG-EMV, costing just US \$0.23, was demonstrated to quantify the viscosities of three different Newtonian fluids like toned milk, skimmed milk, acetic acid with less sample volume requirement of 1.5 μL . The error in the proposed device was estimated to be $\pm 1.08\%$ by comparing the viscosity values obtained from the proposed device with the benchtop Ostwald viscometer. The automated design version of LIG-EMV opens up new possibilities for its application in other fields, such as taste sensing. The unique properties of LIG, such as its high surface area and electrical conductivity, make it suitable for detecting and analyzing taste-related molecules, which can have significant implications in fields such as food and beverage industry, healthcare, and environmental monitoring which is discussed in the next chapter. The automated design of LIG-EMV can potentially enable efficient and precise taste sensing applications, providing valuable insights and data for various purposes. In summary, the LIG-EMV offers several advantages over conventional devices, including simplified fabrication, ease of use, and potential for diverse applications beyond its original design. These benefits make LIG-EMV a promising technology with the potential for widespread adoption in various industries and applications.

CHAPTER 3:

LASER ABLATED MICROFLUIDIC DEVICES INTERDIGITAL ELECTRODES FOR TASTE SENSING APPLICATION IN FOOD INDUSTRY

Chapter describes fabrication and testing of a microfluidic taste sensor which senses various tastes by measuring the impedance between LIG interdigitated electrodes without modifying the surface of electrodes for taste monitoring in the food industry. Also, the potential of LIG microfluidic technology has been depicted to be integrated into multi-functional point-of-care sensors for human sensory tastes, clinical, and environmental applications. On-site taste monitoring is essential for human health and in food industry and widespread adoption requires less expensive, easy to fabricate technology and very precise portable equipment. The portability and high sensitivity of the device are regulated by the electrode configuration and, in turn, the fabrication techniques employed. In this context, herein, sensitive and specific electrical detection of five human gustative sensory tastes leveraging unique properties of graphene to realize optimized electrodes is presented.

The integration of LIG electrodes in a microfluidic environment is presented by fabricating electrodes inside a microchannel whose dimensions are well documented and that can be easily transferred among labs. Importantly, the hydrophilic property of the electrodes and substrate flexibility allows for easy removal and reuse of the electrode, which becomes a significant advancement for electrochemical detection in microfluidic devices. The LIG technique was used to fabricate a microfluidic device that features integrated microchannel and interdigitated electrodes (IDEs), utilizing a capacitive sensing mechanism. Electrochemical Impedance Spectroscopy (EIS) considered the working of the LIG-IDE microfluidic device. In microfluidic conditions, the impedance change exhibited a linear relationship with the concentration of various chemicals within the range of 1 ppm to 1000 ppm. The minimum detection limit achieved was 1 ppm.

The microfluidic taste sensor can classify the five basic taste types: sweet, salty, sour, bitter, and umami. This functioning of the device is also independent of temperature and humidity. This could aid in the development of a system for identifying and monitoring the concentration of a specific type of taste. As a proof of concept, the microfluidic LIG-IDE sensor is tested in basic tastes relevant to human gustative perception (sweetness, saltiness, sourness, bitterness, and umami) at different concentrations. The human threshold for sweetness and saltiness is typically at 10 mM, and the device can distinguish sensing effects at low concentrations. The applications of the devices fabricated using engraving technology and interdigitated electrodes are also discussed in this chapter.

3.1. Design Principle and Materials and equipment:

The LIG-IDE microfluidic device, working on the principle of capacitive sensing, was developed on a polyimide sheet. The surface charge on the electrode fingers changes with the resulting electric

displacement field due to the capacitive nature of the LIG-IDE device. The operating principle of the LIG-IDE device is depicted schematically as a parallel-plate capacitor in Figure 3.1(a) resultant electric field is produced between the two oppositely charged electrodes when a frequency-dependent voltage signal is applied to the excitation electrode. Owing to the coplanar characteristic of the electrodes, electric field ripples from one finger to the next as shown in Figure 3.1 (b). The field might pass through any material close to the sensing region causes switching the properties of the field [36]. These modified properties were analyzed to study the generated electric fields. The existence of the input material above the sensing region was measured by opting for a one-directional measurement state via the polyimide sheet as an insulating substrate on the other hand. An impedance analyzer was used to monitor the responses of LIG-IDE sensor prototypes designed and deployed for various applications. The developed prototypes were used in a variety of applications, especially for taste senses.

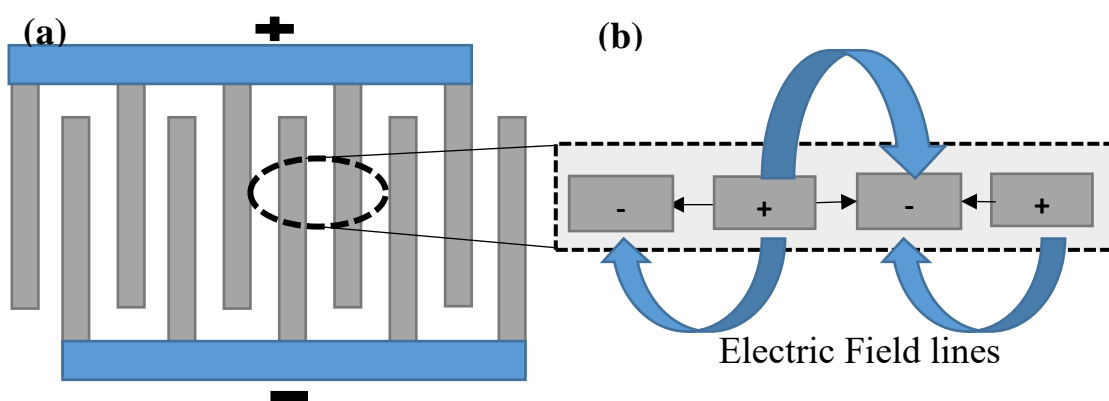


Figure 3.1. Schematic of the operating principle of the LIG-IDE Sensor: (a) Operating Principle of the parallel-plate capacitor (b) Rippling Direction of Resultant Electric Field lines that occur within electrode gap.

A polyimide (PI) sheet which has a thickness of $25.4\ \mu\text{m}$ was purchased from Dali Electronics, India, and a 30 W CO_2 Laser Engraver (VLS 3.60 from Universal Laser Systems, USA) was utilized to develop the LIG-IDE region within the channel. The four-probe analysis (Ossila, United Kingdom) was performed to determine the conductivity along with sheet resistance of the fabricated LIG-based electrodes technique. An electrochemical workstation (SP-150 from Biologic, France), in the two-electrode configuration, was used. Furthermore, the channel height of the fabricated microfluidic device was found to be $35\ \mu\text{m}$ and measured by using a contact profilometer (SJ-210 from Minutolo, Japan). PDMS, Sylgard® 184 silicone elastomer was purchased from Sigma Aldrich. $\text{C}_{11}\text{H}_{12}\text{N}_2\text{O}_2$ (L-Tryptophan), $\text{C}_{12}\text{H}_{22}\text{O}_{11}$ (sucrose), $\text{C}_{10}\text{H}_{14}\text{N}_5\text{O}_8\text{P}$ (guanosine-5-monophosphate disodium salt) (GMP), NaCl (sodium chloride), and $\text{C}_6\text{H}_8\text{O}_7$ (citric acid anhydrous) were purchased from Sisco Research Lab. Apple, lemon, coffee, and tomato juice were purchased from a neighbourhood fruit seller.

3.2. Microfluidic LIG-IDE Sensor Design and Fabrication

Previously work has been done to design and optimize the dimension of the microchannel and IDE [37]. The optimized design parameter of interdigitated electrodes was modeled and reported thoroughly[38]. The work reported by the author represents the capacitive sensor model when IDE is immersed in a solution. demonstrates the microfluidic device with a microchannel along with Interdigitated electrodes (IDE) engraved in it. The inset schematic Figure 3. 2 shows the dimensions of interdigitated electrodes with spacing between two fingers as 0.4 mm and width of the finger as 0.8 mm. The length of the finger was selected according to the requirements of the microchannel. For the fabricated device, the microchannel height was around 0.035 mm.

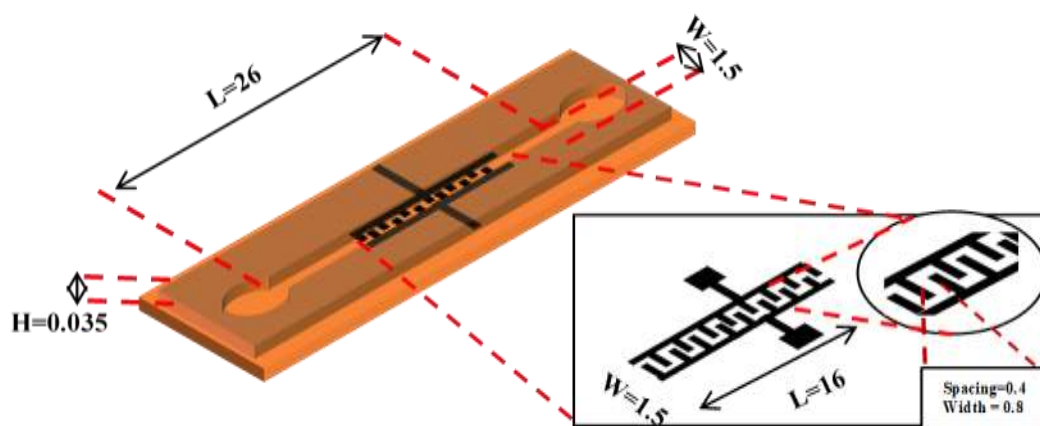


Figure 3. 2: Design of microchannel and Interdigitated electrodes along with dimensions in mm

The LIG-based interdigitated electrode sensor (LIG-IDE) was fabricated using a CO₂ laser engraving technique. First, the fundamental design of the Interdigitated electrode was developed using a software (Corel Draw) and saved in a .dxf format, which was loaded to the CO₂ laser. Figure 3.3 illustrates the fabrication steps of the LIG-IDE sensor. The optimum laser characteristics, such as 6.5% (1.95 W) power and 4.5% (2.5 cm/s) speed, were selected based on prior results. [29]. Electrical conductivity of 378 S/m was obtained by a four-probe measurement technique. Before the laser exposure, to ensure adequate strength, the polyimide sheet was ultrasonically cleaned in a 100% isopropyl alcohol (IPA) solution and dried at 50°C before being bonded to the microscopic glass, as shown in Figure 3.3 (a). Furthermore, the polyimide was kept inside the CO₂ engraver for the development of the interdigitated electrodes (IDEs). With controlled speed and power, a microchannel was developed as illustrated in Figure 3.3 (b). Graphene layers were developed at the region wherein capacitance sensing was required. The microfluidic device was covered by adhering acrylic sheet utilizing thin double-sided adhesive tape. After bonding with the acrylic sheet and double-sided thin adhesive tape, the microchannel remained leakage-free [9]. The fixing of the acrylic sheet with LIG-IDE was accomplished as illustrated

in Figure 3.3 (c) and (d). The final image of the LIG-IDE device is presented in Figure 3.3 (e). Pipette tips were employed to provide a leak-free interface between the microchannel and the tubing. Before beginning the experiment, the peristaltic pump was used to deliver standard distilled water into the rectangular microchannel.

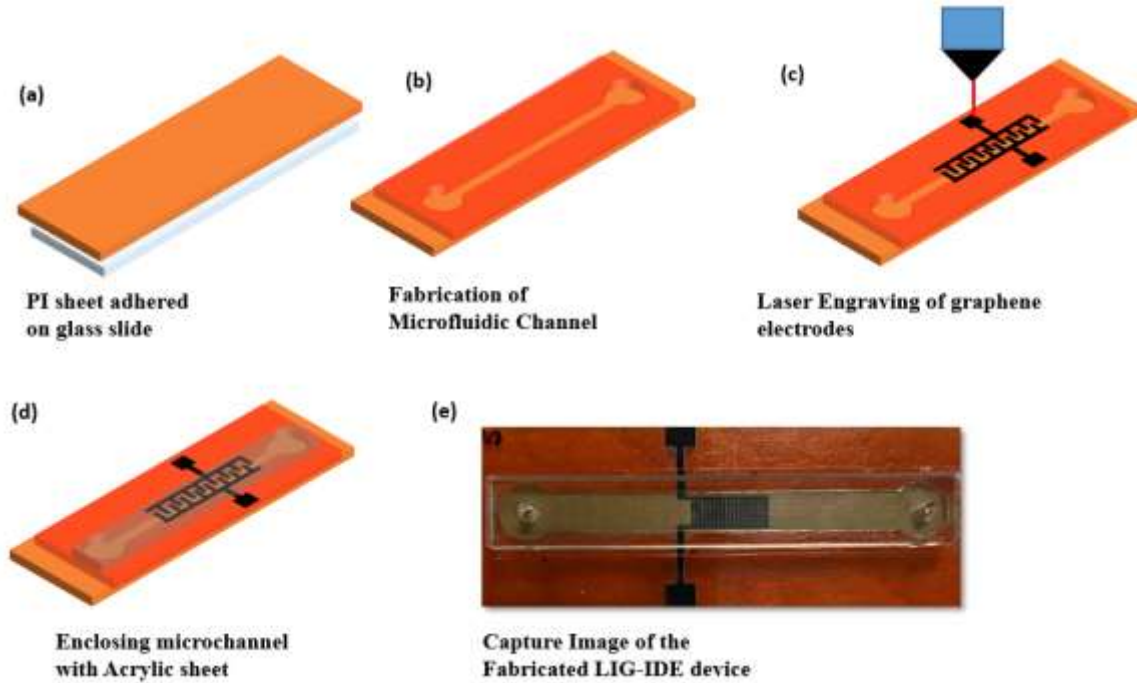


Figure 3. 3 Schematics of Fabrication steps of LIG-IDE sensor (a) PI sheet of 25.4 microns adhered on glass slide (b) Fabrication of Microfluidic Channel (c) Laser engraving of graphene electrodes (d) Enclosing Microchannel with the acrylic sheet (e) Capture Image of the Fabricated LIG-IDE device.

Table 3. 1: Dimensions of the Microfluidic LIG-IDE fabricated using CO₂ Laser Engraver

Parameter	Dimension of Microfluidic LIG-IDE
Height of microchannel	0.035 mm
Length of microfluidic microchannel	26 mm
Width of microchannel	1.5 mm
Interdigitated electrode finger Spacing	0.4 mm
Interdigitated electrode width	0.8 mm

The dimensions of the microfluidic LIG-IDE device are shown in Table 3. 2, where the volume of 2 μ L can be accommodated in the microchannel. Because the microchannel was manufactured on an unmodified surface with a rectangular shape, the non-interrupting flow was discovered between the

microfluidic devices, as shown in the SEM images in Figure 3.4 (a) and (b). A metallization ratio of 0.66 was used to ensure maximum measurement sensitivity from IDEs [39]. There were twenty pairs of interdigitated electrodes with a thickness of 0.035 mm for each finger and a gap of 0.4 mm between two consecutive fingers. The length and width of the sensing area of the patch were 16 mm and 1.5 mm respectively.

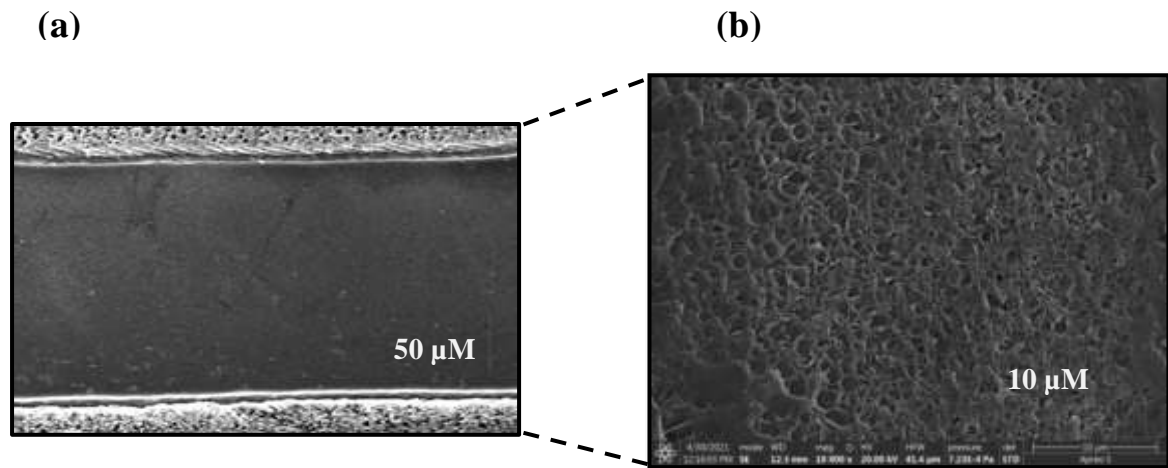


Figure 3. 4 SEM images of the fabricated rectangular horizontal microchannel to represent untreated surface on Polyimide sheet. (a) Upper view of the microchannel. (b) Magnified view of laser engraved microchannel.

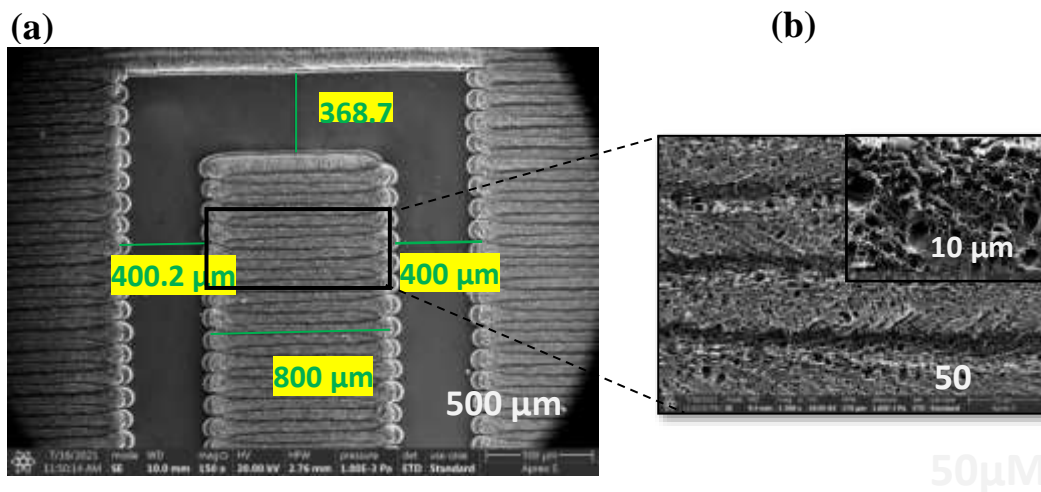


Figure 3. 5 Scanning electron microscopic images of the fabricated LIG-IDE sensor to characterize graphene on a polyimide sheet. (a) The upper view of electrode fingers with the dimensions is in μm. (b) Top view of laser-induced graphene.

Two major advantages of this LIG-IDE sensor were their improved mechanical properties due to the honeycomb structure of graphene along with the corrosion resistive nature of the electrodes because of

lower effective surface area as depicted in Figure 3. 5 (a). Also, as can be seen from Figure 3. 5 (b), the laser carbonizes the non-conductive polymer surface, producing porous super hydrophilic conductive graphene patterns that are used for sensing various analytes [16] [40] [41]. The sensing region of the LIG-IDE sensor was found approximately 24.0 mm² and the conductivity (378 S/m) of LIG-electrodes was reasonably improved.

3.3. Experimental Setup:

The complete setup for the actual experiment is shown in Figure 3. 6 To validate the sensing capability of the device, experiments were performed with different chemicals at room temperature. To prevent direct contact with the connection pad, IDE was completely concealed with analytes.

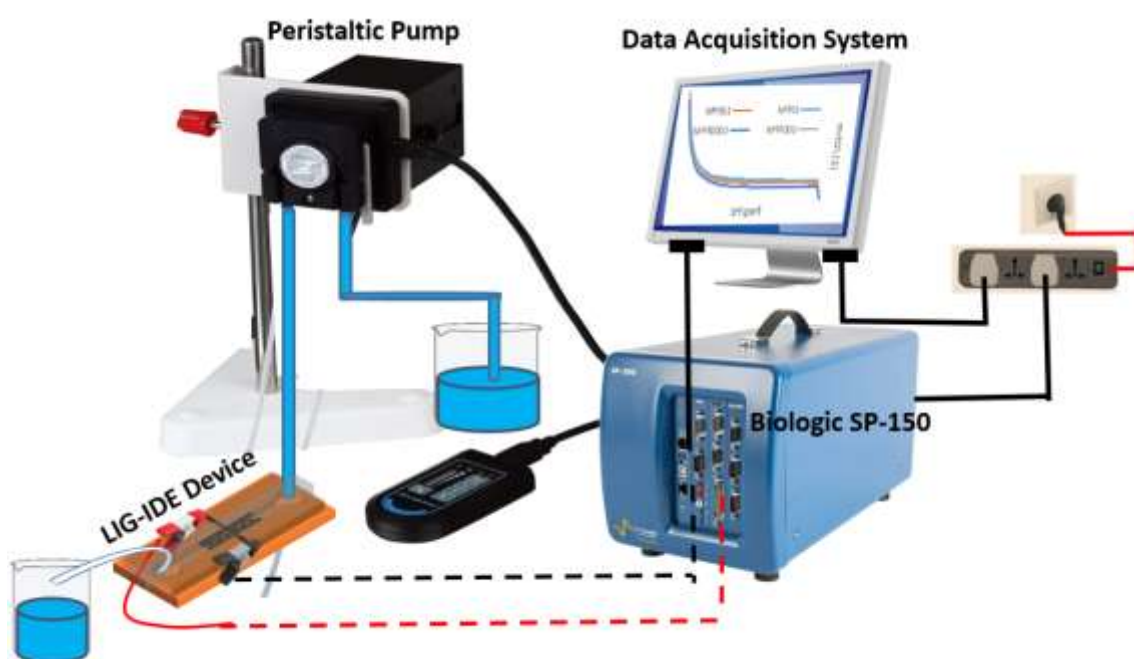


Figure 3. 6 Complete Assembly of Experimental Setup

The sinusoidal signal of $\pm 5V$ was applied and frequencies were swept from 10 Hz to 100 kHz and frequency responses were captured. To perform electrochemical impedance spectroscopy (EIS), an electrochemical workstation was used in the two-electrode configuration, was used. Alligator clips were connected to both sides of LIG-IDE to analyze the variations sensed by the sensor. To test the repeatability response of the device, sample readings were taken an average of three times at a flow rate of 170 $\mu\text{l}/\text{min}$. It was observed that fluid sensitivity improved significantly by decreasing the flow rate from 310 $\mu\text{l}/\text{min}$ to 170 $\mu\text{l}/\text{min}$, which was likely due to diffusion effects at lower flow rates or Peclet numbers [42]. At flow rates lower than the design flow rate, flow separation can occur in the microchannel, which affects the sensitivity of the device [43]. Therefore, all measurements presented in this case are performed at 170 $\mu\text{L}/\text{min}$ flow rate. The microchannels were sequentially filled at 170 $\mu\text{L}/\text{min}$ with various ppm solutions of different chemicals, namely Sucrose, Citric acid, Guanosine

monophosphate (GMP), Sodium Chloride, and L-Tryptophan, which were employed as the solute to create sweet, sour, umami, salty, and bitter tastes respectively. Experiments using four distinct concentrations of 1,10,100, and 1000 ppm were developed using the serial dilution technique. The solution was serially diluted by mixing the de-ionized water as a solvent. Initially, 1000 ppm stock solution was prepared by adding 1 gm solute into 100 mL deionized water, the second solution of 100 ppm was prepared by pipetting 10 mL of stock solution to the 90 ml of deionized water. This process was monitored to achieve up to 1 ppm concentration. Sensory research requires a standardized approach for determining tastant-detection thresholds. As a result, the standard human taste threshold levels have been reported. The tastants were studied about the analyte concentration concerning the literature[44]–[46]. As for different analytes at least 1 ppm concentration was evaluated which was converted into micromolar, the lowest limit obtained for sodium chloride was 17.11 μM , 2.92 μM for sucrose, 5.205 μM for citric acid, 4.89 μM for L-Tryptophan, and 2.45 μM for GMP. These values lie in the human taste sensory threshold range.

3.4. Result and Discussion:

Electrochemical Impedance Spectroscopy (EIS) is commonly mechanisms used for electrochemical-based sensing investigations because of its non-invasive nature. EIS is commonly used to characterize the electrical double layer at electrode-electrolyte interfaces and investigate changes in impedance associated with sensing mechanisms. First, the impedance spectra of normal DI water with LIG-IDE were measured to analyze the impedance signal change prior and after analyte addition in DI water. An electric behavior of the sensing area with LIG-IDE and the responses of the LIG-IDE towards different chemicals expressed in terms of resistance and reactance for the sensitive frequency range. All solutions were applied to an EIS analysis.

Two graphs are shown for each simulated taste chemical: a) resistance (real Z) versus frequency and b) reactance (Z) versus frequency. Concentrations below 1 ppm could not be evaluated because the fabricated LIG-IDE-based sensor was unable to detect and discriminate at such low concentrations. Figure 3. 7 presents the results of citric acid, which shows resistivity decreases with increasing the concentration of citric acid. By varying the concentration of citric acid, electrochemical impedance was altered because of the presence of different Hydroxyl ions (OH^-) in its structure[47]. Ion solvent interaction at a higher frequency causes the impedance change in the solution. The real part of the impedance (reactance) shows distinct variations within the concentration level that describe the dielectric properties of a solution. The custom-designed sensor was successfully utilized to accurately distinguish varying levels of analyte concentration, while operating optimally within the frequency range of approximately 0.1 Hz to 60 kHz, ensuring efficient sensing performance.

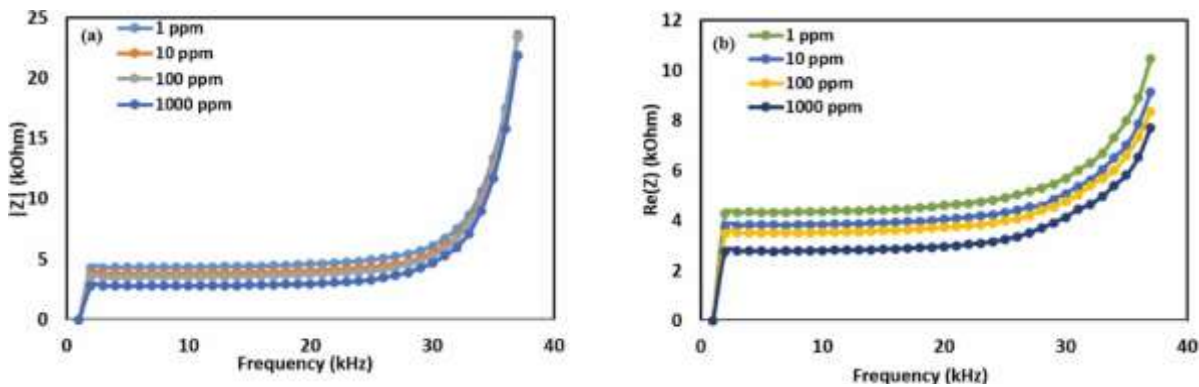


Figure 3. 7 EIS responses of the LIG-IDE sensor towards citric acid expressed in terms of (a) reactance and (b) resistance for the frequency range.

As depicted in Figure 3.8 , the real part of the impedance (reactance) showed distinct variations with variation in the ppm level, which is ascribed to the dielectric properties of the sucrose because of the presence of different Hydroxyl ions (OH^-) in its structure. These variations are more evident in a frequency range of 0.1 Hz – 60 kHz. On the other hand, changes in the real part occurred within a small frequency range.

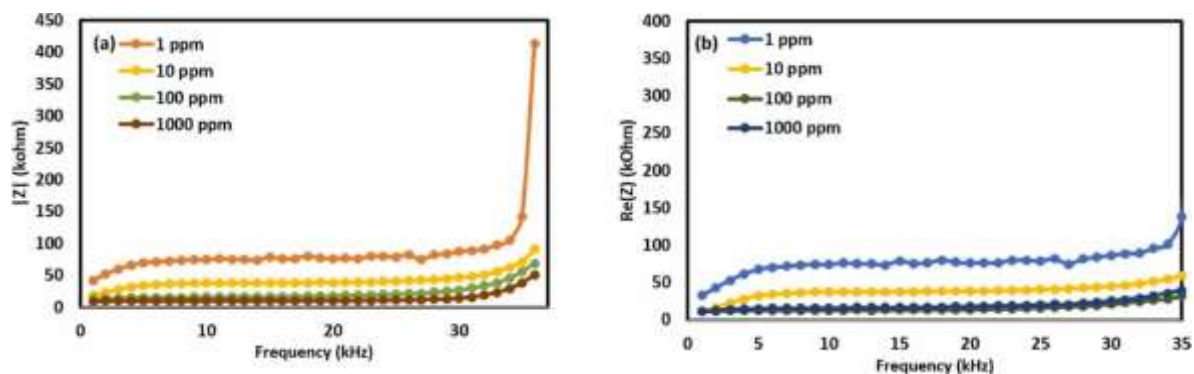


Figure 3. 8 EIS responses of the LIG-IDE sensor towards sucrose expressed in terms of (a) reactance and (b) resistance for the frequency range.

The reactance value of citric acid and sucrose shows similar behaviour for frequency as shown in Figure 3. 7 and Figure 3. 8, respectively. As the frequency rises, the reactance values increase until they reach saturation due to the double-layer capacitance being shorted, causing a gradual plateau. As ion-ion and ion-solvent interactions determine how an ion behaves in a solvent as sulfamate function is essential for cyclamate sweetness although the cation seems to have some effect on the sweet taste. For interpretation of the taste of sweet substance, comprehension of sulfamate function which is essential for cyclamate sweetness was utilized [48]. As shown in Figure 3. 8, for sucrose, after a frequency range of 30 kHz, the reactance value decreases, indicating the influence of electrolyte ion association on the reactance behavior. Due to the lower density of solvated ions (i.e., cations/anions) at the electrode interfaces, the device demonstrates increased sensitivity towards lower analyte concentrations.

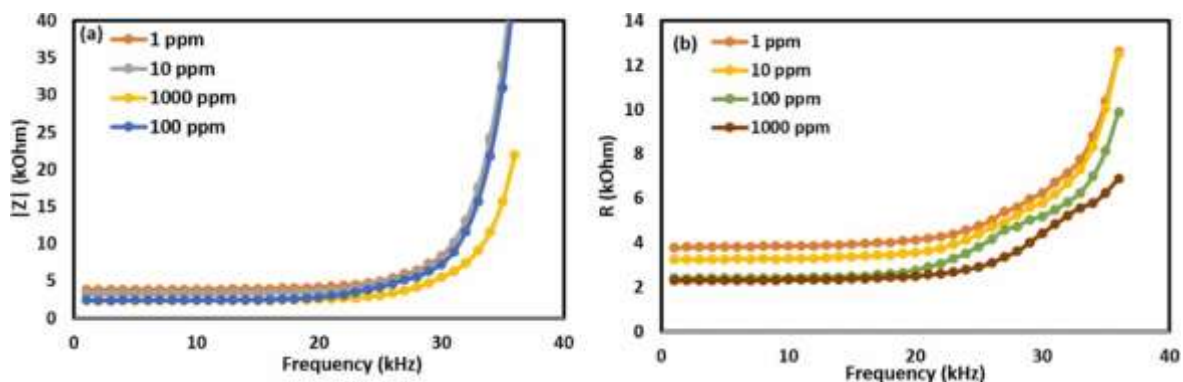


Figure 3. 9. EIS responses of the LIG-IDE sensor towards NaCl expressed in terms of (a) reactance and (b) resistance for the frequency range

As shown in Figure 3. 9, the decreasing rate of the impedance around the concentration range of NaCl from 1 to 1000 ppm seems to be the transition point where the sensor impedance is lower than the solution resistance. However, particularly in lower frequency, the sensor impedance is highly dominated by the concentration-dependent double-layer capacitance. Therefore, until its impedance becomes lower than the resistance of the electrolyte, the sensor impedance becomes relatively independent of frequency.

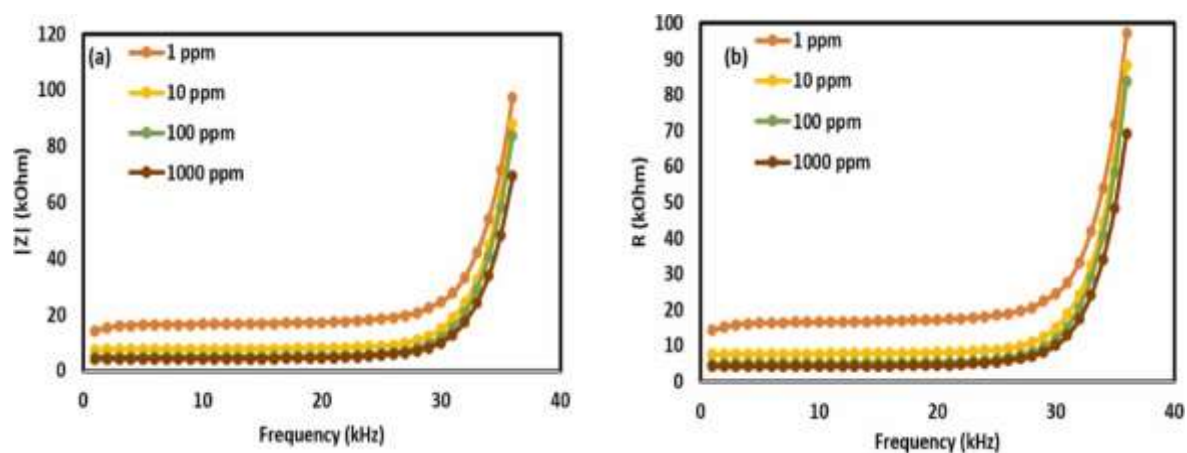


Figure 3. 10 EIS responses of the LIG-IDE sensor towards GMP expressed in terms of (a) reactance and (b) resistance for the frequency range.

As shown in Figure 3. 10 for GMP, the reactance value is drastically decreasing as frequency increases and also shows a similar behavior as that of L-Tryptophan because of the existence of a carboxylic group. Also, a secondary amino group in the structure of L-tryptophan and GMP accounts for its reactance characteristic. At higher frequencies, the double bond in the oxygen in carboxylic group generates a rise in current which causes reducing the reactance value also the polarization of the oxygen atom causes increases in the electronegativity and which directly affects double layer capacitance at electrode-electrolyte interface [49]. Figure 3. 11 depicts that lowering the concentration level of L-

tryptophan causes increases in the impedance value because the shortening of the capacitance layer at the interface relies on the decrease in different concentration levels.

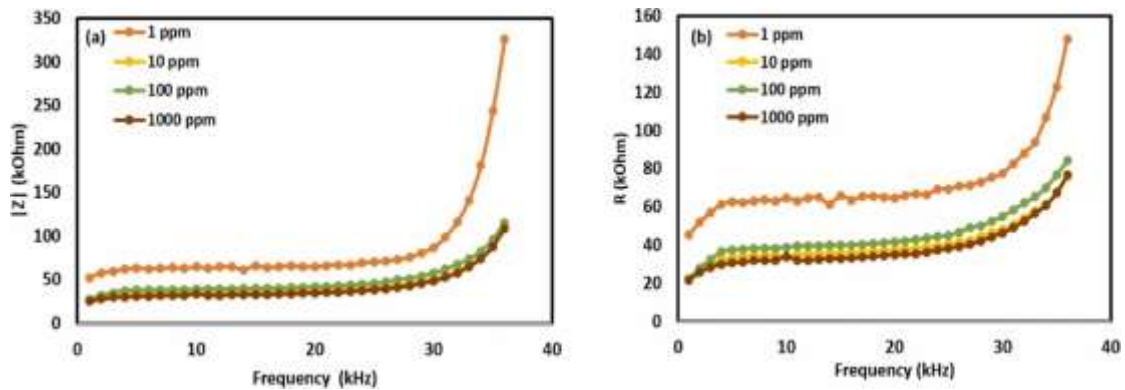


Figure 3. 11. EIS responses of the LIG-IDE sensor towards L-Tryptophan expressed in term of (a) reactance and (b) resistance for the frequency range.

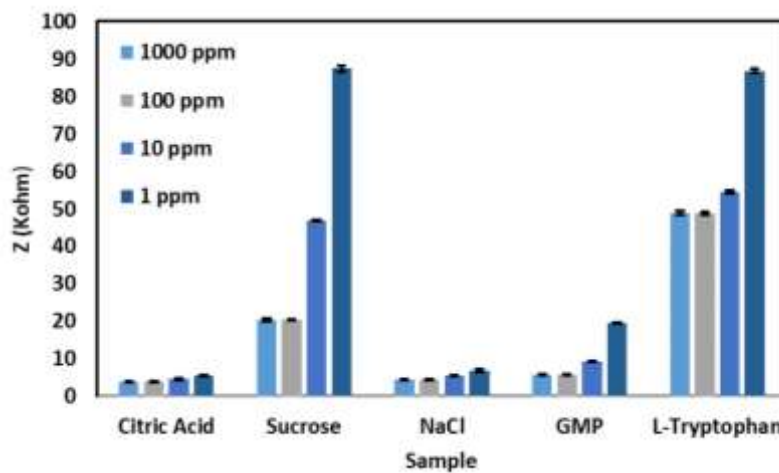


Figure 3. 12 : Analysis of the LIG-IDE sensor responses to several chemicals/samples at different concentrations. Error bar represents the standard deviations for three experiments.

Figure 3. 12 shows the analysis of the LIG-IDE sensor responses to several chemicals at different concentrations, also shows error bars representing the standard deviation for $n = three$. Although the responses for the two chemicals, L-tryptophan and sucrose are similar, the nature of the change in reactance values with increasing concentration differs. Reactive values at low frequencies for L-tryptophan and sucrose for two tested concentrations are very close to each other. This might create confusion for monitoring unit regarding the value of a specific concentration. To overcome this issue, it is needed to operate these sensors at higher frequency so that difference in capacitance value for time may act as the selective response of the LIG-IDE sensor as shown in Figure 3. 13.

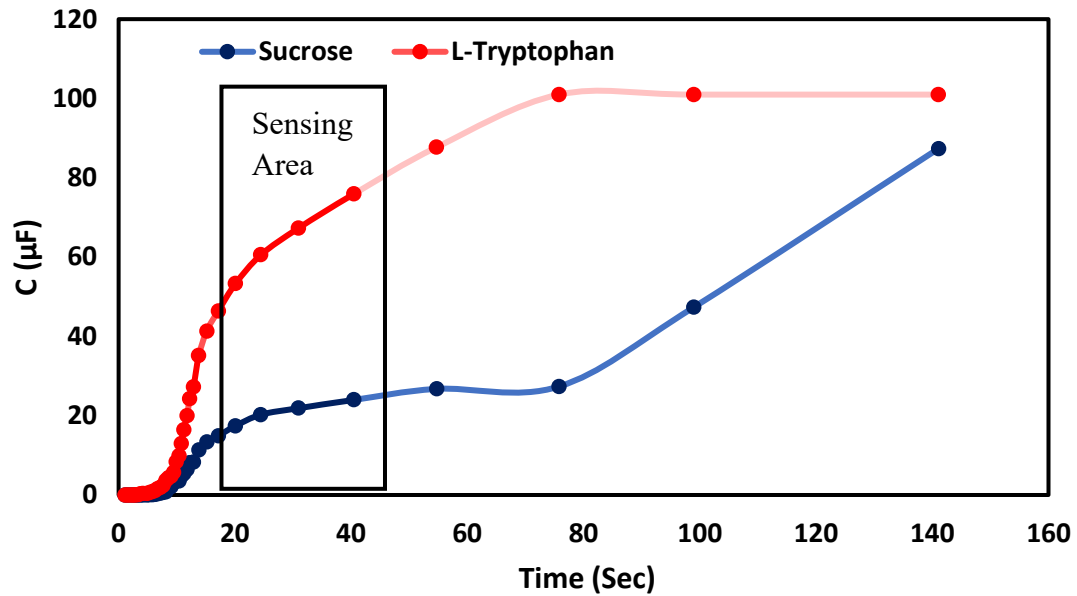


Figure 3. 13: EIS responses of the LIG-IDE sensor towards two different chemicals expressed in terms of C for time.

The LIG-IDE sensor can differentiate between each chemical based on a change in impedance value, as evidenced by the comparative responses of the reactive values and capacitive values for interfering analytes. Table 3. 3 summarizes the recent work reported using interdigitated electrodes for various sensing applications leveraging time-consuming, expensive fabrication methods, electrode material, and expensive cell and electrode manufacturing equipment, with higher a limit of detection. However, the fabrication of a microfluidic sensor should be simpler, with less sample volume requirement, have a lower limit of detection, and be inexpensive. These factors are achieved by realizing the microfluidic LIG-IDE device using a CO₂ laser.

Table 3. 4: Summary of research work reported using Interdigitated electrode sensing.

Sr No.	Electrode Structure	Substrate	Fabrication Method	Analyte Sensing	Limit of detection Range	Reference
1.	Interdigitated Electrodes	Polyimide Sheet	CO ₂ Laser engraving	Taste sensing	1ppm to 1000ppm	[50]
2.	Three Electrodes setup	-	Lipid Membrane Engraving	Taste sensing	0.0025 mM	[51]
3.	Interdigitated Electrodes	Polyimide Sheet (thickness of 120 μm)	CO ₂ Laser engraving	Salinity Sensing	4 ppm to 40000 ppm	[52]
4	Interdigitated Electrodes	Microscopic Glass	Inkjet-Printing Technique	Taste stimuli Sensing	1 ppm to 50 ppm	[53]
5.	Three Electrodes setup	-	lipid/polymer membrane	Taste sensing	1 ppm	[54]
6.	Microfluidic Interdigitated Electrodes	Polyimide Sheet (thickness of 254 μm)	CO ₂ Laser engraving	Taste sensing	1ppm-1000ppm	Proposed Work

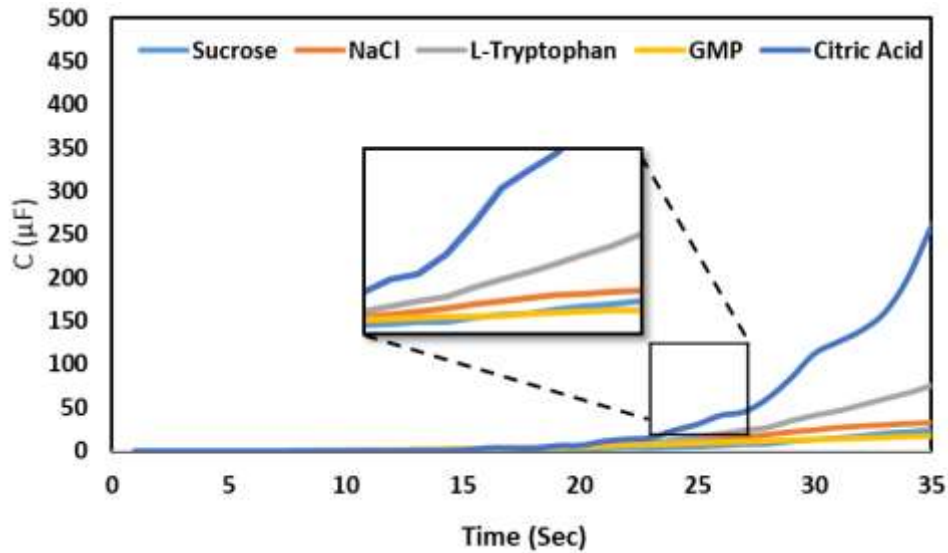


Figure 3. 14: EIS responses of the LIG-IDE sensor towards different chemicals expressed in terms of C for time.

The 100 ppm concentration was chosen for the time-dependent analysis of capacitance formation at the interface (C). The change in capacitance value for time represents information about the dielectric property of the sample. Figure 3. 16 depicts the difference in capacitance expressed in μF for five different chemicals. It was observed that citric acid seemed to have the highest variation in capacitance as time progressed. The graph shows that L-tryptophan and citric acid have different charge distribution capacities despite having a similar chemical structure [20, 26]. GMP and sucrose have nearly the same capacitive value for time increase, which can be correlated with Figure 3. 8 and Figure 3. 10, respectively. Moreover, NaCl exhibited a capacitance range between L-tryptophan and sucrose.

The response of the sensor can be estimated by measuring the value of the impedance after adding different analytes. The response of the sensor in percentage is considered as

$$\text{Sensor Response (\%)} = \frac{\text{Impedance of NaCl}_{1000\text{ppm}} - \text{Impedance of analyte} \times \text{ppm}}{\text{Impedance of NaCl}_{1000\text{ppm}}} * 100$$

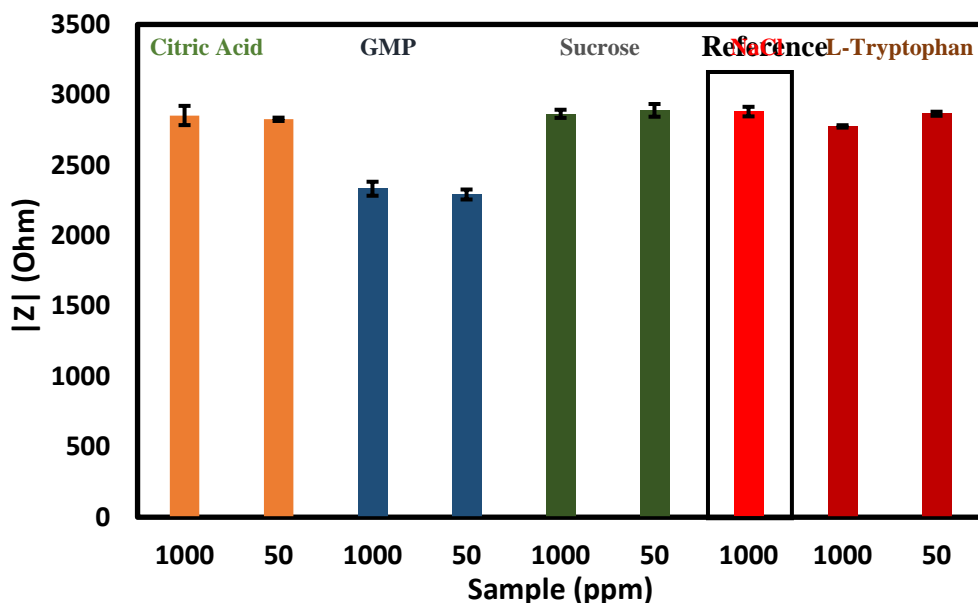


Figure 3. 15: Sensor response in impedance change toward different analytes at 100 ppm and 50 ppm with NaCl (1000 ppm) as reference analyte. Error bar represents the standard deviations for three independent experiments.

By mixing 1000 ppm NaCl with different concentrations (1000 ppm and 50 ppm) of different analytes such as GMP, citric acid, sucrose, and L-tryptophan, the sensor response to different analytes for selectivity analysis is shown in Figure 3. 15. The analytical competence of the device in terms of selectivity toward 1000 ppm NaCl is proven in Figure 3.15 by the least % change in impedance value for sucrose and citric acid. The differences in impedance observed for NaCl, on the other hand, are affected by 50 ppm and 1000 ppm GMP. The error bars from various experimental values, which were repeated for n=3, are depicted in the graph.

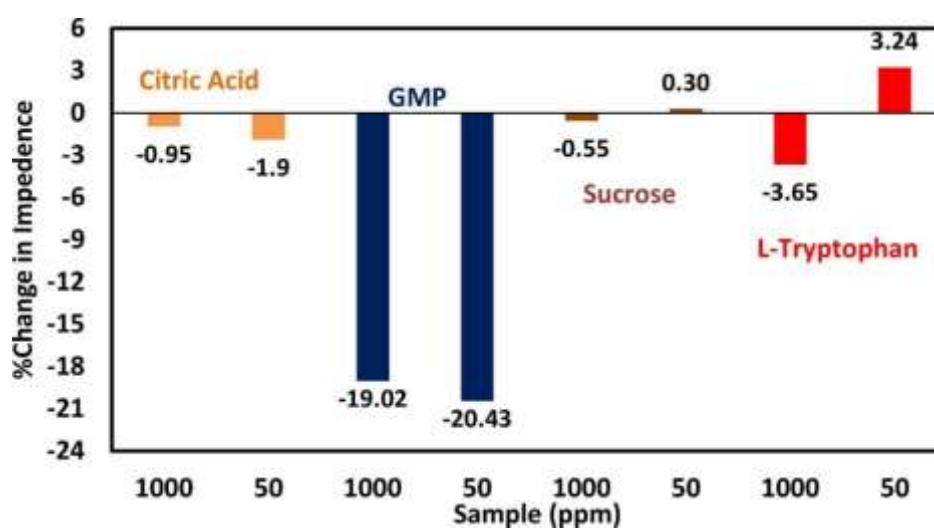


Figure 3. 16: Sensor response to different concentration (ppm) in terms of % change in impedance as a reference to NaCl

As shown in Figure 3. 16 the sensor response to citric acid was 0.95 % for 1000 ppm and -1.9 % for 50 ppm, while the response to GMP was -19.02 % for 1000 ppm and -20.43 % lower for 50 ppm. Further, the response to sucrose was -0.55 % lower for 1000 ppm and 0.3 percent higher for 50 ppm also response to L-Tryptophan was -3.65% lower for 1000 ppm and 3.24% higher for 50 ppm than for selective response to NaCl. The least % change in impedance shows efficient selectivity toward reference analyte NaCl. This sensing method is not necessary for GMP as it is adsorbed and desorbed easily from the sensing surface, and that is why the proposed sensor is highly selective towards salinity (NaCl).

3.5. Real Sample Analysis:

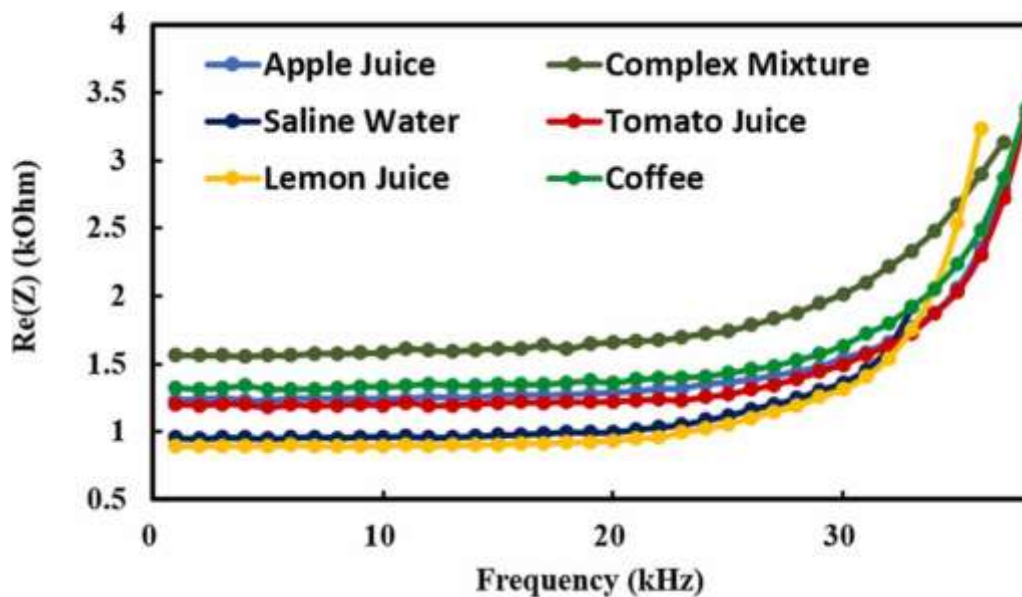


Figure 3. 17: Plot shows the real sample analysis

Figure 3. 17 shows the taste pattern constructed from apple juice (sweetness), coffee (bitterness), saline water (saltiness), tomato juice (unami) and lemon juice (sourness), and complex mixture (mixing in the same ratio). The taste patterns were evaluated using the linear transformation of sensor output obtained from the measurement of resistance value over the lower to higher frequency range, manifesting the resistance variation at different frequencies. It was observed that the impedance amplitude Z varied for different tastes in the measuring frequency range from 0.1 kHz to 10 kHz. When the frequency was lower than 25 kHz, there was almost no further impedance amplitude change. So impedance amplitude change at a range of 27 kHz to 36 kHz was used as the characteristic frequency to measure impedance amplitude [56]. It is also observed that complex mixture and coffee have least conductivity among the five tastes, as is obvious from the comparative reactance value in Figure 3.17. Likewise, lemon juice and saline water had the highest conductivity, related to the least impedance compared with the

impedance value for the respective chemicals. Apple juice and tomato juice were found to be the second and third least conductive tastes based on the stability of the source (chemical) present in them.

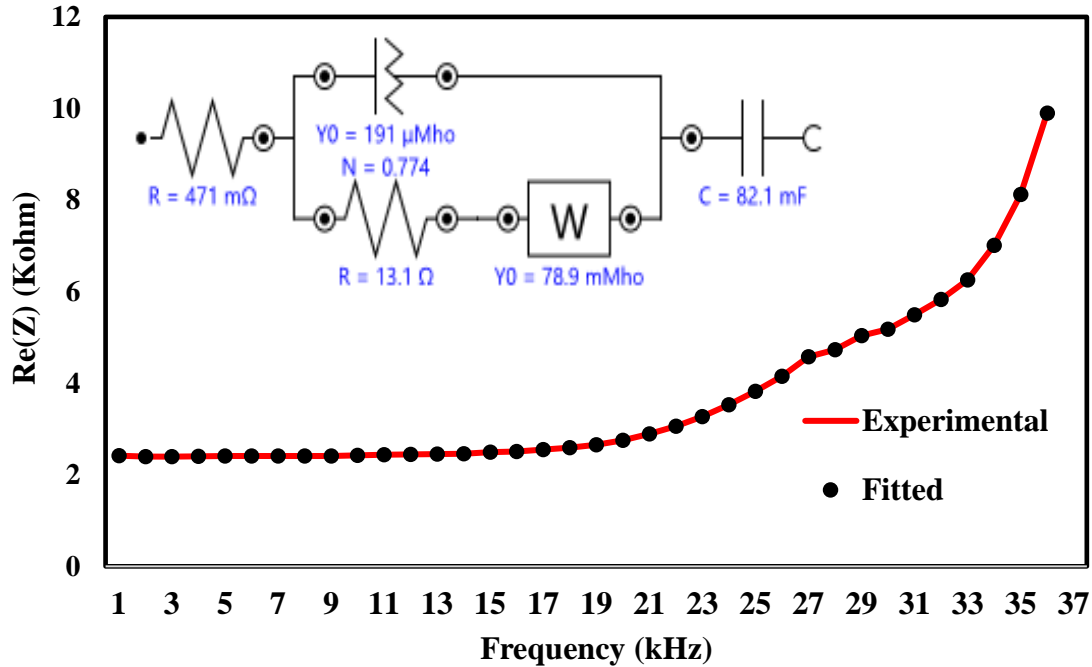


Figure 3. 18 Impedance spectra in the sensing area for 100 ppm NaCl with fitting curves and inset illustrates equivalent model to present the electric behaviour of sensing area at 100 ppm NaCl.

During the experiment, firstly impedance spectra of normal deionized water with laser-induced graphene electrodes were measured to analyze the impedance signal change prior and after the addition of analytes. An equivalent circuit model was used to present the electric behaviour of sensing area through laser-induced graphene in Figure 3. 18 (equivalent circuit) in NaCl. In this circuit, R is the resistance of NaCl solution, Z_{CPE} is the constant phase element (CPE) presents the electrochemical impedance of the electrode surface. Here, the Electrochemical impedance Z_{CPE} is represented by the following equation:

$$Z_{CPE}=[Y_0(j\omega)^m]^{-1},$$

where $-1 < m < +1$, Y_0 is admittance which is independent of frequency and has unit S/cm^2 . When $m = -1$, the Z_{CPE} is a pure inductor, and when $m = 0$, the Z_{CPE} behaves as a pure resistor; and when $m = 1$, Z_{CPE} is a pure capacitor. For LIG-IDE device, the value of m was found to be 1 proving CPE is a pure capacitor that strongly supports the good electrochemical behavior of LIG-IDE design. After adding NaCl in the measurement frequency range of 0.1 Hz to 10 kHz, it was evident that the impedance amplitude increased. Around 23 kHz, impedance variation reached its maximum. Almost no further impedance change was observed when the frequency is lower than 23 kHz. In the experiments,

impedance amplitude changes at 23 kHz was chosen as characteristic frequency for measuring impedance amplitude variation.

3.6. Conclusion

In this work, a Microfluidic LIG-IDE-based taste sensor has been designed and developed for sensing five different tastes. The LIG-IDE sensor was fabricated by the CO₂ laser engraving technique. It can be seen that the LIG-IDE sensor was capable of customizing the chemicals through diverse sensor responses with different chemicals and their respective real samples. The sensor responds to the tested chemicals were significantly repeatable with different concentrations ranging from 1 ppm to 1000 ppm with a minimum detection limit of 1 ppm. This proposed microfluidic device needs a low sample volume (2 μ L) and is independent of different atmospheric parameters, like humidity and temperature, that makes it operatable under different conditions. Sucrose and GMP have the least micromolar limits of 2.92 μ M and 2.45 μ M respectively, while L-Tryptophan and citric acid have the least micromolar limits of 4.89 μ M and 5.205 μ M respectively. One of the challenges that need to address with this device is the fact that reactance and capacitance value nearly overlap for two different structure chemicals, which creates a challenge to monitor this parameter simultaneously. The main advantages of the device include that it has a lower detection limit than the human sensing threshold, which is useful for a variety of taste sensing applications with selective analytical competence of the device toward different analytes especially NaCl. In next chapter, we will focus on the surface modification of the Laser-Induced Graphene (LIG) within the microfluidic reservoir. The microfluidic channels in the biosensor can be designed to allow for the storage of a sample containing different biomolecules like dopamine, Ascorbic acid which can then interact with the receptors on the sensor surface, leading to measurable changes in the sensor output signal. Further research and optimization of surface modification techniques for LIG with aid of additive manufacturing microfluidic reservoirs can open up new opportunities for the development of advanced microfluidic devices with enhanced performance and functionality.

CHAPTER 4:

STEREOLITHOGRAPHIC MICROFLUIDIC DEVICES WITH ENHANCED LASER-INDUCED GRAPHENE BIO ELECTRODE FOR ELECTROANALYTICAL DETECTION

This chapter presents a study for the integrated microfluidic device with laser-induced graphene (LIG) bioelectrode enhanced with MXene for the sensitive and selective electroanalytical detection of dopamine. The LIG bioelectrode was fabricated on a flexible polyimide substrate using a CO₂ laser, and its electrochemical properties were enhanced by coating it with a thin layer of MXene. The microfluidic device was designed to facilitate the electrochemical detection of dopamine in a small volume of sample solution. The performance of the integrated device was evaluated by measuring the electrochemical response of dopamine in a phosphate-buffered saline solution. The results showed that the LIG/MXene bioelectrode exhibited excellent electrochemical activity towards dopamine, with a low detection limit and a high selectivity over interfering compounds. The integrated microfluidic device with the LIG/MXene bioelectrode demonstrates great potential for the development of portable and sensitive electroanalytical devices for the detection of dopamine in biological and clinical applications.

4.1. Introduction:

Dopamine is a catecholamine neurotransmitter found in almost all species, including humans. Disruptions in dopamine create a role in the process of some severe central nerve illnesses. Thus, monitoring and maintaining required the levels of these neurotransmitters are essential not only for interpreting signal routes and nervous system functions but also for diagnosing and treating a wide range of brain-related diseases[56]. Electroanalytical detection, particularly based on voltammetry, colorimetry, electrochemiluminescence, and amperometric approaches [57][58] leads to various disadvantages due to numerous aspects[29]. The selectivity of the devices, however, is a crucial issue that must be addressed because of the overlapping oxidation potential of dopamine with numerous different chemicals found in the central nervous system.[59]. Because of their enormous availability in blood serum and urine samples (much higher than dopamine) and similarity to dopamine, xanthine (Xn), L-cysteine (L-C), uric acid (UA), and ascorbic acid (AA) have been identified as the major interfering species[60][59]. To selectively sense dopamine, bioelectrode materials, including the development of 2D nanomaterials, with the required attributes are needed. However, there are many challenges to overcome, such as interference from other biochemicals and low dopamine peak oxidation signals[61]. When developing electrode surfaces, the sensitivity, and selectivity of electrochemical biosensors might be strengthened by using nanomaterials with superior electrical and large surface area characteristics[62][63]. Karim et al. proposed the sensitive detection of the catechol by layer-by-layer (LBL) assembly of negatively charged poly(sodium 4-styrene sulfonate) with enzyme tyrosinase and positively charged hexadecyltrimethylammonium coated gold nanocubes. Such LBL assembly of nanomaterials or metallic and polyelectrolytes, with positively and negatively charged nanoparticle

layers, might be a feasible alternative[64]. Various functional materials and compounds, especially various 2D nanomaterials, have been used to enhance the active surface area of the bioelectrode to improve its performance for multianalyte analysis. However, most of the 2D nanomaterials use randomly structured immobilizing matrices, resulting in poor electrical connections with the current collector of the electrode and low 2D nanomaterial utilization efficiency for immobilization of enzymes[65].

2D metal carbides or nitrides, also called as MXenes (Ti_3C_2), have suitable morphology for sensing. MXene nanosheets have acquired attention owing to the fact that it can give an effective method for enhancing the porosity of matrix, interfacial coupling, diffusivity of ion, and improved electrode performance, depicting its key role for usage as an immobilization matrix [66], [67]. Recent studies showed that the immobilization with exfoliated MXene electrodes is suitable to obtain a significant distinguishing of oxidation potential for both dopamine and other biochemicals, which could improve the selective sensing of dopamine (increased voltammetric current signals)[68]. Jin X et. al reported that to facilitate charge transport and reduce constriction resistance at the interface between MXene and current collector (polyamide sheet), laser-induced graphene (LIG) was used as conductive bridges [69][7].

In this work, the LBL biosensor consists of an as-synthesized MXene coating with a dense bottom porous graphene layer and a highly porous intricate top matrix network layer. This configuration provides an ideal structure for a highly sensitive effective surface area and perfect entrapment for laccase enzymes (i.e., the active Ti_3C_2 network is inextricably linked to the conducting LIG support). Because laccase is sensitive to its environment, an enclosed microfluidic platform was required to maintain the sensitivity of enzymes with dopamine[70]. One of the important parameters is to control the surface properties and spatial arrangement of the functional biomolecules inside a microchannel for designing neurotransmitter diagnostics. Ali et.al. used the lithography technique for fabricating the microfluidic environment, which is a very expensive technique and a multistep process [71].

In order to resolve this limitation, a simple desktop 3D printer has been utilized here. It is a low-cost method for preparing a 3D-printed microfluidic case in a polymer substrate. The method has advantages in terms of designing and preparing 3D complicated structures economically and rapidly[72]. Therefore, herein, the LBL biosensor was then encased in a 3D Printed microfluidic enclosure. The sensing properties of MXene are due to its metallic conductive nature, biocompatibility, several adsorption sites, and excellent homogenous dispersion in the aqueous medium [73]. Following this, a reduced electrical signal-to-noise ratio, lower detection limit, and improved signal toward dopamine is obtained. The L- Ti_3C_2 -G biosensor has a conducive biosensing capacity with lower LOD along with a larger linear range due to the following factors. First, a large specific surface area of the MXene matrix potentially enhances the effective surface area of the LIG bioelectrode and its accessibility to enzyme

immobilization, resulting in a higher enzyme surface loading amount. Evidently, redox-active sites in the enzymes are effective for the immobilization of matrix, and L-Ti₃C₂-G and Ti₃C₂-G are conducive for improving the electrochemical performance of the redox-active site in the plane. Nafion aids in the solubility of Ti₃C₂-G composites, ensuring that the MXene is well-dispersed and develops a homogeneous and stable coating on the graphene surface even after long durations. The enhanced activity of laccase in the existence of MXene nanoparticles is associated with the sensing capability of L-Ti₃C₂-G. The modified LBL biosensor was used to monitor dopamine concentrations in blood serum and synthetic urine. The peak current changes involved with the surface site-specific electrocatalytic reaction of the substrate dopamine and the enzyme laccase assembled on Ti₃C₂-G lead to the detection of dopamine up to 0.47 nM. Further, the co-existing biochemicals, that are likely to interfere with dopamine, were also tested. It was found that the fabricated device gave a selective response for the various biochemicals at distinct E₀ values. Hence, the fabricated device can be applied for the simultaneous sensing of multiple analytes. In addition to this, real-time blood serum and synthetic urine samples were also tested for dopamine sensing that displayed appreciable recovery values.

4.2. Materials and Methods:

Biochemicals, like dopamine (D), xanthine (Xn), L-cysteine (LC), uric acid (UA) and ascorbic acid (AA), buffer salts like sodium phosphate monobasic dehydrate (NaH₂PO₄) and sodium phosphate dibasic anhydrous (Na₂HPO₄.2H₂O), Nafion (5% (w/w) in mixed alcohols), ethanol, Ti₃AlC₂ powder Isopropyl alcohol (IPA), laccase (EC 1.10.3.2 from *Trametes Versicolor*, 1.34 U.mg⁻¹) were procured from Sigma-Aldrich Co. Ltd. The solution of hydrofluoric acid (HF, 57 wt%) was obtained from Macklin Co. Ltd. Double-distilled water (18.2 MΩ.cm⁻¹) was used throughout the experiment.

4.3. Solution and sample preparation:

0.1 M of phosphate buffer solution (PBS) with pH ranging from 4.0 to 7.0 was prepared. The stock solution of laccase enzyme (0.3 mg.mL⁻¹) was made in 0.1 M PBS of 6.0 and was stored at 2°C till use. For MXene synthesis, Titanium Aluminium Carbide powder (Ti₃AlC₂, 99% purity, Nanoshell LLC, Punjab), Lithium fluoride (SRL India), and hydrochloric acid were used as starting materials and without any further purification. 0.20 g of KCl, 5.0 g of NaCl, 1.1 g of Na₂HPO₄, 0.20 g of NaH₂PO₄, and 21 g of urea were dissolved in 500 mL of double distilled water to make synthetic urine then the pH was calibrated to 3.5 using H₂SO₄ (1 M) and blood serum was taken from Medical Center, BITS Pilani Hyderabad campus. A polyamide sheet (PI) of 254 μm, used as a current collector, was procured from DuPont, India. The LIG conductive electrodes were fabricated using a 30 W CO₂ Laser (VLS 3.60 from Universal Laser Systems, USA). Scanning Electron Microscope (SEM) and EDX were performed with a Scanning Electron Microscope (SEM) (Apreo from Thermo Fisher Scientific, USA). All the CV and SWV measurements were performed utilizing an electrochemical workstation (SP-150 from Biologic, France) in the 3-electrode arrangement.

4.4. Synthesis of layer by layer assembly of the bio electrodes:

A 6 M solution was prepared by diluting 4.927 mL of concentrated HF in 2.5 mL DI water and adjusting the final volume to 10 mL by adding more DI water. To prevent an exothermic reaction, about 1 gm of Ti_3AlC_2 (MAX phase) powder was mixed into the combined solution after the salts were completely dissolved and the resultant suspension was stirred for 24 h slowly at ambient temperature.

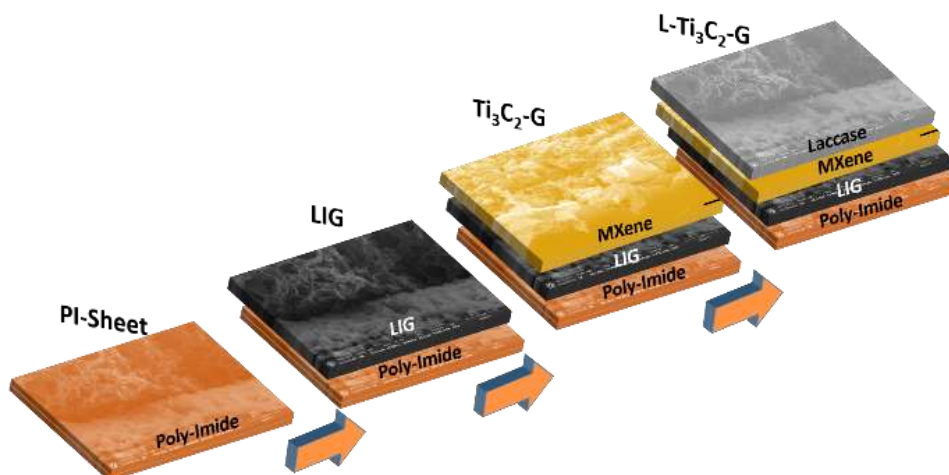


Figure 4. 1 Schematic representation for LBL Synthesis Process for L- $\text{Ti}_3\text{C}_2\text{-G}$ Bio-Electrode.

Consequently, the resultant solution was washed and centrifuged (4000 rpm for 10 min) repeatedly with DI water followed by centrifugation and decanting of the supernatant solution until the pH reached a value of 6. Finally, the obtained slurry was air-dried after filtering and then delaminated in Dimethylsulfoxide (DMSO) using the probe sonication method under inert conditions for 40 min. The obtained stable Ti_3C_2 colloidal solution was used for further processing.

4.5. Fabrication and integration of the bioelectrodes in the microfluidic chambers:

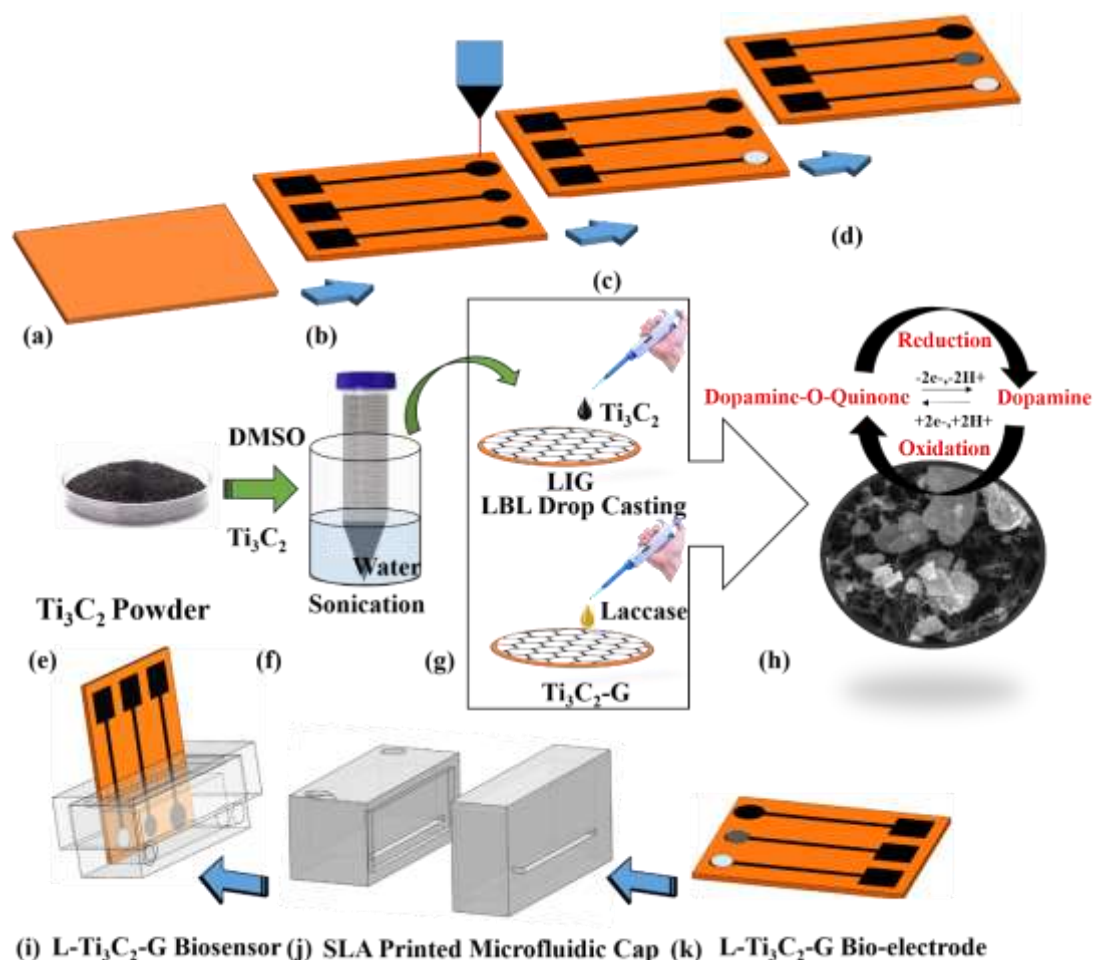


Figure 4. 2: Schematic illustrates the synthesis of Bioelectrode and fabrication flow of Biosensor (a) Polyamide Sheet (b) Laser engraved Electrodes (c) Ag/AgCl coated Reference Electrode (d) L-Ti₃C₂-G Working Electrode. (e) Ti₃C₂ Powder (f) Sonication (g) LBL Drop Casting (h) L-Ti₃C₂ Bio-electrode catalytic activity (i) 3-Electrodes on polyamides, (j) 3D printed Microfluidic cap, and (k) Complete prototype of the fabricated biosensor.

A schematic for the LBL synthesis process of bio electrodes is illustrated in Figure 4. 2. First, a design with a three-electrode system was created which is similar to the one earlier reported. These three electrodes were engraved on the PI sheet as a current collector using a CO₂ laser engraver as shown in Figure 4. 2 (a)-(b). One of LIG electrodes with a modified surface was used as a working electrode, a bare LIG electrode as an auxiliary counter electrode, and Ag/AgCl coated LIG electrode as a reference electrode as can be seen in Figure 4. 2 (c). The L-Ti₃C₂-G as a working electrode (shown as final bio electrode in Figure 4. 2 (d)) was fabricated as follows. First, LIG was synthesized by the optimized laser parameters (1.8 W and 112.5 mm.s⁻¹) as reported in the previously published work by our group[37]. Herein, the PI sheet was kept in the CO₂ laser engraver and LIG electrodes were patterned at the

positions as designed using the parameters mentioned above. The prepared MXene delaminated solution was coated over LIG as shown in Figure 4. 2 (e)-(f). 0.2 μL of Nafion, was used for the formation of the Ti_3C_2 layer over the LIG surface. 5 mg of laccase enzyme was dispersed in 1 ml of the phosphate buffer solution kept at 4°C . Later, 2 μL of the laccase enzyme solution was cast onto the dried $\text{Ti}_3\text{C}_2\text{-G}$ sheet. Thereby, the L- $\text{Ti}_3\text{C}_2\text{-G}$ bioelectrode has been fabricated using LBL assembly of a positively charged MXene coated on LIG complexes ($\text{Ti}_3\text{C}_2\text{-G}$) and a negatively charged laccase enzyme, as shown in Figure 4. 2 (g) [3]. As shown in Figure 4. 2 (h), the modified electrode L- $\text{Ti}_3\text{C}_2\text{-G}$ was utilized for the oxidation of dopamine as discussed in a further section of the reaction mechanism. The $\text{Ti}_3\text{C}_2\text{-G}$ electrode (without the laccase enzyme) was synthesized by a similar technique for comparative study. The L- $\text{Ti}_3\text{C}_2\text{-G}$ as the working electrode was subsequently enclosed in the microchannel of a microfluidic device fabricated via stereolithography (SLA) based 3D printing technique for establishing a leakage-proof microfluidic environment. The sensing area of the miniaturized device was $3\text{ mm} \times 10\text{ mm}$. As a proof of concept, for sensitivity and selectivity toward modified bioelectrode, this device was evaluated for different biofluids including untreated blood serum and synthetic urine for detecting dopamine, l-cysteine, uric acid, xanthine, and ascorbic acid. The microfluidic device with integrated bioelectrodes is shown in Figure 4. 2 (i)-(k). A 3D CAD modeling software (Solid works 2021) was used to design $5 \times 15\text{ mm}^2$ rectangular boxes. The SLA 3D printed design was used to create a microfluidic device with an inlet and outlet as shown in Figure 4. 2 (j) with a sample volume requirement of $150\text{ }\mu\text{L}$. Laccase molecules are trapped by $\text{Ti}_3\text{C}_2\text{-G}$ due to its large specific surface area, which accumulated on Ti_3C_2 surface functional groups (Figure 4. 2 (c)). Nafion was preloaded onto $\text{Ti}_3\text{C}_2\text{-G}$ to provide matrix stability while also regulating the accuracy and sensitivity of the device for dopamine sensing[70]. As depicted in Figure 4. 2 (b)-(c), on the LIG electrode, a thin layer of laccase was developed. The high porosity of the uniform film of laccase on $\text{Ti}_3\text{C}_2\text{-G}$ enhanced the improved bioelectrodes-specific surface area, resulting in enhanced performance characteristics of fabricated biosensors. Also, such a 2D matrix is suitable for allowing trapped enzymes to sustain their biological properties and for enzymatic molecules to be transported efficiently

4.6. Material Characterization:

The different material characterization like SEM, XRD, UV spectroscopy, and EDX characterization was conducted on L- $\text{Ti}_3\text{C}_2\text{-G}$ bioelectrode. Figure 4. 3 depicts the morphology of the synthesized and modified surface of MXene (Ti_3C_2). Layers over honeycomb structure of the LIG, like multilayer nanostructure Ti_3C_2 , are observable in synthesized $\text{Ti}_3\text{C}_2\text{-G}$ crystallites (Figure 4. 4 (a)). The unique 2D graphene structure provides conductive bridges to facilitate charge transport and mitigate the constriction resistance at the interface between the Ti_3C_2 and the current collector (PI sheet).

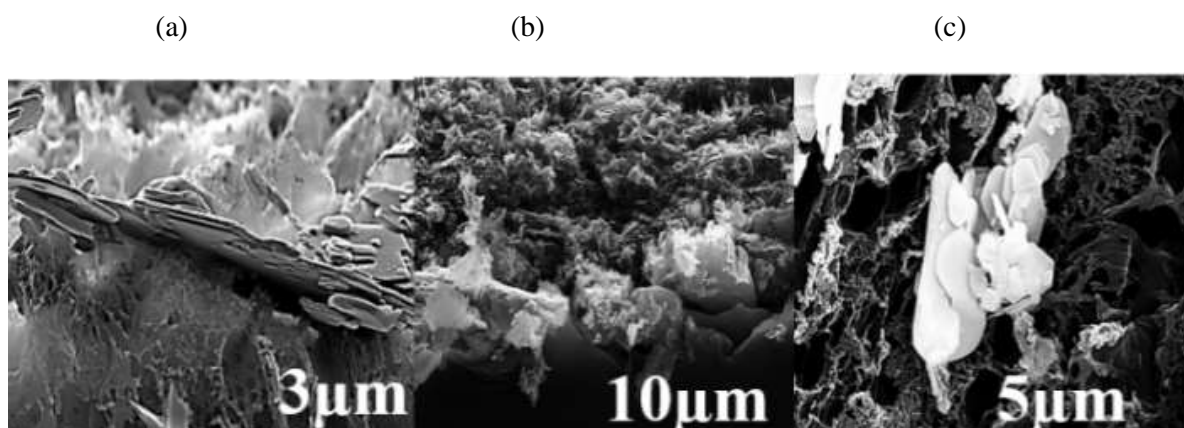


Figure 4. 3 Scanning Electron Morphology of (a) Ti_3C_2-G (b) $L-Ti_3C_2-G$: Immobilization of laccase on Ti_3C_2-G (c) $L-Ti_3C_2-G$ bioelectrode.

Laccase molecules are trapped by Ti_3C_2-G due to its large specific surface area, which accumulated on Ti_3C_2 surface functional groups. Nafion was preloaded onto Ti_3C_2-G to provide matrix stability while also regulating the accuracy and sensitivity of the device for dopamine sensing [17]. As depicted from Figure 4. 3 (b)-(c), on the LIG electrode, a thin layer of laccase was developed. The high porosity of the uniform film of laccase on Ti_3C_2-G enhanced the improved bioelectrodes-specific surface area, resulting in enhanced performance characteristics of fabricated biosensors. Also, such a 2D matrix is suitable for allowing trapped enzymes to sustain their biological properties and for enzymatic molecules to be transported efficiently.

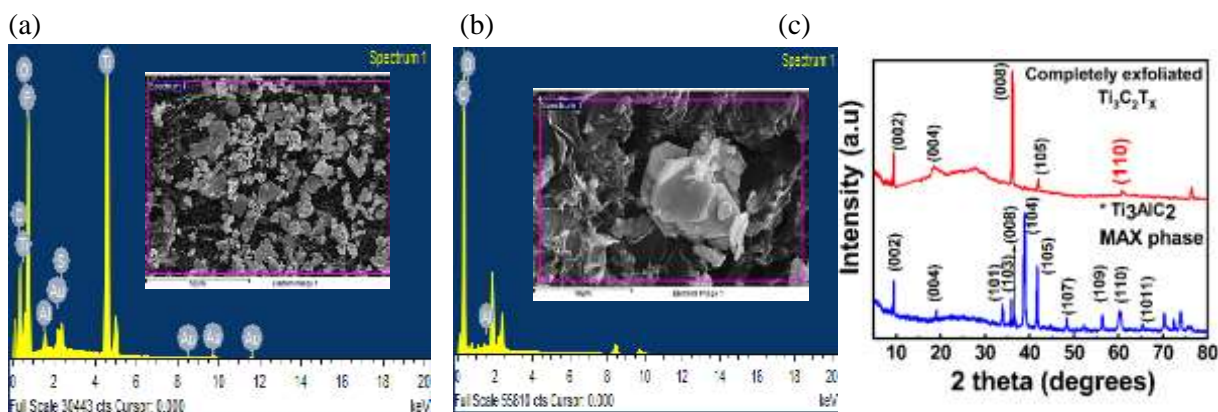


Figure 4. 4: Spectra of energy dispersive spectroscopy mapping of (a) $L-Ti_3C_2-G$ (b) Ti_3C_2-G , (c) XRD patterns of $Ti_3C_2T_x$ and Ti_3AlC_2 .

The spectra of energy dispersive spectroscopy (EDS) and XRD in Figure 4. 4 (a)-(b) show that, for Ti_3C_2 , the aluminum peak almost vanished and the fluorine element appeared, meanwhile the percentage of oxygen markedly increased compared with (MAX powder) Ti_3AlC_2 , implying the generation of numerous surface-terminating groups after etching. Elemental mapping inset displays that each element was evenly distributed including O and F, suggesting uniform dispersion of the

termination groups on the L-Ti₃C₂-G surface. As depicted from Figure 4. 4 (c), the x-ray diffraction patterns reveal a clear distinction between Ti₃AlC₂ (MAX phase) and MXene (Ti₃C₂T_x) as shown in Figure 4.4 (c). The diffraction data attained for Ti₃AlC₂ matches with JCPDS card no. 52-0875 and comprises of 9.52° (0 0 2), 19.20° (0 0 4), 34° (1 0 1), 35.93° (1 0 3), 38.82° (0 0 8), 39.04° (1 0 4), 41.82° (1 0 5), 48.55° (1 0 7), 56.40° (1 0 9) planes, respectively. The successful etching away of Al from the MAX phase can be confirmed by the successful elimination of the 104 (39.04°) peak and the shifting of (9.52°) which agrees well with the previously reported literature [74].

4.7. Result and Discussion:

4.7.1. Electro catalytic behaviour of the Biosensor

The L-Ti₃C₂-G bioelectrode was tested for electrocatalytic activity toward dopamine sensing. Figure 4.5 (a) is a typical comparative CV of the optimal modified electrode in 1 mM dopamine solution with the blank electrodes for n=2, at 20 mV.s⁻¹ in pH 7 PBS. The oxidation and reduction peaks of redox probe potentials were more reversible when L-Ti₃C₂-G was used, showing effective electron transport in the presence of laccase immobilized over MXene. In terms of electrocatalysis, the oxidation peak current of dopamine on L-Ti₃C₂-G was 2.5 and 3.26 times higher than Ti₃C₂-G and L-G, respectively, demonstrating superior catalytic activity of MXene and a higher proportion of catalytically active sites. This effect can be explained by the fact that the electrostatic interactions of copper ions (present in laccase enzyme) with Ti₃C₂-G sheets neutralize the originally negative charges of the MXene surface-terminating groups (-OH, -O, -F), decreasing electrostatic repulsion and resulting in accumulation [67]. Adsorption of laccase ions is easily possible on the titanium molecules because of its erect position of the hydroxyl (-OH) group. The scan rate effect was used to demonstrate the stability of the electrode with that peak potential by sweeping at multiple scan rates from 20 mV.sec⁻¹ to 150 mV.sec⁻¹ with peak current at a constant potential as depicted in Figure 4. 5 (b). As can be seen, the oxidation current increases linearly when the scan rate is increased. In the inset of Figure 4. 5 (b), the plot of anodic peak current (I_{pa}) vs scan rate (mV.s⁻¹) was observed to be linear. The obtained regression coefficient was R₂ = 0.9972 from the inset graph, and the diffusion coefficient value was calculated with the Randles Sevcik equation.

$$I_{pa} = 2.69 \times 10^5 \times n^{\frac{3}{2}} A C D^{\frac{1}{2}} V^{\frac{1}{2}}$$

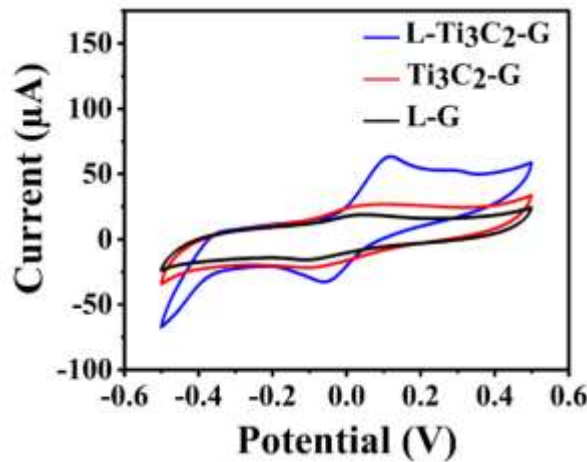
wherein, I_{pa}/V^(1/2) is the slope obtained from the inset linear plot of Figure 5(b), D is the diffusion coefficient = 4.38×10⁻¹²cm².s⁻¹, C is the 1 mM concentration of dopamine, A is an active electrochemical surface area of (3 mm²), n = the total number of electrons in the reaction are assumed as 2 based on reported reaction mechanisms, I_{pa} is the anodic peak current value (mA). This device has shown considerably better sensitivity and selectivity than previously reported dopamine biosensors, as shown in summary Table 4. 1. The functional characteristics of the dopamine biosensor are similar to the finest

reported results. According to these CV scans, oxidation peaks, in particular, correspond to the potential 0.11 V, which is amplified, and these peaks had higher currents in the presence of MXene (Ti_3C_2) than in the absence of it such as in the case of bare LIG.

Table 4. 1: Comparative assessment of analytical performances of electro-chemical biosensors obtained for dopamine determination based on 2D nanomaterials

#	Electrode	Detection Technique	Limit of Detection (μM)	Linear Range (μM)	Reference
1.	MoS ₂ /Laccase	CV	0.01	NA	[75]
2.	Graphene Ink	CV	0.1	1000	[76]
3.	GO/PEDOT: PSS	CV	1	1-1000	[77]
4.	PDA/ErGo/GCE	CV	2.3	10-200	[78]
5.	Cu/CuOx/NP	DPV	1.07	0.3-53	[79]
6.	Laccase-EPS-MWCNTs	SWV	0.127	2.99-38.5	[80]
7.	L-Ti ₃ C ₂ -G	SWV and CV	0.00047	0.001– 10	This work

(a)



(b)

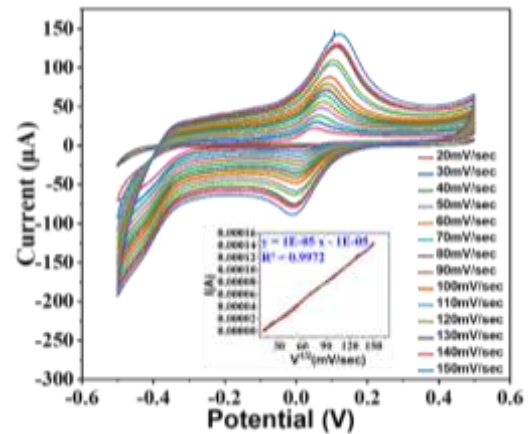


Figure 4. 5 Cyclic voltammetry of (a) Optimal L-Ti₃C₂-G and control electrodes with 1 mM dopamine in pH 7 PBS at 20 mV. Sec-1 for n=2. (b) Scan Rate effects of L-Ti₃C₂-G in 1mM dopamine concentration from 20-150 mV.sec-1 with inset showing correlating trendline calibration graphs of I_{pa} versus V^{1/2} oxidation peak currents.

Electrochemical characteristics of these bioelectrodes were compared in PBS solution. The cathodic or anodic peak voltage (E_{pc} or E_{pa}) and cathodic or anodic peak currents (I_{pc} or I_{pa}) are given in Table 4.2.

Table 4. 2: Cathodic/anodic peak current and cathodic/anodic peak potential for the electrodes for dopamine.

Bioelectrodes	E_{pc} (V)	I_{pc} (mA)	E_{pa} (V)	I_{pa} (mA)
L-Ti ₃ C ₂ -G	-0.05	-3.22	0.11	6.37
Ti ₃ C ₂ -G	-0.09	-2.14	0.018	2.54
L-G	-1.49	-0.1	0.02	1.95

4.7.2. Effect of varying concentration

Square wave voltammetry (SWV) is an excellent approach for the detection of different analytes as it is more precise and sensitive than cyclic Voltammetry (CV).

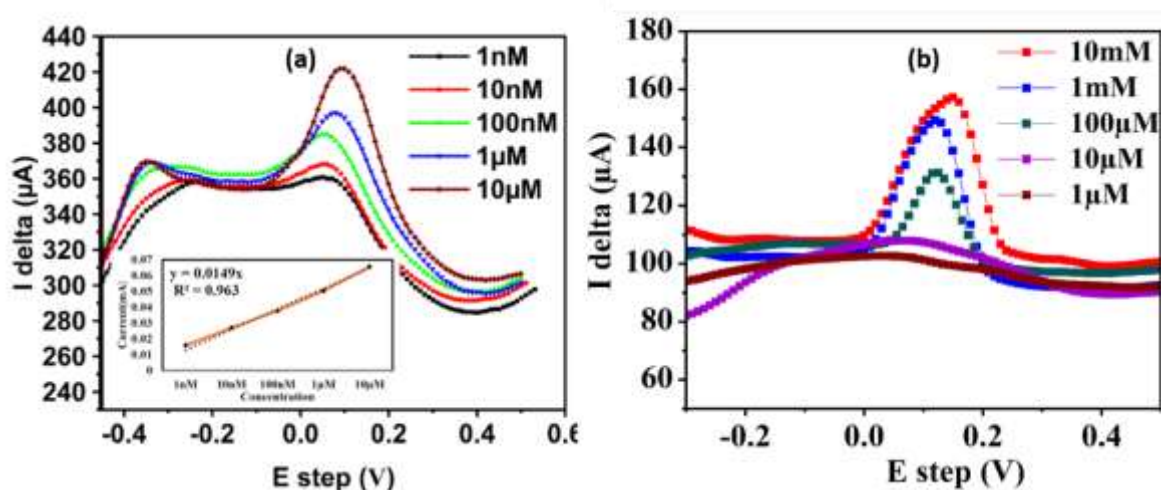


Figure 4. 6 Square wave voltammogram of (a) L-Ti₃C₂-G in PBS with different concentrations of dopamine (1 nM -10 μM) (b) L-Ti₃C₂-G in PBS with different concentration of dopamine (1 nM -10 μM) (b) L-G in PBS with different concentrations of dopamine (1 μM -10 mM)

As a result, SWV was chosen to examine the analytical capabilities of the L-Ti₃C₂-G for dopamine detection in PBS. Figure 4. 6 (a) depicts SWV profiles of the L-Ti₃C₂-G in PBS for different concentrations of dopamine (1 nM –10 μM). Figure 4. 6 (b) shows SWV for L-G for different concentrations of dopamine (1 μM – 10 mM). The current response and its linear relationship with dopamine concentrations are compared and depicted in Table 4. 2. Herein, a very low LOD = 0.476 nM and high current sensitivity (6.37 mA nM⁻¹ cm⁻²) were achieved. The LOD is determined by the equation $LOD = 3 \sigma / m$, where σ denotes standard deviation depicting peak current values for three measurements and m represents the slope for linear calibration plot shown in inset of Figure 4. 6. The LOD of the L-Ti₃C₂-G biosensor is lower than the other two fabricated dopamine biosensor devices presented in Table 4. 3.

Table 4. 3: Summary of limit of detection of bio-electrodes towards dopamine

Electrode	Limit of Detection for dopamine (Calculated)	Limit of Detection for Dopamine (Experimental)	Linear Range
L-Ti ₃ C ₂ -G	0.476 nM	1 nM	1 nM to 10 μ M
Ti ₃ C ₂ -G	1.03 μ M	1 μ M	1 μ M to 10 mM
L-G	1.81 μ M	1 μ M	1 μ M to 10 mM

4.7.3. Simultaneous determination of L-Cysteine, Xanthein, Ascorbic Acid, and Uric Acid at L-Ti₃C₂-G towards Dopamine detection:

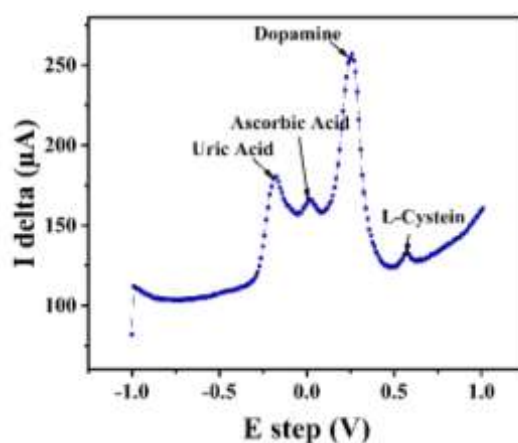


Figure 4. 7 SWV ($I \Delta$ Vs E step) for Simultaneous detection analysis of common interferent.

The mixture of these analytes was deposited on the bioelectrode, and the individual peak in the SWV plots, shown in Figure 4. 7, was distinguished by the bioelectrode, demonstrating the simultaneous sensing ability of the device. This plot obtained, for ascorbic acid, L-cysteine, xanthein, uric acid, and dopamine in a mixture at the L-Ti₃C₂-G bioelectrode with 0.1 M PBS solution, define distinctive oxidation peaks for the concentration of 1 M of each analyte at 0.50, 0.12, 0.62, 0.70, 0.10, and 0.42 V respectively [59]. For the sensitive and selective detection of dopamine at lower concentrations values in human blood serum, amplification of dopamine electrochemical response and distinction from quasi surface adhesion of interferents are required. [6]. The increased peak current of 1 mM dopamine after mixing with 1 mM concentrations of uric acid, L-cysteine, xanthein, and ascorbic acid at L-Ti₃C₂-G is shown in Figure 4. 7. The synergistic impact of MXene nanoparticles adsorbed on the graphene electrode surface can be used as a general technique to resolve the aforementioned flaws while also strengthening analytical performance. In comparison to individual CV, the oxidation potentials of all

analytes contained in the SWV were not significantly shifted. These findings corroborate that the L-Ti₃C₂-G device is well suited for detecting five distinct analytes simultaneously.

4.7.4. Reproducibility, Anti-interference (Selectivity), and Stability properties of biosensor

The repeatability of L-Ti₃C₂-G was evaluated before biological quantification by evaluating SWV responses of 5 different biosensors prepared independently at 1 mM concentration of dopamine as shown in Figure 4. 8 (a).

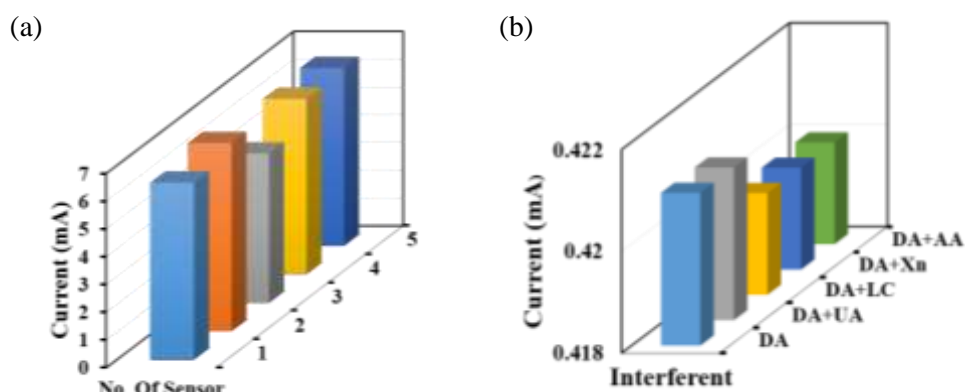


Figure 4. 8 (a) Reproducibility of L-Ti₃C₂-G biosensors for dopamine detection with fixed concentrations of 1mM were used in 0.1 M PBS (b)Anti-interference property of the biosensor (*Do=Dopamine, UA=uricAcid, LC=L-cysteine, Xn=Xanthein, AA=Ascorbic Acid)

The selectivity was determined by observing the impact of the interfering biological samples such as including 1 mM concentration of various biochemicals that co-exist in biological fluids. Selectivity of the developed bioelectrode was evaluated for dopamine detection in the existence of equal concentrations of certain five common interfering agents such as L-cysteine, ascorbic acid, xanthein, uric acid. As depicted in Figure 4. 8 (b), in the presence of strong concentrations of the interfering species, no substantial changes in the current were observed, demonstrating dopamine has superior selectivity over the other analytes. In both serum and synthetic urine samples, the maximum concentration values for the proportion ratios of ascorbic acid and dopamine, uric acid and dopamine were 1:1. Because these species may persist in blood serum and urine, SWV data were analyzed for possible interference with dopamine by uric acid and ascorbic acid. When the SWV responses were compared, it was evident that neither uric acid nor ascorbic acid interfered with the dopamine response depicting the fabricated L-Ti₃C₂-G biosensor is more selective towards dopamine[61]. It can be inferred that the electrocatalytic activity of the bioelectrode was efficient for the detection of dopamine with a linear ranging from 1 to 10⁶ nM, a LoD of 1.03 nM, excellent stability, repeatability, and reproducibility.

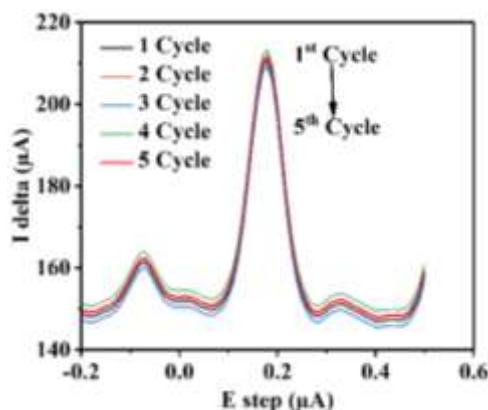


Figure 4. 9 Stability analysis using SWV plots of L-Ti₃C₂-G for continuous scanning of 5 cycles.

Figure 4. 9 demonstrates SWV for the use of L-Ti₃C₂-G in dopamine more than 5 consecutive times and the response peak current of L-Ti₃C₂-G attenuates negligibly. Finally, in this microfluidic biosensor, a continuous and steady reference signal was obtained. Due to the protective influence of the microfluidic cover, the activity of the laccase was intact and the biosensor exhibited zero surface leaching[37].

4.7.5. Real Sample Analysis in Blood Serum and Synthetic Urine

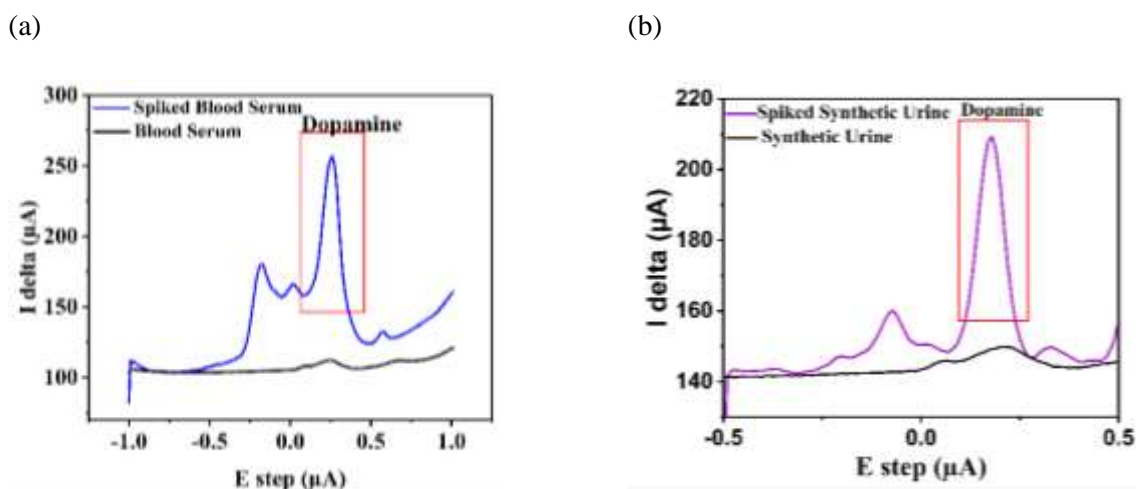


Figure 4. 10 SWV Graph for (a) Blood serum with and without spikes, and (b) Synthetic urine with and without spikes.

Different interferents were used to evaluate human blood serum. Dopamine detection in human blood serum and synthetic urine was performed to determine the evidence-based effectiveness of the proposed biosensor. The real sample blood serum was first evaluated to determine if there any dopamine was present, and it was observed that there was only one oxidation peak for dopamine in the blood serum, with a 2% shift in the potential as shown in blood serum and synthetic urine samples of the SWV graph in Figure 4. 10 (a) and (b) respectively. The samples were analyzed before and after spiking with known concentrations of dopamine standard. For cross-verification, the samples were developed by diluting

the blood serum in PBS and spiking with a required concentration of dopamine using the dilution technique. The spiking levels were based on the biological range in the human body with the electroanalytical quantification of dopamine in biological matrices.

Table 4. 4: Real sample sensing of dopamine in blood serum (n = 3) and synthetic urine

Analyte	Added (nM)	Found (nM)	Recovery (%)	Average recovery (%)
Dopamine in human blood Serum	100	91.35	91.35	97.08%
	50	48.35	96.7	
	10	10.32	103.2	
Dopamine in Synthetic Urine	100	93.36	93.36	97.81%
	50	51.29	102.58	
	10	9.75	97.5	

The relative average recovery is presented in Table 4. 4. The dopamine recovery percentage is in the corresponding range of 93.36 %, 102.58 %, and 97.5 % with an average recovery of 97.81 %. The modified bioelectrode was also tested for the real-sample detection of the dopamine content (100 nM) of synthetic urine samples. Before experiments, 100 nM, 50 nM, 10 nM of dopamine were directly diluted 20 times with 0.1 M PBS electrolyte. The results of the recovery tests, which were used to evaluate the reliability and accuracy, are shown in Table 4. 5. The dopamine concentration in the diluted solution was detected to be 93.36 nM, 51.29 nM, and 9.75 nM, and the corresponding recoveries were 91.35–103.2 % with an average recovery of 97.08 %.

4.8. Conclusion

In this work, a novel Laccase-MXene-LIG (L-Ti₃C₂-G) bioelectrodes were fabricated on a polyamide sheet by immobilizing laccase over Ti₃C₂ modified LIG electrode. The resultant bioelectrodes were encased on a 3D printed microfluidic device and the integrated platform was utilized to electroanalytical sense dopamine in clinical and biological samples. When applied in a dopamine biosensor, Ti₃C₂ proved to be an effective matrix for laccase immobilization, providing a biocompatible microfluidic environment without enzyme leaching from the fabricated biosensor with good analytical properties (sensitivity, anti-interfering, reproducibility, and stability) inferring that device has analytical aspects with potential to be used as point-of-care (PoC) applications. The peak current and dopamine concentration were shown to be linearly related using SWV in the linear range of 1 - 10³ nM and obtained limit of detection was 0.47 nM. The sensitivity of the electrode was found to be 6.37 mA.nM⁻¹.cm⁻². This biosensor was precisely used to determine dopamine levels in blood serum and synthetic urine and presented good selectivity towards dopamine. Further, simultaneous detection in the existence of ascorbic acid, L-cysteine, xanthein, uric acid was carried out to prove the selectivity of the platform. MXene configured over LIG provides superior selectivity and specificity with a useful LoD and should be preferable in real-time bio-sensing applications. One common surface modification technique is chemical functionalization, where different chemical compounds are used to modify the surface of the LIG. For example, surface functionalization with organic molecules, such as silanes or self-assembled monolayers (SAMs), can introduce specific functional groups onto the LIG surface, which can enhance its chemical reactivity, wettability, and biocompatibility. In the next chapter, we will explore different surface modification techniques that can be applied to the LIG functionality. This integration allows for real-time monitoring of biological signals, remote data collection, and analysis, enabling faster and more accurate detection of bio-analytes. The synergy of LIG and IoT technology offers promising advancements in real-time bio-sensing applications, paving the way for innovative solutions in healthcare, environmental monitoring, and other fields.

CHAPTER 5:

IoT-ENABLED ELECTROCHEMICAL SENSOR MICROSTRIP

5.1. Introduction:

Accurate detection of triglycerides (fats) in the blood is useful for diagnosing cardiovascular health. This study reports a point-of-care (POC) electrochemical assay that utilizes a smartphone-assisted platform to detect triglycerides. The assay consists of a flexible polyimide-based microstrip with electrodes composed of AuNPs (gold nanoparticles) deposited on laser-induced graphene (LIG). A coating of polydopamine (PDA) on the Au helps to anchor lipase enzymes to the electrode, which results in an enzymatic sensor that is sensitive and specific toward triglycerides. The sensor connects to a smartphone for data acquisition and monitoring, making it IoT-enabled for PoC applications. Since smartphones are ubiquitous, compared to conventional bulky sensors, this approach is more compatible with PoC use. The sensor has a linear response to triglyceride concentration with a limit of detection of 17.89 mg/dL. The apparent Michaelis-Menten constant (K_{appm}) of 21.6 mg/dL indicates that lipase conjugates strongly with triglyceride, resulting in a limit of quantification of 59.63 mg/dL using just 2 μ L of reference triglyceride solution. The validation of the test was also conducted using spiked triglycerides in human serum, wherein the sensor demonstrated a recovery rate of 93.87% for the actual analyte, and the sensor displayed anti-interference capability with other common analytes. The ability to detect triglycerides using a smartphone may lead to improved personalized health monitoring.

Triglyceride is a significant biochemical marker present in the serum of blood that is important biomarker in diagnosing various disorders, including anomalies in lipid metabolism, cardiovascular diseases, atherosclerosis, hypertension [81]. Thus, its accurate and precise measurement has significant therapeutic implications. Concurrently, triglycerides are an important component of the food industry and play a critical role in the production and preservation of many types of food products. Consequently, a sensitive and selective technique of triglyceride assessment is required for health and food monitoring [82].

There are a variety of strategies to measure triglycerides, such as enzyme-linked immunosorbent assay (ELISA) [83], raman spectroscopy [84], and biochemical assays [85]. Among the manifold methods available for triglyceride detection, electrochemical enzymatic biosensors [86] are easy to use, sensitive, specific, and straightforward to implement [87]–[89]. Such assays are also appealing because they fit into a larger trend of diagnostics moving from lab-based to more advanced point-of-care diagnostics with predictive capabilities [90]–[92].

The sensitivity and selectivity of an enzymatic electrochemical biosensor depends on the efficient immobilization of the lipase enzyme on the electrode surface. The lipase enzyme plays a vital role in the enzymatic sensing mechanism by catalyzing the breakdown of triglyceride molecules into glycerol

and fatty acids, while facilitating electron transfer between the active center of the enzyme and the electrode surface. The resulting electrical current is the basis for sensing the triglyceride. One critical factor in executing this mechanism is the appropriate selection of the electrode surface for immobilizing the enzyme.

Electrode selection is another field for research as it has significant impact on the enzyme immobilization. Gold nanoparticles (AuNPs) are attractive as electrodes because they are easy to functionalize and have high surface area. The characteristics of AuNPs make them appropriate for use in enzyme immobilization. Films of AuNPs provide high surface area, yet such film are generally not conductive since the particles lack a percolation path to conduct charge. Thus, the AuNPs should be coated on an underlying electrode. Specifically, AuNPs coated on a laser induced graphene (LIG) electrodes exhibit a low impedance ($\sim 16 \Omega$) [14,15]. LIG is appealing because it is easy to form by simply rastering a laser across certain surfaces, such as polyimide as used here. The use of AuNPs and LIG composite can significantly improve enzymatic adsorption and catalytic performance than bare LIG[16].

One challenge with using such electrodes is formulating AuNPs with long-lasting high catalytic performance [93]. Contamination caused by frequent use [94] and physical, electrical and chemical incompatibility with electrode surfaces limits stability [62], [95]. Therefore, engineering the surface of AuNPs is becoming increasingly important. Coating the surface of AuNPs can shield the AuNP's from exterior factors such as pH of the electrolyte, applied potential, and electrolyte composition. Such factors can alter the surface chemistry of the AuNPs and impact on the stability of the electrode [96]. Coatings can also improve the binding of enzymes to the surface of the Au. Such coatings can help address issues often faced with enzymes, such as denaturation [15], leaching of the enzyme into the sensing solution [16], or decoupling of the enzyme from the electrode that can cause poor electron transfer between the enzymes and electrodes [17,18]. To tackle these challenges, researchers had explored various ways to immobilize enzymes (proteins) to the electrode.

Polydopamine (PDA) is a compelling coating material for immobilization because it adheres readily to many surfaces, including Au. PDA can be formed on a film of AuNPs from a solution of dopamine via oxidative polymerization [97]. PDA has moieties such as amine, imine, and catechol groups that provide conjugate sites for the lipase enzyme. While there are studies on the synthesis of PDA on AuNPs, none have employed it for anchoring enzymes directly on the LIG surface for electrochemical sensors[97], [98]. Prior studies report the benefits of composite electrodes, but the electrodes were prepared in a time consuming, multistep processes [99], [100].

Herein, this work report a simple method to create electrodes for triglyceride sensing. The electrical signal from the sensors can interface with a smartphone app for data acquisition and monitoring. The electrodes have been created by binding enzyme to AuNPs on LIG using PDA. The electrodes exhibit

clinical relevance by demonstrating a LoD value of 17.83 mg/dL with high specificity in blood serum. Moreover, the electrode proved to be reproducible (across 4 devices) and stable without enzyme degradation for up to 6 days. This achievement can be treated as a step toward the development of a portable and accurate platform for triglyceride sensors. This sensor configuration offers versatility for blood serum measurements in clinics and at point-of-care sites, where quick and affordable investigations are prioritized.

5.2. Materials and Method

Lipase and triglyceride were procured from Sigma-Aldrich. Glucose, urea, and uric acid were purchased from Sigma-Aldrich Co., Ltd. All other chemicals used were of analytical grade. Fresh preparation of lipase (2 mg/mL) in phosphate buffer (50 mM, pH 7.4) was carried out before use. Triglyceride solutions (100 mg/dL) prepared in absolute ethanol and stored at 4°C. A range of triglyceride concentrations in 50 mM phosphate buffered solution (PBS, pH 7.0) were prepared by serial dilution.

5.3. Synthesis and fabrication model of the triglyceride biosensor:

Figure 5. 1 represent the mechanism and the various fabrication stages involved in creating the electrodes. A substrate of DuPont-manufactured polyimide (PI) was employed due to its ability to form Laser-Induced Graphene (LIG) upon laser irradiation. The PI substrate, with a thickness of 254 μm , was cut into 30 mm \times 10 mm pieces.

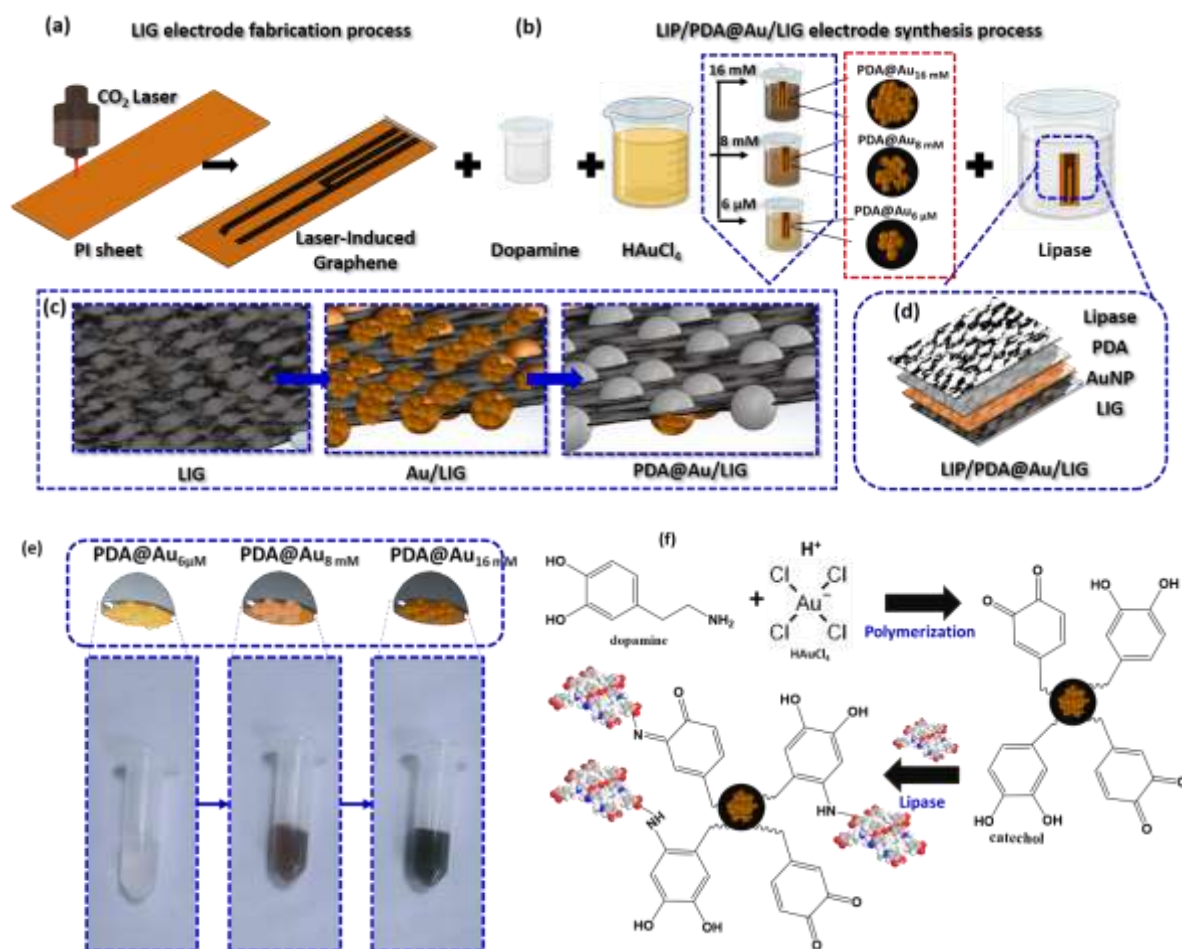


Figure 5. 1: Mechanism and fabrication stages (a) of bare LIG surface (b) LIP/PDA@Au/LIG electrode synthesis process (c) magnified view of synthesized PDA@Au/LIG (d) layer by layer assembly of final LIP/PDA@Au/LIG electrode (e) Accumulated solution image of PDA@Au as a function of Au concentration (f) Schematic for the lipase immobilization process.

Laser engraving of LIG patterns on the PI was carried out using a 50 W CO₂ laser engraver (VLS 3.60 from Universal laser system, AZ, USA), with optimized parameters of 6.5% power and 4.5% speed, PPI 500 in raster mode, as previously reported by our group [7], [37], [101], [102]. The three-electrode design (working electrode, counter electrode, reference electrode) on the PI substrate shown in Figure 5. 1 (a) occupied an area of 20 x 5 mm. AuNPs were then attached to the LIG surface, as represented in Figure 5. 1 (b). The particles were synthesized simultaneously with a PDA coating, which serves multiple purposes, including acting as a reducing agent to convert HAuCl₄ salts into metallic Au, serving as a capping agent for the resulting AuNPs, and ultimately anchoring the enzyme. To synthesize the PDA-coated particles, an aqueous solution of dopamine hydrochloride (2 mg/mL, 0.1 M, pH 8.5) in 0.5 mL tris-HCl buffer solution was used for the formation of the polydopamine solution. To the aforementioned solution, various concentrations of a chloroauric acid solution (HAuCl₄.3H₂O (6 μM, 8 mM, and 16 mM)) were introduced while stirring until the total volume reached 2 mL. The catechol and amine groups on PDA can reduce Au (III) ions to AuNPs. The LIG microstrip was immersed for 4 hr in the aforementioned solution, which resulted in the particles adhering to the LIG. The microstrip resulting from the synthesis process was named PDA@Au/LIG. This synthesis process demonstrated a fascinating phenomenon wherein PDA acted as both a reducing and capping agent for AuNPs, as depicted in Figure 5. 1 (c). The AuNP-synthesized PDAs were denoted as PDA@Au_n, where n is 16 mM, 8 mM, or 6 μM, displaying different aspects of AuNP occupation on the PDA surface, as shown in Figure 5. 1 (d). To attach the enzyme, the microstrips were submerged overnight in a lipase enzyme solution with a concentration of 2 mg/ml in phosphate buffer solution (PBS), resulting in LIP/PDA@Au/LIG. The interaction between the catechol/quinone groups from PDA and the terminal amino or thiol groups of lipase caused a C-N bond and a strong amide bond on the working electrode surface, as shown in Figure 5. 1 (f). When the concentration of HAuCl₄ was as low as 6 μM, limited and larger size AuNPs were embedded inside the PDA coating, designated as PDA@Au_{6 μM}. As the concentration of HAuCl₄ increased to 8 mM, numerous monodisperse AuNPs of small size, known as PDA@Au_{8 mM}, were lodged and dispersed in the PDA shell, as depicted in Figure 5. 1 (d), which was further confirmed through SEM. With a further increase in concentration from 6 μM to 16 mM, AuNPs with broader size distribution and agglomeration were observed, as depicted in Figure 5. 1(d), named PDA@Au_{16 mM}. The accumulation solution color was function of the Au_n concentration showing that the PDA shell had darkly colored, highly concentrated Au ions that mellowed down with decreasing concentration as shown in Figure 5. 1 (e). Au ions mount up at PDA would be lowered by self-reducing agent. Thus, for further experiments PDA@Au_{6 μM} was considered for the sensing of triglyceride as the

maximum surface area was provided by AuNPs with less content of PDA for the immobilization of the lipase.

5.4. Material Characterization

5.4.1. Scanning Electron Microscopy: Impact of HAuCl_4 concentration on PDA coating.

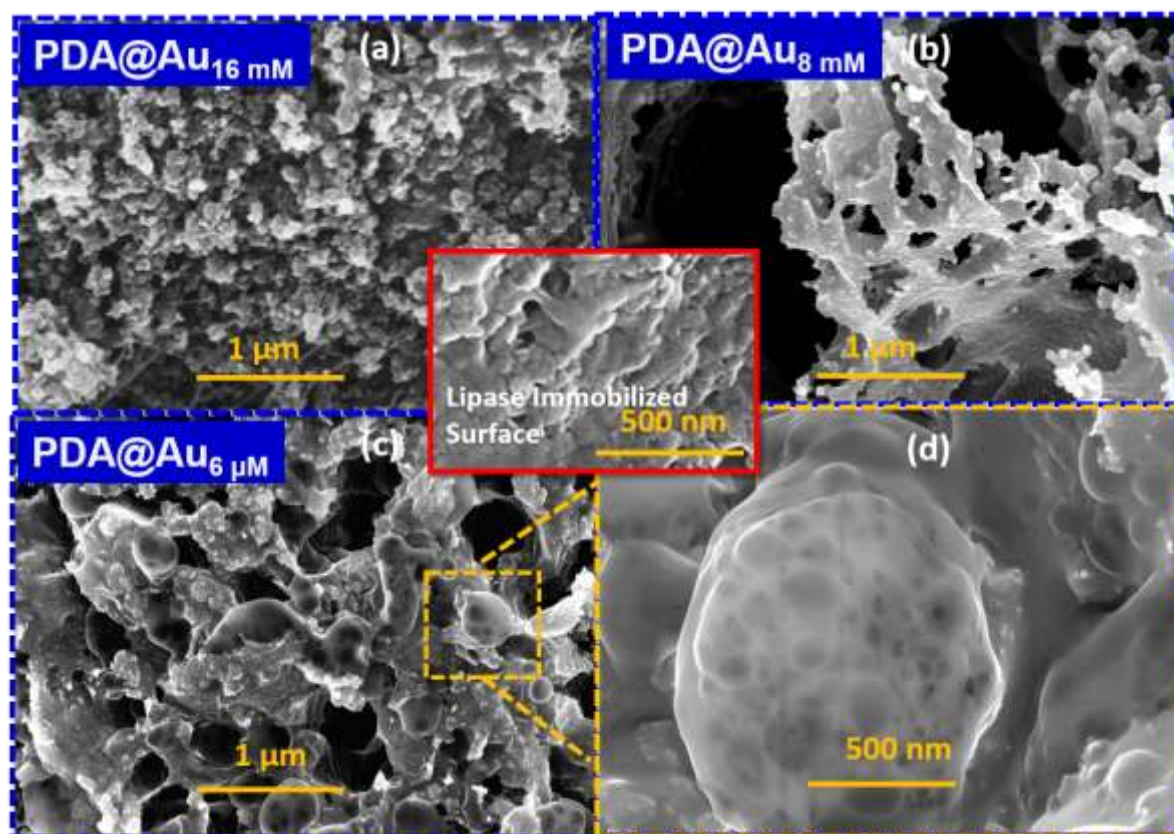


Figure 5. 2: Scanning electron microscopy illustrating the synthesis process of the PDA/Au_n where $n=16 \text{ mM}, 8 \text{ mM}, 6 \mu\text{M}$ (d) magnified view of the lipase immobilization over PDA/Au_{6 μM} the surface

In pursuit of achieving selectivity, we sought to immobilize a lipase enzyme onto a working electrode (WE) and explored the in-situ synthesis of a PDA/Au_n composite with varying concentrations of HAuCl_4 to examine their effects on the size and quantity of AuNPs encapsulated within the PDA shell and the surface morphology of the resulting PDA@Au NPs film on the LIG microstrip using scanning electron microscopy (SEM), as depicted in Figure 2. The enzyme helps to hydrolyze the triglycerides into fatty acid and glycerol as a by-product [102], [103]. It was found that synthesized AuNPs can demonstrate three manifold aspects for their occupation within the PDA corresponding to the concentration of HAuCl_4 that contributed to the reaction. The study investigated impact of varying the concentration of HAuCl_4 affected the quantity and size of AuNPs enclosed by the PDA shell. In addition, the surface structure of the LIP/PDA@Au NPs film on the LIG microstrip was examined using scanning electron microscopy (SEM), as depicted in inset of Figure 5. 2 (d). Also to better understand

how the concentration of Au_n impacts the immobilization efficiency and the morphology of microstrips were compared on the different Au_n concentrations. When the concentration of $HAuCl_4$ was significantly low, the synthesis of PDA coating on the surface of AuNPs was consistently observed as in the case of $PDA@Au_{6\mu M}$ and this was confirmed with the EDAX analysis which shows least 1.22 at. wt % of Cl as compared to the $PDA@Au_{16\text{ mM}}$ and $PDA@Au_{8\text{ mM}}$ which was 0.80 and 0.75 at. wt %. The PDA coating served to regulate the growth of AuNPs on the surface of LIG, as depicted in Figure 5.2 (a and b). Upon increasing the concentration of $HAuCl_4$ to 8 mM, an ample amount of monodisperse AuNPs of smaller size were observed with a PDA shell on LIG surface, as shown in Figure 5.2 (b). Further increases in $HAuCl_4$ concentration, from 6 μM to 16 mM, led to the detection of AuNPs with a wide size distribution and agglomeration, as demonstrated in Figure 5.2 (a). At a concentration of 6 μM , small and evenly dispersed AuNPs were synthesized due to the strong binding activity of PDA with the AuNPs, which effectively inhibited the growth of AuNPs and provided a sufficient surface area for immobilization. This immobilization was advantageous, as the stabilizing interactions between Au and PDA in the inner shell were stronger than those on the surface, owing to the higher abundance of functional groups present in the inner shell[86].

5.4.2. Fourier transforms infrared spectroscopy

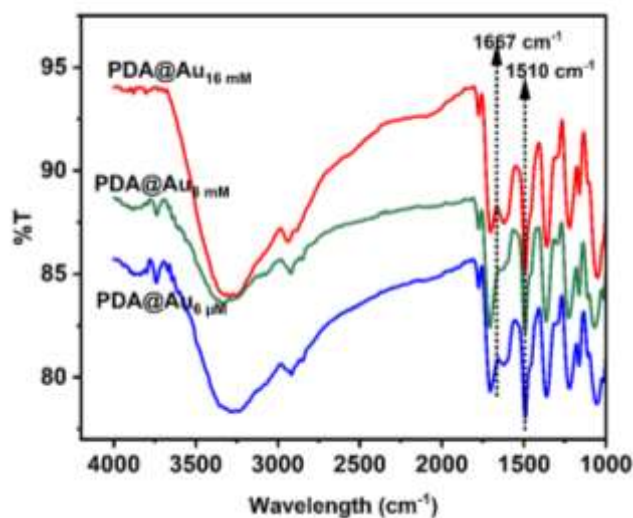


Figure 5.3 Fourier transforms infrared spectroscopy (FTIR) spectra of PDA/Aun $n=16\text{ mM}$, 8 mM , $6\ \mu M$.

To investigate the PDA synthesis in the process of in situ growth with the aid of Au_n solution, after 4 hours. reaction was polymerized and examined by the FTIR as shown in Figure 5.3, which confirmed that the Au concentration had an impact on the in-situ PDA synthesis. The unreacted dopamine was in the range of $3000\text{-}3400\text{ cm}^{-1}$ while spectra for synthesized PDA were found in the range of $1500\text{-}1700\text{ cm}^{-1}$. These spectra were ascribed to the stretching vibration of the phenolic O-H and N-H groups. As polymerization of the dopamine was initiated, one of the two bands (in the range $3000\text{ to }3400\text{ cm}^{-1}$)

disappeared because of the transformation of the primary amine into the secondary or tertiary amine. The reduction in the transmittance intensity of the distinctive peaks implies the appreciable in situ PDA synthesis in the polymerized solution as shown in Figure 5. 3. After the successful synthesis of PDA, indole, and indoline formation appeared through the spectra 1500 to 1660 cm^{-1} which was formed through the intramolecular cyclization reaction of dopamine [81].

5.4.3. UV-Vis Spectroscopy

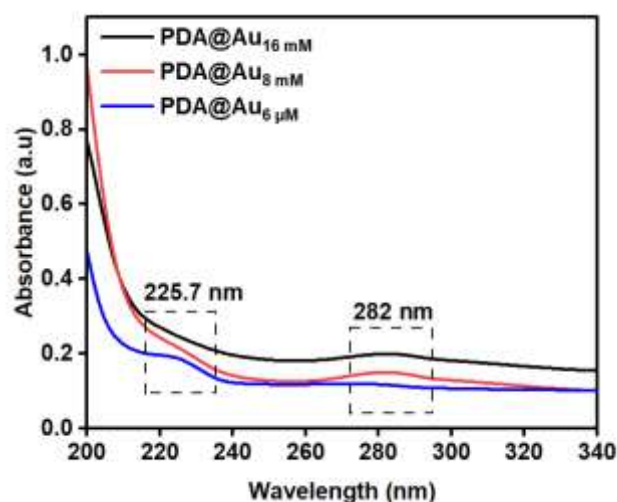


Figure 5. 4 UV-Vis absorption spectra of the PDA@Au $n=16 \text{ mM}$, 8 mM , $6 \mu\text{M}$ as a function of the increasing concentration of the Au.

From Figure 5. 4, it can be revealed that due to the presence of the quinone moiety, absorption at 282 nm was seen and absorption at 225.7 nm was acquired due to intramolecular charge transfer. It was observed that a decrease in the absorbance at 282 nm as the concentration of PDA@Au was reduced from 16 mM to 8 mM. This decrease in absorbance was attributed to the reduction of quinone to hydroquinone, which suggests that the PDA coating on the Au NPs was acting as a reducing agent. Quinones and amines were formed in the UV-Vis spectrum between 200 and 320 nm, which was associated with the subsequent oxidation and polymerization of those molecules to produce PDA. As a result, in this work, the absorbance at 282 nm was used to assess the development of PDA [82]. As per the Schiff base formation mechanism, subsequent to the synthesis of the PDA coating onto the Au particles surface, the residual quinones groups, which remained after the reduction process involving Au as illustrated in Figure 5. 3, are expected to undergo nucleophilic reactions with the aid of covalent immobilization [84]. In this work, the quinone group at the PDA surface and thiol or amino group of the lipase enzyme assist the immobilization of the enzyme over the surface of the LIG by exposing the PDA@Au surface to the lipase enzyme solution [84]. The SEM image confirms the immobilization of the lipase over the surface of the LIG in the above section in the inset of Figure 5. 2 (d).

5.5. Result and Discussion:

5.5.1. Data acquisition and monitoring on smartphone:

The LIP/PDA@Au/LIG microstrip was integrated with a portable potentiostat (Sensit Smart from palmsense) for on-site triglyceride sample analysis. Figure 5. 5 shown the complete setup including an Android smartphone with an accompanying app. The potentiostat was connected to a single board computer running Raspberry Pi OS help to compensate two significant parts of the system. A cloud-based IoT MQTT Broker (called ThingSpeak) was used to store, retrieve, and transmit data to and from the sensing platform utilizing the HTTP and MQTT protocols. The need for different protocols was to tackle the asynchronous operation of the sensing platform. In the MQTT model, the ThingSpeak service was the broker, and the Raspberry Pi was the client. The data on the ThingSpeak service can also be stored and retrieved using HTTP requests. MethodSCRIPT language was used to communicate with the potentiostat by the Raspberry Pi. It aids in adjusting the measurement parameters as required and fetching the results from the potentiostat. The asynchronous operation was achieved using MQTT, as the client gets the payload without frequent polling.

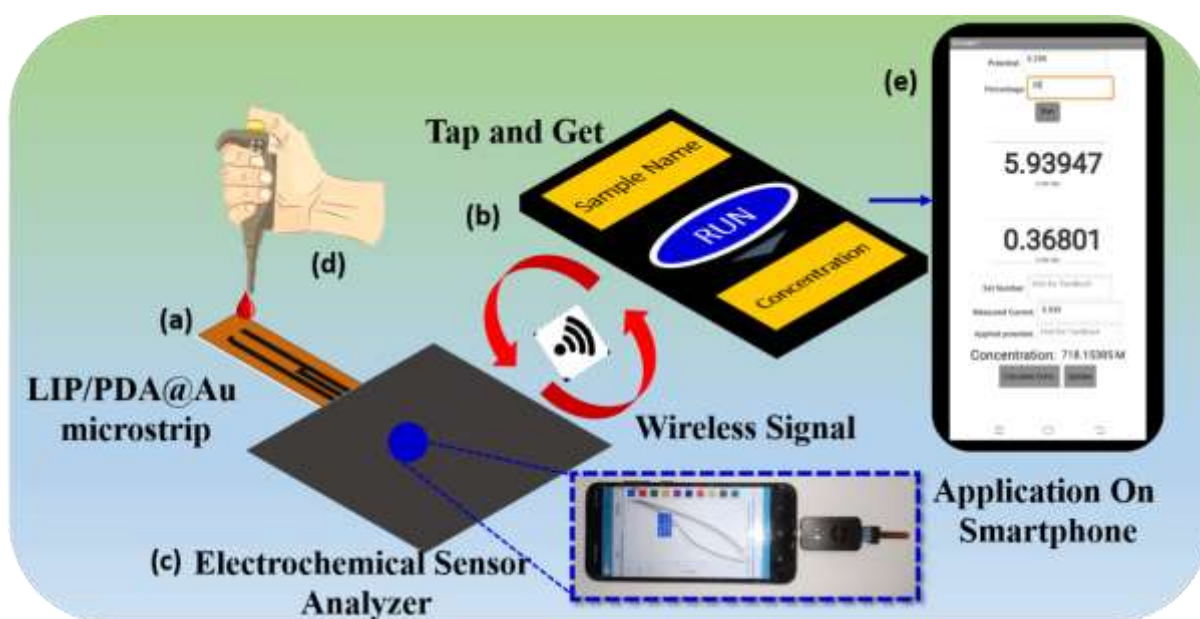


Figure 5. 5: (a) LIP/PDA@Au/LIG microstrip inserted to the electrochemical analyzer with selected cyclic voltammetry mode (b) Smartphone is tapped on the application to receive data (c) Electrochemical analyzer receive power from smartphone; (d) sample drop on the detection zone (e) Receive signal display as concentration on smartphone application.

The program retrieves the potentiostat data in real-time, parses, processes the output data and stores results as ".CSV" files which may be uploaded to the cloud. The necessary data points are stored on the ThingSpeak cloud, and the Android application displays the results of the most recent response on the

smartphone screen. The current measurement from the sample can be turned into a concentration level using a standard calibration curve built into the Android application.

5.5.2. Electrochemical response studies and response of LIP/PDA@Au/LIG microstrips and Hanes plot for effect of enzyme activity:

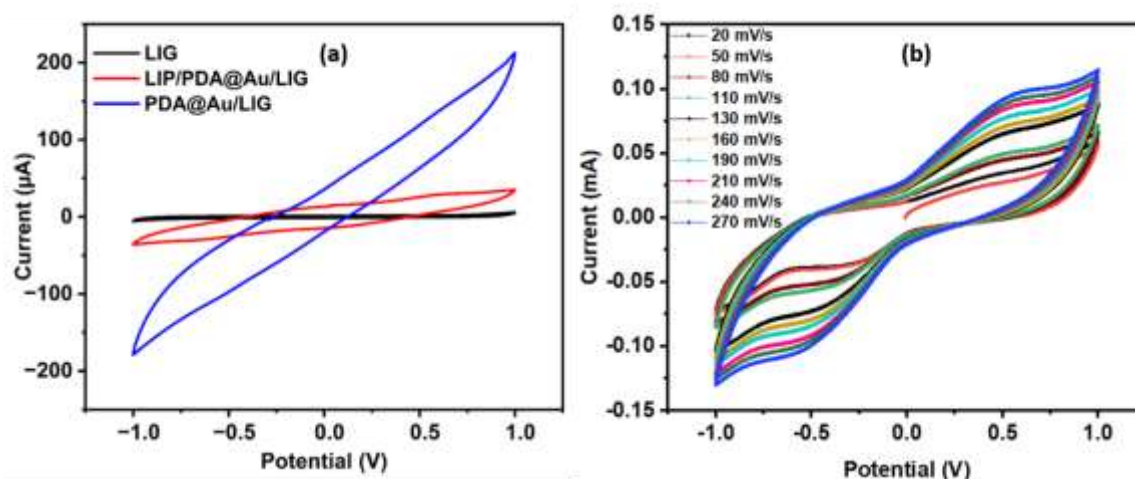


Figure 5. 6 Cyclic voltammetry of (a) LIG, PDA@Au/LIG, and LIP/PDA@Au/LIG microstrip in PBS (50 mM, pH 7.0) at the scan rate of 20 mV/s (b) Scan rate analysis of PDA@Au/LIG with a scan rate of 20 mV/s to 280 mV/s.

Cyclic voltammetry (CV) of bare LIG, modified with in situ PDA and lipase immobilized microstrips were monitored, and changes in their electrochemical behavior were found at different steps of microstrip modification. The electrochemical behavior of all microstrip was investigated through the CV in a deaerated PBS with no significant redox peak observed. These electrochemical studies are shown in Figure 5. 6 (a) of the PDA@Au//LIG microstrip and LIP/PDA@Au/LIG microstrip carried out in 50 mM of PBS (pH 7.0, 0.9% NaCl) including 5 mM $[\text{Fe}(\text{CN})_6]^{3-/4-}$ at a scan rate of 20 mV/s. As magnitude of the current response of the PDA@Au/LIG microstrip was higher than that of the bare LIG microstrip revealing that PDA has increased the electroactive surface of the microstrip resulting in enhanced electron transport between triglyceride and the microstrip surface. However, the magnitude of the current response decreased after the immobilization of the lipase enzyme onto the PDA@Au//LIG microstrip as a cause of isolating properties of the lipase [102]. To study electrode reaction mechanism, Figure 5. 6 (b) exhibits the CV for the LIP/PDA@Au/LIG microstrip as a function of scan rate from 20 to 280 mV/s. As the anodic and cathodic peak current magnitude increases linearly with the scan rate which follows the diffusion-controlled mechanism. It revealed that the electron transfer between lipase and PDA microstrip could be easily performed at the LIP/PDA@Au/LIG film and it was a diffusion-controlled process, not a surface-controlled process as concluded from the calibration plot shown in the Figure 5. 7 (c). The regression coefficients for cathodic and anodic peaks were 0.9360 and 0.988, respectively. The cathodic equation is represented as,

$$I_{pa} \text{ (}\mu\text{A)} \text{ (LIP/PDA@Au/LIG)} = 6.49 \times 10^{-3} \text{ mA (s/mV)} \times v^{1/2} \text{ (mV/s)} + 0.092 \text{ (mA)};$$

$$R = 0.93; \text{SD} = 0.03$$

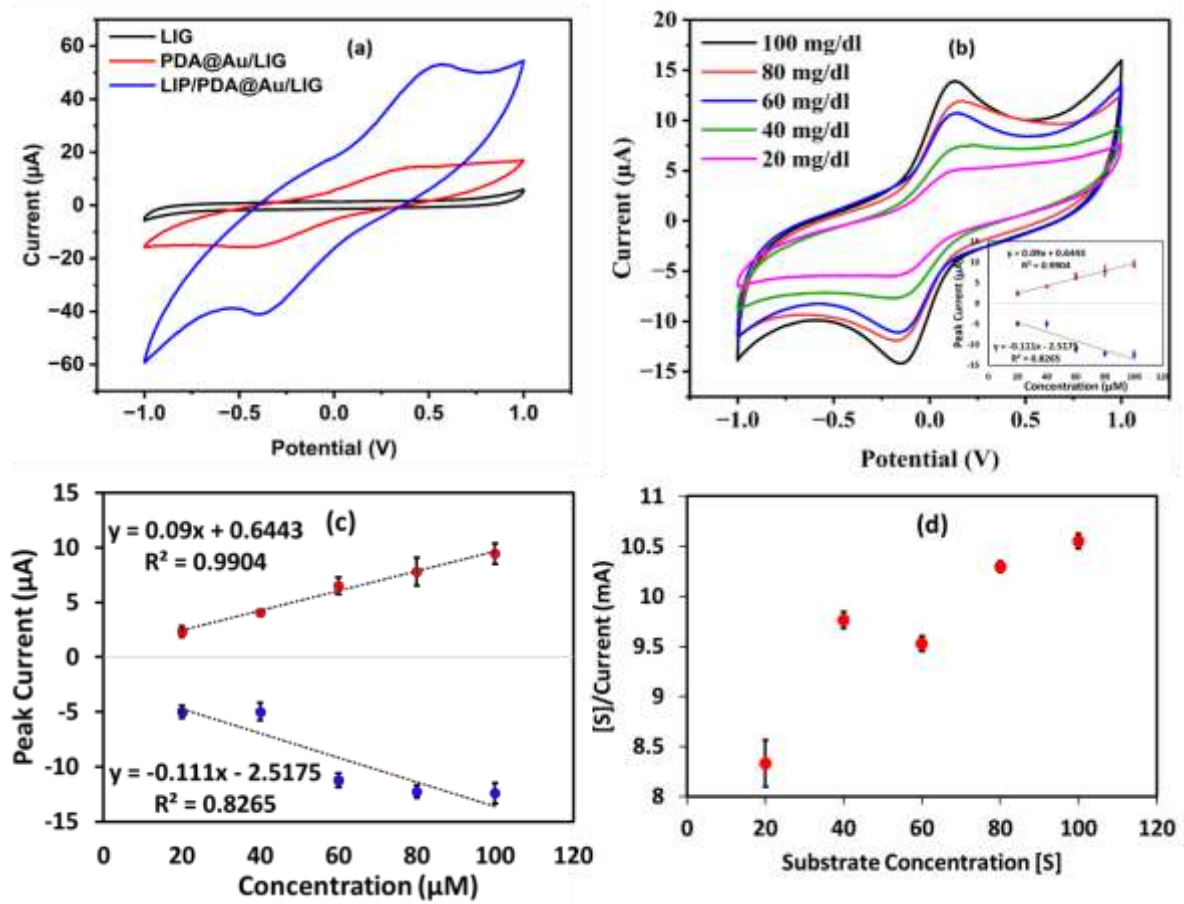


Figure 5. 7: Cyclic voltammetry of (a) LIG, PDA@Au/LIG, and LIP/PDA@Au/LIG microstrip in 200 mg/dL triglyceride at the scan rate of 20 mV/s (b) Concentration analysis varies from 20 mg/dl to 100 mg/dl with the scan rate of 20 mV/s (c) Calibration plot for concentration of 20 mg/dl to 100 mg/dl. (d) Study of Hanes plot for the concentration of substrate [S] and [S]/current in mA.

Further, the redox peak was observed in the PBS containing 200 mg/dL triglyceride solution with the redox mediator $K_3Fe(CN)_6$. The electrochemical response of LIP/PDA@Au/LIG lead to increase in the current response for the 200 mg/dL triglyceride at the scan rate of 20 mV/s than the other microstrips like PDA@Au/LIG and LIG shown in Figure 5. 7 (a). The EC response of the LIP/PDA@Au/LIG was studied as function of triglyceride concentrations varying from 20 mg/dL to 100 mg/dL using the CV technique shown in Figure 5. 7 (b) at a 20 mV/s of scan rate in deaerated PBS of 50 mM, (pH 7.2) which falls under the clinically found normal human range of (20 mg/dL to 400 mg/dL). The calibration plot obtained from the concentration study reveals the linearity of the sensor with the coefficient of the regression as 0.9904 for anodic peak current with the LoD and LoQ of 17.89 mg/dL and 59.63 mg/dL ($LoD = \frac{3\sigma}{Sensitivity}$ and $LoQ = \frac{10\sigma}{Sensitivity}$) respectively. The sensitivity of the sensor was calculated to

be $0.25 \mu\text{A}/\text{cm}^2/\text{mg}/\text{dL}$ from the slope value of the calibration plot in Figure 5.7(c). The sensitivity of the sensor relies on the enzyme and substrate kinetics characteristics and it was observed from the Hanes plot as shown in Figure 5.7(d). According to the Hanes plot, the apparent Michaelis-Menten constant ($K_{\text{app m}}$) for the LIP/PDA@Au/LIG microstrip was obtained to be $21.6 \text{ mg}/\text{dL}$. The low value of $K_{\text{app m}}$ indicates enhanced affinity of lipase from the *C. rugosa* towards triglyceride which is an efficient value in the case of the enzymatic triglyceride sensing which is much smaller than the reported articles [102], [104]. The lower $K_{\text{app m}}$ value specifies *C. rugosa* shows appropriate affinity of lipase toward triglyceride.

5.5.3. Anti-interference and Reproducibility of lipase/PDA@Au/LIG microstrip

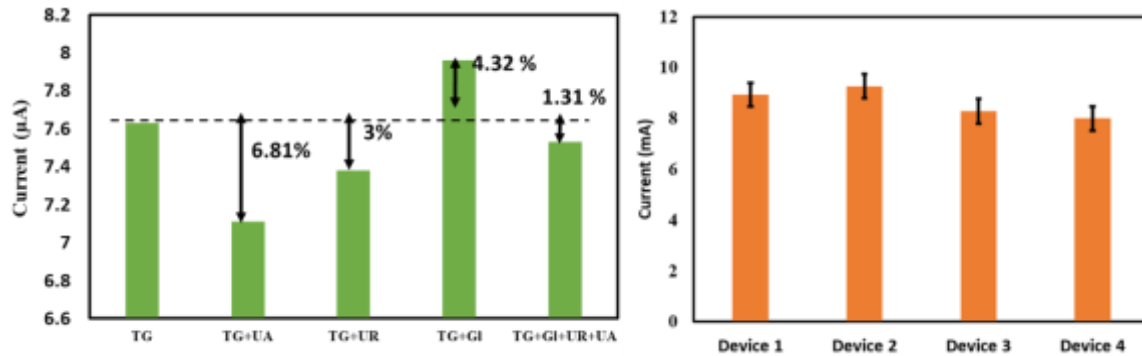


Figure 5.8: (a) Anti-interference plot for the triglyceride with interferent of UA, UR, Gl, and all composition in TG (b) Reproducibility analysis for the four devices.

*UA: uric acid, UR: urea, Gl: Glucose, TG: Triglyceride

To validate the effect of possible interferents on the current response obtained from the device, a CV test was carried out in a controlled environment. This process helps to ensure the accuracy of the results by identifying any potential sources of interference that could impact the device performance. Figure 5.8(a) demonstrate the effect of the change in peak current response with individual analyte concentration of triglyceride in a 1:1 ratio. The bar diagram shows the interference percentage for various interferents and was calculated as follows:

$$\% \text{Interference} = \frac{\Delta \text{Current}_{\text{TG}} - \Delta \text{Current}_{\text{Interferent}}}{\Delta \text{Current}_{\text{TG}}}$$

where $\Delta \text{Current}_{\text{TG}}$ is the current change obtained for triglyceride concentration if compared with current acquired for $0 \text{ mg}/\text{dL}$ triglyceride and $\Delta \text{Current}_{\text{Interferent}}$ is the current change resembling to the mixture of triglyceride also with interferents in a 1:1 ratio. The horizontal line intersecting the Y axis shows % interference with particular interferent as UA (0.2 mM), UR (1 mM), Gl (5 mM), and TG ($100 \text{ mg}/\text{dL}$). This reveals a maximum of 6.81 % interference due to UA which help to evaluate the specificity of the LIP/PDA@Au/LIG microstrip and had strong anti-interferent (Note: Concentration conversion factor for the TG is $100 \text{ mg}/\text{dL} = 1.13 \text{ mM}$). The reproducibility of the sensor was evaluated

by performing four trials with freshly coated LIP/PDA@Au/LIG microstrip for the detection of triglyceride. Figure 5. 8 (b) illustrates the current response with four devices with less than a 5 % standard deviation confirming the reproducibility of the sensor. The relative standard deviation for the measured values was 0.53 which is within the permissible limits. These data reveal the consistency and accuracy of the developed biosensor.

5.5.4. Determination of triglycerides in human serum sample

Subsequently, experiment was conducted in the human blood serum to perform real sample analysis. For this, 500 μ L blood serum and 2 mg lipase enzyme were incubated at 35°C to hydrolyze the intrinsic triglyceride in blood serum and sample was diluted 50 times in PBS (50 mM, pH). The protein was separated from the mixture through centrifugation at a speed of 12000 rpm to avoid the interference with subsequent analysis. Serum triglyceride concentration was spiked from 50 mg/dL to 100 mg/dL. At a peak potential of 0.47 V, the obtained current was recorded and its concentration in human serum was calculated using the calibration curve. The, this value was compared with the significantly elevated amounts in the spiked samples, as shown in Table 5.1.

Table 5. 1 Response of triglyceride assay and recovery analysis of blood serum samples

Sr.No.	Triglyceride Concentration Spiked (mg/dL)	Triglyceride Concentration Found (mg/dL)	Standard Deviation	Recovery (%R)
1	50	56.23	0.027	93.71
2	80	70.26	0.036	87.82
3	100	93.89	0.156	93.89

Thus, the present portable triglyceride sensor provides adequate sensitivity for the TG in the human blood serum.

5.6. Conclusion

In this work, a simple yet efficient, low-cost, in situ synthesis approach has been established to fabricate an extremely sensitive PDA@Au microstrip. This novel sensor featured a sensitivity of 0.25 μ A.cm⁻²/mg/dL, a fast response time of less than 17 ms. With this sensor, triglyceride with an LoD of 17.83 mg/dL and anti-interference capability with co-analytes have been detected. These attributes enable to monitor real-time signals from blood serum. It is noteworthy that the complete device fabrication technique can be scaled up without the use of complicated or expensive machinery. This technique offers a new path to affordable biosensors with the possibility for simple integration into future biomedical and electronics, like flexible reusable chips and human-machine interfaces.

CHAPTER 6: CONCLUSION AND FUTURE SCOPE

This thesis encompasses the advancement of various microfluidic technologies that facilitate electrochemical-based research and diagnostics. The focal points of this research were the development of an integrated system for sensing fluids in small volume, as well as electrochemical sensors for quantifying biomarkers. Detailed methodologies for fabricating and validating these technologies were presented, with a primary emphasis on sustainability and affordability throughout the value chain, encompassing both the process and final product. The summary of the outcomes of this thesis is illustrated in the accompanying flowchart.

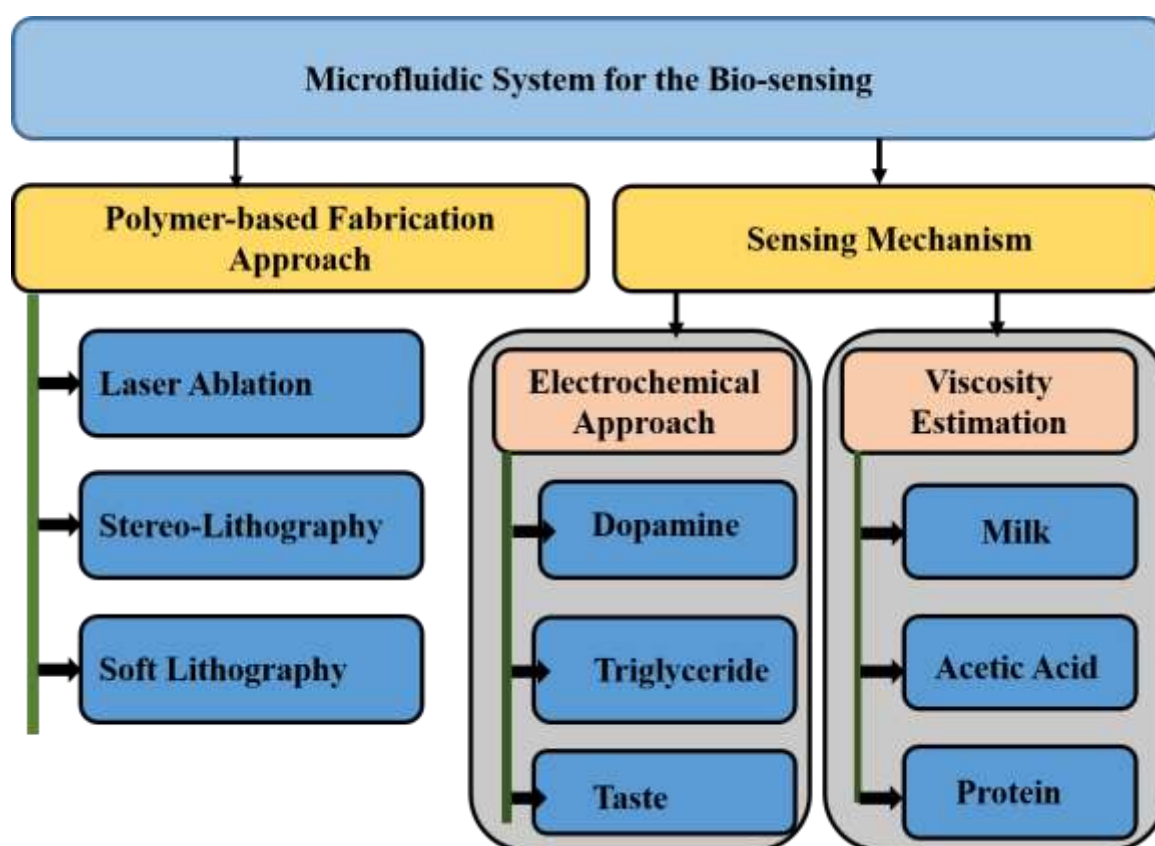


Figure 6. 1: Summary of the outcomes of this thesis is illustrated in the accompanying flowchart

6.1. Major Outcomes:

- The research utilized techniques such as electrochemical and viscosity measurement method with a primary focus on electrode fabrication, surface modification, and integration with microfluidics platforms.
- The validation of automated electro-microfluidic viscometer in the Newtonian fluid was conducted with the least variation in viscosity as compare to the conventional viscometer.
- The validation of miniaturized electro-analytical sensors in buffer solutions was conducted, successfully detecting various biochemical such as dopamine, ascorbic acid, uric acid, L-Cysteine as well as xanthine.
- The sensors were also evaluated for susceptibility to interference from blood chemicals, with no observed interference. Furthermore, the sensors were applied to real sample analysis using bodily fluids like serum and urine, and results were compared with commercially available assay kits.
- The developed miniaturized electro-analytical platforms exhibited potential applications in point-of-care diagnostics for healthcare management.

6.2. Limitations and Future Scope

- The sensitivity, selectivity, and specificity of POCT have significantly improved over time. One potential way to integrate POCT into healthcare diagnostics is through wearable handheld devices enabled with Wi-Fi. The combination of POCT with complementary technologies such as microfluidics, IoT, machine learning, and EC techniques can aid in the prediction of digital healthcare consultations.
- There are numerous multidisciplinary challenges that need to be overcome to optimize protocols for e-health. These challenges encompass the integration of big data analysis into diagnosis, which necessitates further exploration of machine learning, data mining, and visualization tools.
- Ensuring the security of patient data while providing health status insights is a critical factor. An ongoing challenge in sensor development is the identification of new electrode materials and device fabrication techniques that are reusable, disposable, affordable, and environmentally friendly. The integration of electrochemical methods with microfluidics offers the potential for new functionalities without compromising integrity or miniaturization.
- Incorporating automation in microfluidics can substantially enhance the efficiency, precision, and reproducibility of experiments. Here is a more comprehensive explanation of how to incorporate automation into your microfluidic research:

- **Syringe Pumps:** Syringe pumps are frequently used in microfluidics to control the flow rate of fluids within microchannel. These pumps automate the process of starting and withdrawing fluids from microfluidic devices. Researcher can program syringe pumps to deliver precise flow rates and patterns, building it easier to conduct experiments that necessitate constant flow, pulsatile flow, or specific gradients.
- **Microcontrollers and Programmable Logic Controllers (PLCs):** These devices allow researchers to automate various aspects of experiments. Researcher can use microcontrollers or PLCs to control valves, pumps, and other components of your microfluidic setup. This automation can help in executing complex protocols with precise timing and coordination.
- **Remote Operation:** In some cases, researcher may want to operate microfluidic experiments remotely, which is especially valuable for experiments conducted in isolated environments or when conducting long-term studies. Automation can enable remote monitoring and control of that setup.

REFERENCE

- [1] R. Ahmad, M. Khan, P. Mishra, ... N. J.-J. of the, and undefined 2021, "Engineered hierarchical CuO nanoleaves based electrochemical nonenzymatic biosensor for glucose detection," *iopscience.iop.org*, vol. 168, no. 1, p. 017501, Jan. 2021, doi: 10.1149/1945-7111/abd515.
- [2] A. Khosla *et al.*, "Carbon fiber doped thermosetting elastomer for flexible sensors: physical properties and microfabrication," *Springer*, vol. 8, no. 1, p. 12313, Dec. 2018, doi: 10.1038/s41598-018-30846-3.
- [3] M. Mauk *et al.*, "Miniaturized devices for point of care molecular detection of HIV," *Lab Chip*, vol. 17, no. 3, pp. 382–394, Jan. 2017, doi: 10.1039/C6LC01239F.
- [4] R. Khnouf, D. Karasneh, E. Abdulhay, A. Abdelhay, W. Sheng, and & Z. Hugh Fan, "Microfluidics-based device for the measurement of blood viscosity and its modeling based on shear rate, temperature, and heparin concentration", doi: 10.1007/s10544-019-0426-5.
- [5] A. Kaushik, R. Khan, P. Solanki, S. Gandhi, H. Gohel, and Y. K. Mishra, "From Nanosystems to a Biosensing Prototype for an Efficient Diagnostic: A Special Issue in Honor of Professor Bansi D. Malhotra," *Biosens. 2021, Vol. 11, Page 359*, vol. 11, no. 10, p. 359, Sep. 2021, doi: 10.3390/BIOS11100359.
- [6] P. R. Solanki, C. Dhand, A. Kaushik, A. A. Ansari, K. N. Sood, and B. D. Malhotra, "Nanostructured cerium oxide film for triglyceride sensor," *Sensors Actuators B Chem.*, vol. 141, no. 2, pp. 551–556, Sep. 2009, doi: 10.1016/J.SNB.2009.05.034.
- [7] M. D. Wagh, S. K. Sahoo, and S. Goel, "Laser-induced graphene ablated polymeric microfluidic device with interdigital electrodes for taste sensing application," *Sensors Actuators A Phys.*, vol. 333, p. 113301, Jan. 2022, doi: 10.1016/J.SNA.2021.113301.
- [8] S. N. Prabhu, S. C. Mukhopadhyay, C. Gooneratne, A. S. Davidson, and G. Liu, "Interdigital sensing system for detection of levels of creatinine from the samples," *Proc. Int. Conf. Sens. Technol. ICST*, vol. 2019-December, Dec. 2019, doi: 10.1109/ICST46873.2019.9047672.
- [9] P. Rewatkar, A. Kothuru, and S. Goel, "PDMS-Based Microfluidic Glucose Biofuel Cell Integrated with Optimized Laser-Induced Flexible Graphene Bioelectrodes," *IEEE Trans. Electron Devices*, vol. 67, no. 4, pp. 1832–1838, Apr. 2020, doi: 10.1109/TED.2020.2971480.
- [10] A. Nag, S. C. Mukhopadhyay, and J. Kosel, "Tactile sensing from laser-ablated metallized PET films," *IEEE Sens. J.*, vol. 17, no. 1, pp. 7–13, 2016.
- [11] A. Gao *et al.*, "Silicon-nanowire-based CMOS-compatible field-effect transistor nanosensors for ultrasensitive electrical detection of nucleic acids," *Nano Lett.*, vol. 11, no. 9, pp. 3974–3978,

- 2011.
- [12] M. R. Bobinger *et al.*, “Flexible and robust laser-induced graphene heaters photothermally scribed on bare polyimide substrates,” 2018, doi: 10.1016/j.carbon.2018.12.010.
- [13] L. Martynova, L. E. Locascio, M. Gaitan, G. W. Kramer, R. G. Christensen, and W. A. MacCrehan, “Fabrication of Plastic Microfluid Channels by Imprinting Methods,” *Anal. Chem.*, vol. 69, no. 23, pp. 4783–4789, Dec. 1997, doi: 10.1021/AC970558Y/ASSET/IMAGES/LARGE/AC970558YF00008.JPEG.
- [14] J. Xu, L. Locascio, M. Gaitan, and C. S. Lee, “Room-temperature imprinting method for plastic microchannel fabrication,” *Anal. Chem.*, vol. 72, no. 8, pp. 1930–1933, Apr. 2000, doi: 10.1021/AC991216Q/ASSET/IMAGES/LARGE/AC991216QF00005.JPEG.
- [15] J. Lin *et al.*, “Laser-induced porous graphene films from commercial polymers,” *Nat. Commun.*, vol. 5, pp. 5–12, 2014, doi: 10.1038/ncomms6714.
- [16] J. L. Erkal *et al.*, “3D printed microfluidic devices with integrated versatile and reusable electrodes,” *Lab Chip*, vol. 14, no. 12, pp. 2023–2032, May 2014, doi: 10.1039/C4LC00171K.
- [17] Y. Nakajima *et al.*, “Femtosecond-laser-based fabrication of metal/PDMS composite microstructures for mechanical force sensing,” *Opt. Mater. Express*, vol. 7, no. 11, pp. 4203–4213, 2017.
- [18] M. F. El-Kady, V. Strong, S. Dubin, and R. B. Kaner, “Laser scribing of high-performance and flexible graphene-based electrochemical capacitors,” *Science (80-.)*, vol. 335, no. 6074, pp. 1326–1330, 2012, doi: 10.1126/science.1216744.
- [19] P. F. O’Neill *et al.*, “Advances in three-dimensional rapid prototyping of microfluidic devices for biological applications,” *Biomicrofluidics*, vol. 8, no. 5, p. 052112, Oct. 2014, doi: 10.1063/1.4898632.
- [20] L. Chen, C. Zhang, and D. Xing, “Paper-based bipolar electrode-electrochemiluminescence (BPE-ECL) device with battery energy supply and smartphone read-out: A handheld ECL system for biochemical analysis at the point-of-care level,” *Sensors Actuators B Chem.*, vol. 237, pp. 308–317, Dec. 2016, doi: 10.1016/J.SNB.2016.06.105.
- [21] S. B. Puneeth and S. Goel, “Handheld and ‘Turnkey’ 3D printed paper-microfluidic viscometer with on-board microcontroller for smartphone based biosensing applications,” *Anal. Chim. Acta*, vol. 1153, p. 338303, Apr. 2021, doi: 10.1016/j.aca.2021.338303.
- [22] A. Mustafa *et al.*, “A micropillar-based microfluidic viscometer for Newtonian and non-Newtonian fluids,” *Anal. Chim. Acta*, vol. 1135, pp. 107–115, 2020, doi:

- 10.1016/j.aca.2020.07.039.
- [23] S. B. Puneeth, N. Munigela, S. A. Puranam, and S. Goel, “Automated Mini-Platform with 3-D Printed Paper Microstrips for Image Processing-Based Viscosity Measurement of Biological Samples,” *IEEE Trans. Electron Devices*, vol. 67, no. 6, pp. 2559–2565, Jun. 2020, doi: 10.1109/TED.2020.2989727.
- [24] M. Younas *et al.*, “Parametric analysis of wax printing technique for fabricating microfluidic paper-based analytic devices (μ PAD) for milk adulteration analysis,” *Microfluid. Nanofluidics*, vol. 23, no. 3, p. 38, Mar. 2019, doi: 10.1007/s10404-019-2208-z.
- [25] D. E. Solomon, A. Abdel-Raziq, and S. A. Vanapalli, “A stress-controlled microfluidic shear viscometer based on smartphone imaging,” *Rheol. Acta*, vol. 55, no. 9, pp. 727–738, Sep. 2016, doi: 10.1007/s00397-016-0940-9.
- [26] D. E. Solomon and S. A. Vanapalli, “Multiplexed microfluidic viscometer for high-throughput complex fluid rheology,” *Microfluid. Nanofluidics*, vol. 16, no. 4, pp. 677–690, 2014, doi: 10.1007/s10404-013-1261-2.
- [27] H. A. Stone, *Stone2007*.
- [28] S. H. Maron, I. M. Krieger, and A. W. Sisko, “A capillary viscometer with continuously varying pressure head,” *J. Appl. Phys.*, vol. 25, no. 8, pp. 971–976, Aug. 1954, doi: 10.1063/1.1721811.
- [29] A. Kothuru, C. Hanumanth Rao, S. B. Puneeth, M. Salve, K. Amreen, and S. Goel, “Laser-Induced Flexible Electronics (LIFE) for Resistive, Capacitive and Electrochemical Sensing Applications,” *IEEE Sens. J.*, vol. 20, no. 13, pp. 7392–7399, Jul. 2020, doi: 10.1109/JSEN.2020.2977694.
- [30] Z. Han, X. Tang, and B. Zheng, “A PDMS viscometer for microliter Newtonian fluid,” in *Journal of Micromechanics and Microengineering*, Sep. 2007, vol. 17, no. 9, pp. 1828–1834. doi: 10.1088/0960-1317/17/9/011.
- [31] K. Dutkowski, “Experimental investigations of Poiseuille number laminar flow of water and air in minichannels,” *Int. J. Heat Mass Transf.*, vol. 51, no. 25–26, pp. 5983–5990, Dec. 2008, doi: 10.1016/j.ijheatmasstransfer.2008.04.070.
- [32] G. Türkakar and T. Okutucu-Özyurt, “Dimensional optimization of microchannel heat sinks with multiple heat sources,” in *International Journal of Thermal Sciences*, Dec. 2012, vol. 62, pp. 85–92. doi: 10.1016/j.ijthermalsci.2011.12.015.
- [33] M. A. Nour, S. M. Khan, N. Qaiser, S. A. Bunaiyan, and M. M. Hussain, “Mechanically flexible viscosity sensor for <sc>real-time</sc> monitoring of tubular architectures for industrial

- applications,” *Eng. Reports*, vol. 3, no. 3, p. e12315, Mar. 2021, doi: 10.1002/eng2.12315.
- [34] T. Xu *et al.*, “A high sensitive pressure sensor with the novel bossed diaphragm combined with peninsula-island structure,” *Sensors Actuators, A Phys.*, vol. 244, pp. 66–76, Jun. 2016, doi: 10.1016/j.sna.2016.04.027.
- [35] M. Shaker, E. Sundfor, G. Farine, C. Slater, P. A. Farine, and D. Briand, “Design and Optimization of a Low Power and Fast Response Viscometer Used for Determination of the Natural Gas Wobbe Index,” *IEEE Sens. J.*, vol. 19, no. 23, pp. 10999–11006, Dec. 2019, doi: 10.1109/JSEN.2019.2928479.
- [36] A. V. Mamishev, Y. Du, B. C. Lesieutre, and M. Zahn, “Development and applications of fringing electric field dielectrometry sensors and parameter estimation algorithms,” *J. Electrostat.*, vol. 46, no. 2–3, pp. 109–123, Apr. 1999, doi: 10.1016/S0304-3886(99)00006-6.
- [37] M. D. Wagh, P. S. B., S. Goel, and S. K. Sahoo, “Development of Laser-Induced Graphene-Based Automated Electro Microfluidic Viscometer for Biochemical Sensing Applications,” *IEEE Trans. Electron Devices*, pp. 1–8, 2021, doi: 10.1109/TED.2021.3107374.
- [38] S. Dudala, S. Srikanth, S. K. Dubey, A. Javed, and S. Goel, “Development of Miniaturized Interdigitated Electrode Sensors and Their Application in Taste Sensing,” *ECS Trans.*, vol. 98, no. 12, p. 49, Sep. 2020, doi: 10.1149/09812.0049ECST.
- [39] M. Ibrahim, J. Claudel, D. Kourtiche, and M. Nadi, “Geometric parameters optimization of planar interdigitated electrodes for bioimpedance spectroscopy,” *J Electr Bioimp*, vol. 4, pp. 13–22, 2013, doi: 10.5617/jeb.304.
- [40] M. L. Bhaiyya, P. K. Pattnaik, and S. Goel, “Miniaturized Electrochemiluminescence Platform with Laser-Induced Graphene-Based Single Electrode for Interference-Free Sensing of Dopamine, Xanthine, and Glucose,” *IEEE Trans. Instrum. Meas.*, vol. 70, 2021, doi: 10.1109/TIM.2021.3071215.
- [41] O. Fayyaz *et al.*, “Enhancement of mechanical and corrosion resistance properties of electrodeposited Ni–P–TiC composite coatings,” *Sci. Reports 2021 111*, vol. 11, no. 1, pp. 1–16, Mar. 2021, doi: 10.1038/s41598-021-84716-6.
- [42] W. Tanthapanichakoon, K. Matsuyama, N. Aoki, and K. Mae, “Design of microfluidic slug mixing based on the correlation between a dimensionless mixing rate and a modified Peclet number,” *Chem. Eng. Sci.*, vol. 61, no. 22, pp. 7386–7392, Nov. 2006, doi: 10.1016/J.CES.2006.08.049.
- [43] S. Berten, M. Farhat, ... F. A.-P. of the 12th, and undefined 2014, “Experimental investigation

- of pressure fluctuations in a high-energy centrifugal pump stage at off-design conditions,” *infoscience.epfl.ch*, Accessed: Aug. 16, 2021. [Online]. Available: <https://infoscience.epfl.ch/record/255210>
- [44] C. Öner, R. D. Turan, B. Telatar, Ş. Yeşildağ, Ş. Hergün, and F. Elmacioğlu, “A pilot study on salt taste sensitivity threshold in Turkish young adults,” *Anatol. J. Cardiol.*, vol. 16, no. 9, p. 731, 2016, doi: 10.14744/ANATOLJCARDIOL.2016.7257.
- [45] S. L. Cheled-Shoval, N. Reicher, M. Y. Niv, and Z. Uni, “Detecting thresholds for bitter, umami, and sweet tastants in broiler chicken using a 2-choice test method,” *Poult. Sci.*, vol. 96, no. 7, pp. 2206–2218, Jul. 2017, doi: 10.3382/PS/PEX003.
- [46] E. Ervina, I. Berget, and V. L. Almlı, “Investigating the Relationships between Basic Tastes Sensitivities, Fattiness Sensitivity, and Food Liking in 11-Year-Old Children,” *Foods 2020, Vol. 9, Page 1315*, vol. 9, no. 9, p. 1315, Sep. 2020, doi: 10.3390/FOODS9091315.
- [47] M. J. Kim, S. Choe, H. C. Kim, S. K. Cho, S.-K. Kim, and J. J. Kim, “Electrochemical Behavior of Citric Acid and Its Influence on Cu Electrodeposition for Damascene Metallization,” *J. Electrochem. Soc.*, vol. 162, no. 8, pp. D354–D359, 2015, doi: 10.1149/2.0561508jes.
- [48] J. Juansah and W. Yulianti, “Studies on Electrical behavior of Glucose using Impedance Spectroscopy,” *IOP Conf. Ser. Earth Environ. Sci.*, vol. 31, no. 1, 2016, doi: 10.1088/1755-1315/31/1/012039.
- [49] F. Zhao, X. Li, W. Xu, W. Zhang, and X. Ying, “An Electrochemical Sensor for L-Tryptophan Using a Molecularly Imprinted Polymer Film Produced by Copolymerization of o-Phenylenediamine and Hydroquinone,” *Anal. Lett.*, vol. 47, no. 10, pp. 1712–1725, 2014, doi: 10.1080/00032719.2014.880172.
- [50] A. Nag and S. C. Mukhopadhyay, “Fabrication and implementation of printed sensors for taste sensing applications,” *Sensors Actuators A Phys.*, vol. 269, pp. 53–61, Jan. 2018, doi: 10.1016/J.SNA.2017.11.023.
- [51] K. Woertz, C. Tissen, P. Kleinebudde, and J. Breikreutz, “Performance qualification of an electronic tongue based on ICH guideline Q2,” *J. Pharm. Biomed. Anal.*, vol. 51, no. 3, pp. 497–506, Feb. 2010, doi: 10.1016/J.JPBA.2009.09.029.
- [52] A. Nag, S. C. Mukhopadhyay, and J. Kosel, “Sensing system for salinity testing using laser-induced graphene sensors,” *Sensors Actuators A Phys.*, vol. 264, pp. 107–116, Sep. 2017, doi: 10.1016/J.SNA.2017.08.008.
- [53] S. Dudala, S. Srikanth, S. K. Dubey, A. Javed, and S. Goel, “Rapid Inkjet-Printed Miniaturized

- Interdigitated Electrodes for Electrochemical Sensing of Nitrite and Taste Stimuli,” *Micromachines* 2021, Vol. 12, Page 1037, vol. 12, no. 9, p. 1037, Aug. 2021, doi: 10.3390/M112091037.
- [54] A. Taniguchi, Y. Naito, N. Maeda, Y. Sato, and H. Ikezaki, “Development of a Monitoring System for Water Quality Using a Taste Sensor,” *Sensors Mater.*, vol. 11, no. 7, pp. 437–446, 1999.
- [55] M. J. Kim, S. Choe, H. C. Kim, S. K. Cho, S.-K. Kim, and J. J. Kim, “Electrochemical Behavior of Citric Acid and Its Influence on Cu Electrodeposition for Damascene Metallization,” *J. Electrochem. Soc.*, vol. 162, no. 8, pp. D354–D359, May 2015, doi: 10.1149/2.0561508jes.
- [56] R. J. Dijkstra, W. J. J. M. Scheenen, N. Dam, E. W. Roubos, and J. J. ter Meulen, “Monitoring neurotransmitter release using surface-enhanced Raman spectroscopy,” *J. Neurosci. Methods*, vol. 159, no. 1, pp. 43–50, Jan. 2007, doi: 10.1016/J.JNEUMETH.2006.06.017.
- [57] O. Niwa, M. Morita, and H. Tabei, “Highly sensitive and selective voltammetric detection of dopamine with vertically separated interdigitated array electrodes,” *Electroanalysis*, vol. 3, no. 3, pp. 163–168, Apr. 1991, doi: 10.1002/ELAN.1140030305.
- [58] G. W. Hardi and S. F. Rahman, “Amperometric Detection of Dopamine based on a Graphene Oxide/PEDOT:PSS Composite Electrode,” *Int. J. Technol.*, vol. 11, no. 5, pp. 974–983, Nov. 2020, doi: 10.14716/IJTECH.V11I5.4323.
- [59] J. M. Mohan, K. Amreen, A. Javed, S. K. Dubey, and S. Goel, “Highly Selective Electrochemical Sensing of Dopamine, Xanthine, Ascorbic Acid and Uric Acid Using a Carbon Fiber Paper,” *IEEE Sens. J.*, vol. 20, no. 19, pp. 11707–11712, Oct. 2020, doi: 10.1109/JSEN.2020.2999067.
- [60] M. A. Raj and S. A. John, “Simultaneous determination of uric acid, xanthine, hypoxanthine and caffeine in human blood serum and urine samples using electrochemically reduced graphene oxide modified electrode,” *Anal. Chim. Acta*, vol. 771, pp. 14–20, Apr. 2013, doi: 10.1016/J.ACA.2013.02.017.
- [61] B. Patella *et al.*, “Electrochemical detection of Dopamine with Negligible Interference from Ascorbic and Uric acid by means of Reduced Graphene Oxide and metals-NPs based electrodes,” *Anal. Chim. Acta*, p. 339124, Sep. 2021, doi: 10.1016/J.ACA.2021.339124.
- [62] J. Wang, “Nanomaterial-based electrochemical biosensors,” *Analyst*, vol. 130, no. 4, pp. 421–426, Mar. 2005, doi: 10.1039/B414248A.
- [63] M. Salve, A. Mandal, K. Amreen, P. K. Pattnaik, and S. Goel, “Greenly synthesized silver

- nanoparticles for supercapacitor and electrochemical sensing applications in a 3D printed microfluidic platform,” *Microchem. J.*, vol. 157, p. 104973, Sep. 2020, doi: 10.1016/J.MICROC.2020.104973.
- [64] M. N. Karim, J. E. Lee, and H. J. Lee, “Amperometric detection of catechol using tyrosinase modified electrodes enhanced by the layer-by-layer assembly of gold nanocubes and polyelectrolytes,” *Biosens. Bioelectron.*, vol. 61, pp. 147–151, Nov. 2014, doi: 10.1016/J.BIOS.2014.05.011.
- [65] S. J. Kim *et al.*, “Metallic Ti₃C₂T_x MXene Gas Sensors with Ultrahigh Signal-to-Noise Ratio,” *ACS Nano*, vol. 12, no. 2, pp. 986–993, Feb. 2018, doi: 10.1021/ACSNANO.7B07460.
- [66] C. Yang *et al.*, “Flexible Nitrogen-Doped 2D Titanium Carbides (MXene) Films Constructed by an Ex Situ Solvothermal Method with Extraordinary Volumetric Capacitance,” 2018, doi: 10.1002/aenm.201802087.
- [67] J. Guo, Q. Peng, H. Fu, G. Zou, and Q. Zhang, “Heavy-Metal Adsorption Behavior of Two-Dimensional Alkalization-Intercalated MXene by First-Principles Calculations,” *J. Phys. Chem. C*, vol. 119, no. 36, pp. 20923–20930, Sep. 2015, doi: 10.1021/ACS.JPCC.5B05426.
- [68] V. Chaudhary, A. Gautam, Y. K. Mishra, and A. Kaushik, “Emerging MXene–Polymer Hybrid Nanocomposites for High-Performance Ammonia Sensing and Monitoring,” *Nanomater. 2021, Vol. 11, Page 2496*, vol. 11, no. 10, p. 2496, Sep. 2021, doi: 10.3390/NANO11102496.
- [69] M. Kujawska, S. K. Bhardwaj, Y. K. Mishra, and A. Kaushik, “Using Graphene-Based Biosensors to Detect Dopamine for Efficient Parkinson’s Disease Diagnostics,” *Biosens. 2021, Vol. 11, Page 433*, vol. 11, no. 11, p. 433, Oct. 2021, doi: 10.3390/BIOS11110433.
- [70] M. Chandran, E. Aswathy, I. Shamna, M. Vinoba, R. Kottappara, and M. Bhagiyalakshmi, “Laccase immobilized on Au confined MXene based electrode for electrochemical detection of catechol,” *Mater. Today Proc.*, vol. 46, pp. 3136–3143, Jan. 2021, doi: 10.1016/J.MATPR.2021.02.697.
- [71] † Ali Khademhosseini *et al.*, “A Soft Lithographic Approach To Fabricate Patterned Microfluidic Channels,” *Anal. Chem.*, vol. 76, no. 13, pp. 3675–3681, Jul. 2004, doi: 10.1021/AC035415S.
- [72] S. B. Puneeth, S. A. Puranam, and S. Goel, “3-D Printed Integrated and Automated Electro-Microfluidic Viscometer for Biochemical Applications,” *IEEE Trans. Instrum. Meas.*, vol. 68, no. 7, pp. 2648–2655, Jul. 2019, doi: 10.1109/TIM.2018.2866357.
- [73] X. Jin *et al.*, “Superior role of MXene nanosheet as hybridization matrix over graphene in

- enhancing interfacial electronic coupling and functionalities of metal oxide,” *Nano Energy*, vol. 53, pp. 841–848, Nov. 2018, doi: 10.1016/J.NANOEN.2018.09.055.
- [74] F. Shahzad, A. Iqbal, S. A. Zaidi, S. W. Hwang, and C. M. Koo, “Nafion-stabilized two-dimensional transition metal carbide (Ti₃C₂T_x MXene) as a high-performance electrochemical sensor for neurotransmitter,” *J. Ind. Eng. Chem.*, vol. 79, pp. 338–344, Nov. 2019, doi: 10.1016/J.JIEC.2019.03.061.
- [75] R. Rubio-Govea *et al.*, “MoS₂ nanostructured materials for electrode modification in the development of a laccase based amperometric biosensor for non-invasive dopamine detection,” *Microchem. J.*, vol. 155, p. 104792, Jun. 2020, doi: 10.1016/J.MICROC.2020.104792.
- [76] R. Muralidharan, V. Chandrashekhar, D. Butler, and A. Ebrahimi, “A Smartphone-Interfaced, Flexible Electrochemical Biosensor Based on Graphene Ink for Selective Detection of Dopamine,” *IEEE Sens. J.*, vol. 20, no. 22, pp. 13204–13211, Nov. 2020, doi: 10.1109/JSEN.2020.3005171.
- [77] G. Hardi and S. Rahman, “Amperometric Detection of Dopamine based on a Graphene Oxide/PEDOT: PSS Composite Electrode,” *ijtech.eng.ui.ac.id*, Accessed: Sep. 21, 2021. [Online]. Available: <https://ijtech.eng.ui.ac.id/article/view/4323>
- [78] F. Xie *et al.*, “Permselectivity of Electrodeposited Polydopamine/Graphene Composite for Voltammetric Determination of Dopamine,” *Electroanalysis*, vol. 31, no. 9, pp. 1744–1751, Sep. 2019, doi: 10.1002/ELAN.201900062.
- [79] E. Bahrami, R. Amini, and S. Vardak, “Electrochemical detection of dopamine via pencil graphite electrodes modified by Cu/Cu₂O nanoparticles,” *J. Alloys Compd.*, vol. 855, p. 157292, Feb. 2021, doi: 10.1016/J.JALLCOM.2020.157292.
- [80] J. H. Coelho *et al.*, “Exploring the exocellular fungal biopolymer botryosphaeran for laccase-biosensor architecture and application to determine dopamine and spironolactone,” *Talanta*, vol. 204, pp. 475–483, Nov. 2019, doi: 10.1016/J.TALANTA.2019.06.033.
- [81] S. Madhurantakam, K. Jayanth Babu, J. B. Balaguru Rayappan, and U. Maheswari Krishnan, “Fabrication of a Nano-Interfaced Electrochemical Triglyceride Biosensor and its Potential Application towards Distinguishing Cancer and Normal Cells,” *ChemistrySelect*, vol. 5, no. 43, pp. 13492–13501, Nov. 2020, doi: 10.1002/SLCT.202003771.
- [82] T. Ohnuma *et al.*, “Benefits of use, and tolerance of, medium-chain triglyceride medical food in the management of Japanese patients with Alzheimer’s disease: a prospective, open-label pilot study,” *Clin. Interv. Aging*, vol. 11, p. 29, Jan. 2016, doi: 10.2147/CIA.S95362.

- [83] K. Miyashita *et al.*, “A new enzyme-linked immunosorbent assay system for human hepatic triglyceride lipase,” *Clin. Chim. Acta*, vol. 424, pp. 201–206, Sep. 2013, doi: 10.1016/J.CCA.2013.06.016.
- [84] S. Giansante, H. E. Giana, A. B. Fernandes, and L. Silveira, “Analytical performance of Raman spectroscopy in assaying biochemical components in human serum,” *Lasers Med. Sci.*, vol. 37, no. 1, pp. 287–298, Feb. 2022, doi: 10.1007/S10103-021-03247-8/TABLES/5.
- [85] I. Lee *et al.*, “Development of Interdigitated Electrode Based Enzyme Sensor for Triglyceride Monitoring Using Engineered Oxygen Insensitive Glycerol 3-Phosphate Oxidase,” *SSRN Electron. J.*, Jun. 2022, doi: 10.2139/SSRN.4145645.
- [86] Z. Zhu, H. Song, Y. Wang, and Y. H. P. Zhang, “Protein engineering for electrochemical biosensors,” *Curr. Opin. Biotechnol.*, vol. 76, p. 102751, Aug. 2022, doi: 10.1016/J.COPBIO.2022.102751.
- [87] K. L. Baker, F. B. Bolger, and J. P. Lowry, “Development of a microelectrochemical biosensor for the real-time detection of choline,” *Sensors Actuators B Chem.*, vol. 243, pp. 412–420, May 2017, doi: 10.1016/J.SNB.2016.11.110.
- [88] P. S. Venkateswaran, A. Sharma, S. Dubey, A. Agarwal, and S. Goel, “Rapid and Automated Measurement of Milk Adulteration Using a 3D Printed Optofluidic Microviscometer (OMV),” *IEEE Sens. J.*, vol. 16, no. 9, pp. 3000–3007, May 2016, doi: 10.1109/JSEN.2016.2527921.
- [89] M. D. Fernández-Ramos, M. Bolaños-Bañuelos, and L. F. Capitán-Vallvey, “Point-of-care assay platform for uric acid, urea, and triglycerides with a microfluidic paper device (μ PAD) controlled by stimulus-sensitive valves,” *Talanta*, vol. 254, p. 124189, Mar. 2023, doi: 10.1016/J.TALANTA.2022.124189.
- [90] D. Calabria, C. Caliceti, M. Zangheri, M. Mirasoli, P. Simoni, and A. Roda, “Smartphone-based enzymatic biosensor for oral fluid L-lactate detection in one minute using confined multilayer paper reflectometry,” *Biosens. Bioelectron.*, vol. 94, pp. 124–130, Aug. 2017, doi: 10.1016/J.BIOS.2017.02.053.
- [91] L. Yi, J. Li, C. Guo, L. Li, and J. Liu, “Liquid metal ink enabled rapid prototyping of electrochemical sensor for wireless glucose detection on the platform of mobile phone,” *J. Med. Devices, Trans. ASME*, vol. 9, no. 4, Dec. 2015, doi: 10.1115/1.4031659/376795.
- [92] T. Saha *et al.*, “Wireless Wearable Electrochemical Sensing Platform with Zero-Power Osmotic Sweat Extraction for Continuous Lactate Monitoring,” *ACS Sensors*, vol. 7, no. 7, pp. 2037–2048, Jul. 2022, doi: 10.1021/ACSSENSORS.2C00830/ASSET/IMAGES/LARGE/SE2C00830_0005.JPEG.

- [93] J. H. Shim, J. Kim, C. Lee, and Y. Lee, "Electrocatalytic activity of gold and gold nanoparticles improved by electrochemical pretreatment," *J. Phys. Chem. C*, vol. 115, no. 1, pp. 305–309, Jan. 2011, doi: 10.1021/JP1067507/SUPPL_FILE/JP1067507_SI_001.PDF.
- [94] S. Hebié, K. B. Kokoh, K. Servat, and T. W. Napporn, "Shape-dependent electrocatalytic activity of free gold nanoparticles toward glucose oxidation," *Gold Bull.*, vol. 46, no. 4, pp. 311–318, Dec. 2013, doi: 10.1007/S13404-013-0119-4/FIGURES/5.
- [95] I. R. Suhito, N. Angeline, and T.-H. Kim, "Nanomaterial-modified Hybrid Platforms for Precise Electrochemical Detection of Dopamine," *BioChip J. 2019 131*, vol. 13, no. 1, pp. 20–29, Mar. 2019, doi: 10.1007/S13206-019-3106-X.
- [96] K. Mahato *et al.*, "Gold nanoparticle surface engineering strategies and their applications in biomedicine and diagnostics," *3 Biotech*, vol. 9, no. 2, pp. 1–19, Feb. 2019, doi: 10.1007/S13205-019-1577-Z/FIGURES/5.
- [97] X. Du *et al.*, "UV-Triggered Dopamine Polymerization: Control of Polymerization, Surface Coating, and Photopatterning," *Adv. Mater.*, vol. 26, no. 47, pp. 8029–8033, Dec. 2014, doi: 10.1002/ADMA.201403709.
- [98] Y. Ren, J. G. Rivera, L. He, H. Kulkarni, D. K. Lee, and P. B. Messersmith, "Facile, high efficiency immobilization of lipase enzyme on magnetic iron oxide nanoparticles via a biomimetic coating," *BMC Biotechnol.*, vol. 11, Jun. 2011, doi: 10.1186/1472-6750-11-63.
- [99] N. R. Nirala *et al.*, "Partially reduced graphene oxide–gold nanorods composite based bioelectrode of improved sensing performance," *Talanta*, vol. 144, pp. 745–754, Nov. 2015, doi: 10.1016/J.TALANTA.2015.05.059.
- [100] D. R. Kumar, S. Kesavan, T. T. Nguyen, J. Hwang, C. Lamiel, and J. J. Shim, "Polydopamine@electrochemically reduced graphene oxide-modified electrode for electrochemical detection of free-chlorine," *Sensors Actuators B Chem.*, vol. 240, pp. 818–828, Mar. 2017, doi: 10.1016/J.SNB.2016.09.025.
- [101] S. M. Kang, S. Park, D. Kim, S. Y. Park, R. S. Ruoff, and H. Lee, "Simultaneous Reduction and Surface Functionalization of Graphene Oxide by Mussel-Inspired Chemistry," *Adv. Funct. Mater.*, vol. 21, no. 1, pp. 108–112, Jan. 2011, doi: 10.1002/ADFM.201001692.
- [102] M. D. Wagh, H. Renuka, P. S. Kumar, K. Amreen, S. K. Sahoo, and S. Goel, "Integrated Microfluidic Device with MXene enhanced Laser-Induced Graphene Bioelectrode for Sensitive and Selective Electroanalytical Detection of Dopamine," *IEEE Sens. J.*, pp. 1–1, Jun. 2022, doi: 10.1109/JSEN.2022.3182293.

- [103] B. M. Sachith *et al.*, “Simple sonochemical synthesis of SrCuO₂ assisted GCN nanocomposite for the sensitive electrochemical detection of 4-AAP,” *Surfaces and Interfaces*, vol. 20, p. 100603, Sep. 2020, doi: 10.1016/J.SURFIN.2020.100603.
- [104] Y. Liang, C. Cui, L. Liu, H. Geng, S. Yang, and S. Cui, “Microstructure and mechanical properties of A356.2(Al-7Si-0.3Mg) alloy refined and modified by in-situ Al-SrB₆ composites,” *Surfaces and Interfaces*, vol. 36, p. 102513, Feb. 2023, doi: 10.1016/J.SURFIN.2022.102513.

LIST OF PUBLICATIONS AND PATENT :

1. **Mrunali D. Wagh**, S. B. Puneeth, Sanket Goel, and Subhendu Kumar Sahoo Wax-Printed Microfluidic Paper Analytical Device for Viscosity-Based Biosensing in a 3D Printed Image Analysis Platform Microactuators, Microsensors and Micromechanisms. Mechanisms and Machine Science, vol 126. Springer, Cham. https://doi.org/10.1007/978-3-031-20353-4_26
2. **Mrunali D. Wagh**, Renuka H, Paver Sai Kumar, Khairunnisa Amreen, Subhendu Kumar Sahoo and Sanket Goel, Microfluidic Biosensor with Integrated Electrodes Configuring Mxene over Laser-Induced Graphene for Selective Electroanalytical Detection of Dopamine and Other Biochemicals IEEE Sensor journal, <https://doi.org/10.1109/JSEN.2022.3182293>
3. Himanshi Awasthi*, Jayapiriya U S*, Renuka H*, **Mrunali D. Wagh***, Avinash Kothuru, Alok Kumar Srivastava and Sanket Goel, "Flexible Paper and Cloth Substrates with Conductive Laser-Induced Graphene Traces for Electroanalytical Sensing, Energy Harvesting and Supercapacitor Applications," in IEEE Sensors Journal, <https://doi.org/10.1109/JSEN.2022.3170538>
4. **Mrunali D. Wagh**, Subhendu Kumar Sahoo and Sanket Goel, Development of Laser-Induced Graphene-based Microfluidic Interdigital Electrodes for Taste Sensing Application, Sensors and Actuators: A. Physical <https://doi.org/10.1016/j.sna.2021.113301>
5. **Mrunali D. Wagh**, S. B. Puneeth, Sanket Goel, and Subhendu Kumar Sahoo. "Development of Laser-Induced Graphene-Based Automated Electro Microfluidic Viscometer for Biochemical Sensing Applications." IEEE Transactions on Electron Devices 68, no. 10 (2021):5184-5191 <http://doi.org/10.1109/TED.2021.3107374>.
6. **Mrunali D. Wagh**, Kavita Pande, S. J. dhoble ,R. K. Sharma, Nitin Narkhede, Abhay D. Deshmukh Nitrogen Optimized Highly Stable Carbon for Increasing the Efficiency of Supercapacitors, International Journal of Energy Research <https://doi.org/10.1002/er.8285>

LIST OF PATENT :

1. Integrated Polymeric Microfluidic Electroanalytical Device, patent application number **202111059663** (Filed) Dated: 13/01/2023.
2. Graphene bio electrode comprising polydopamine-coated gold nanoparticles, method of synthesis, and biosensor system thereof. Patent application number **202311002716** (Filed) Dated: 22/12/2021.
3. Improved Electro-microfluidic droplet chip. The patent application number is **202311052103** (Filed) Dated 03-08-2023.
4. Improved Electro-microfluidic droplet chip. The patent application number is **202311052236** (Filed) Dated 03-08-2023.

BIOGRAPHIES

Biography of the Candidate - Ms. Mrunali Wagh

Mrunali D Wagh received her Masters in VLSI Design from Shri Ramdeobaba College of Engineering and Management, Nagpur, India in 2019. Earlier, she completed her undergraduate studies Electronics & Telecommunication Engineering from Nagpur university, India in 2016. Since 2019, she is working for her Ph.D. under the supervision of Prof. Subhendu Sahoo, Prof. Sanket Goel, Prof. Michael Dickey. Her research interests include Microfluidic biosensors, flexible devices using laser-induced graphene, and their applications in biomedical via the electrochemical platform.

Biography of the Supervisor - Dr. Subhendu Sahoo

Subhendu Kumar Sahoo completed his B.E. in Electronics and telecommunication engineering from Utkal University, Orissa, India, in 1994 with honors securing fifth position in the university. He obtained his M.E. in Electronic Systems and Communication from R.E.C. (N.I.T.) Rourkela in 1998. He received a Ph. D. degree in Electrical Engineering from the Birla Institute of Technology and Science, Pilani, in 2006. He worked as a faculty in the Electrical and Electronics Engineering department from 2009 to 2011. Presently he is working as Professor at Birla Institute of Technology and Science, Pilani Hyderabad campus. His research areas are high- performance arithmetic circuits and VLSI circuits for Digital Signal Processing applications, IoT-enabled sensors, and circuit designing.

Biography of the Co-Supervisor - Dr. Sanket Goel

Sanket Goel is Associate Professor with the Department of Electrical and Electronics Engineering BITS-Pilani, Hyderabad campus. Prior to this, headed the EEE Department at BITS-Pilani (2017-2020), and R&D department and was an Associate Professor at the University of Petroleum & Energy Studies (UPES), Dehradun, India (2011-2015). Sanket did his BSc (H- Physics) from the Ramjas College, Delhi University; MSc (Physics) from IIT Delhi; PhD (Electrical Engineering) from the University of Alberta, Canada on NSERC fellowship; and MBA in International Business from Amity University in 1998, 2000, 2006 and 2012 respectively. He has worked with two Indian national labs, Institute of Plasma Research, Gandhinagar (2000-2001) and DEBEL-DRDO, Bangalore (2006). As an NIH fellow, Sanket did his postdoctoral work at the Stanford University, US (2006-2008), and worked as a Principal Investigator at A*STAR, Singapore (2008- 2011) before joining UPES in July 2011. His current research interests are MEMS, Microfluidics, Nanotechnology, Materials and Devices for Energy, Biochemical and Biomedical Applications, Science Policy and Innovation & Entrepreneurship. As a Principal Investigator, Sanket has been implementing several funded projects (from DRDO, DST, ISRO, MNRE, SERB, Government of India; UNESCO; European Commission) and has been collaborating with various groups in India and abroad. During the course of his career, he has won several awards, including Dr. C R Mitra Best Faculty Award (2021), Fulbright-Nehru

fellowship (2015), DST Young Scientist Award (2013), American Electrochemical Society's Best students paper award (2005), University of Alberta PhD thesis award (2005) etc. Sanket is widely travelled and has >180 publications and 12 patents (1 US and 11 Indian) to his credits. He has delivered >70 invited talks, guided/guiding 24 PhD, and several Masters and Bachelors students.

Sanket Goel is a Senior Member, IEEE; Life Member, Institute of Smart Systems and Structures; Life Member, Indian Society of Electrochemical Chemistry. Currently he is an Associate Editor of IEEE Transactions on NanoBioscience, IEEE Sensors Journal, IEEE Access, Applied Nanoscience, and guest editor of Special Issue in Sensors - "3D Printed Microfluidic Devices". He is also serving as a Visiting Associate Professor with UiT, The Arctic University of Norway

Biography of the Co-Supervisor - Michael Dickey

Michael Dickey received a BS in Chemical Engineering from Georgia Institute of Technology (1999) and a PhD from the University of Texas (2006) under the guidance of Professor Grant Willson. From 2006-2008 he was a post-doctoral fellow in the lab of Professor George Whitesides at Harvard University. He is currently the Camille and Henry Dreyfus Professor in the Department of Chemical & Biomolecular Engineering at NC State University. He completed a sabbatical at Microsoft in 2016. Michael's research interests include soft matter (liquid metals, gels, polymers) for soft and stretchable devices (electronics, energy harvesters, textiles, and soft robotics). He is on the advisory board for several journals including Advanced Materials, Advanced Materials Technologies, and Droplet